

The Pennsylvania State University

The Graduate School

Department of Electrical Engineering

A QUANTITATIVE ANALYSIS OF TUNABLE LONG PERIOD GRATING
TECHNOLOGY AND ITS APPLICATION

A Thesis in

Electrical Engineering

by

Jonathan E. Lee

Submitted in Partial Fulfillment
of the Requirements
for the Degree of

Doctor of Philosophy

December 2007

The thesis of Jonathan E. Lee was reviewed and approved* by the following:

Stuart (Shizhuo) Yin
Professor of Electrical Engineering
Thesis Co-Advisor
Co-Chair of Committee

Karl Reichard
Assistant Professor of Acoustics, Research Associate
Thesis Co-Advisor
Co-Chair of Committee

Qiming Zhang
Distinguished Professor of Electrical Engineering

C. Russell Philbrick
Professor of Electrical Engineering

Qi Li
Professor of Physics

W. Kenneth Jenkins
Professor of Electrical Engineering
Head of the Department of Electrical Engineering

*Signatures are on file in the Graduate School

ABSTRACT

In this thesis, a design for an electro-optically tunable, fiber optic filter based on a long period fiber grating (LPFG) is introduced and is the motivation for the quantitative analysis that follows. The basic fundamentals of coupled mode theory are presented and used to distinguish LPFGs from fiber Bragg gratings (FBGs). A three-layer model is then used to demonstrate the feasibility of the tunable filter design. The model results show that an LPFG with a thin cladding ($\sim 35\text{-}40 \mu\text{m}$) will have an enhanced sensitivity to changes in the ambient index and will have a single resonant band in its output spectrum. The results of the three-layer model are experimentally verified, but unexpected LPFG tuning behavior is observed when a high index indium tin oxide (ITO) overlay is coated on the fiber. The ITO overlay, which had been omitted in the three-layer model, is shown to induce cladding mode transitions in the fiber as the ambient index is increased. These transitions significantly affect the tuning performance of an LPFG, and a new four-layer model, which includes the overlay, is developed to more accurately predict an ITO coated LPFG's tuning behavior. The four-layer model is used to confirm and quantify the effects of mode transitions. The measured data from a number of ITO coated LPFGs is then compared to the model data to see how well the model predicts the tuning behavior of real LPFGs fabricated in our lab. By making a few adjustments to the model constants to account for variations in the fabrication processes, the model is made to fit to the various data sets. The tuning performance of one LPFG fabricated in our lab nearly matched the performance of the ideal-case LPFG predicted by the model. However, the errors that are consistently introduced by our equipment during fabrication prevented us from replicating the sample and proved to be the limiting factor in our research effort. Although we were unable to produce a working, electro-optically tunable filter prototype, this research effort was not pursued in vain. The four-layer model presented in this thesis is a comprehensive analytical tool that can be used to predict both the tuning range and peak depth of a tunable LPFG that has been coated with a high index overlay. Using the model as a guide, we fabricated an ITO coated LPFG whose resonant peak tuned in excess of 200 nm when the ambient refractive index was increased by 0.01. To the best knowledge of the author, this is the highest sensitivity reported for an LPFG to date. In addition to the tuning performance, the resonant peak remains within 1 dB of its maximum depth for nearly 150 nm of the tuning range. Furthermore, we examine several future research topics that could benefit from the analysis in this thesis.

TABLE OF CONTENTS

LIST OF FIGURES	v
ACKNOWLEDGEMENTS.....	ix
Chapter 1 Introduction	1
Chapter 2 Coupled Mode Theory and Index Gratings in Fiber Optics	6
<i>2.1 - Coupled Mode Theory</i>	6
<i>2.2 - Fiber Bragg Gratings</i>	9
<i>2.3 - Long Period Fiber Gratings (LPFGs)</i>	11
Chapter 3 LPFG Analysis Using a Three-Layer Model	13
<i>3.1 - Three-Layer Model Theory and Calculations</i>	14
<i>3.2 - A Single Resonant Band LPFG</i>	24
<i>3.3 - LPFG Tuning</i>	28
Chapter 4 A Tunable Filter Design Based on a Single Resonant Band LPFG	34
<i>4.1 - LPFG Fabrication</i>	35
<i>4.2 - Filter Testing</i>	37
Chapter 5 Cladding Mode Transitions and the Four Layer Model.....	42
<i>5.1 - ITO Characterization and Cladding Mode Transitions</i>	42
<i>5.2 - Theoretical analysis of the four-layer model</i>	49
Chapter 6 Experimental Results and Analysis.....	67
<i>6.1 - LPFG Tuning Analysis</i>	67
<i>6.2 - Peak Depth Analysis</i>	87
<i>6.3 - Optimizing the LPFG Performance</i>	93
Chapter 7 Future Work	98
<i>7.1 - Tunable LPFG Filter</i>	98
<i>7.2 - Tunable LPGs in planar waveguides</i>	106
<i>7.3 - Add/drop tunable filter</i>	108
<i>7.3 - Sensing applications</i>	110
Chapter 8 Summary and Conclusions.....	112
References.....	118
Appendix Publications.....	125

LIST OF FIGURES

Figure 1.1: Schematic of an LPFG [22].....	1
Figure 1.2: A tunable, fiber optic filter design based on a thin cladding LPFG with an E-O polymer second cladding [16].....	2
Figure 2.1: Contradirectional coupling in a single mode fiber for a) core mode/core mode coupling and b) core mode/cladding mode coupling.....	9
Figure 2.2: Codirectional coupling in a single mode fiber (core mode/cladding mode).....	11
Figure 3.1: The normalized propagation constants, b , and the effective indices, n_{eff} , of a number of modes are plotted as a function of the V-parameter [35].	17
Figure 3.2: Effective indices of the core and cladding modes as a function of wavelength (Fiber diameter = 125 μm).	20
Figure 3.3: Grating period as a function of wavelength (Fiber diameter = 125 μm , $\Lambda = 500$).	21
Figure 3.4: LPFG output spectrum (Fiber Diameter = 125 μm , $\Lambda = 500$).	22
Figure 3.5: The coupling constants, κ , divided by the grating profile, σ , for coupling between the core mode and the j^{th} cladding mode. The even and odd modes are shown separately [36].....	23
Figure 3.6: Effective indices of the core and cladding modes as a function of wavelength (Fiber diameter = 35 μm).	25
Figure 3.7: Grating period as a function of wavelength (Fiber Diameter = 35 μm , $\Lambda = 500$).	26
Figure 3.8: LPFG output spectrum (Fiber Diameter = 35 μm , $\Lambda = 500$).....	27
Figure 3.9: The simulated spectrum of a thin cladding LPFG at several different ambient indices.....	30
Figure 3.10: LPFG spectra for various index matching oils (Fiber diameter = 35 μm , $\Lambda = 400 \mu m$).	31
Figure 3.11: Resonant wavelength (top) and peak depth (bottom) as a function of ambient refractive index (Fiber diameter = 35 μm , $\Lambda = 400 \mu m$).	32

Figure 3.12: Top graph: experimentally measured resonant wavelength of the longest wavelength attenuation band (Fiber diameter = 125 μm , $\Lambda = 275 \mu\text{m}$). Bottom graph: depth of resonant peak as a function of n_3 [22].	33
Figure 4.1: An all-fiber, electrically tunable, fiber optic filter based on a single period long period fiber grating with an electro-optic polymer second cladding [16].	35
Figure 4.2: The six basic steps required to fabricate the tunable LPFG filter.	36
Figure 4.3: The spectrum of a LPFG is tuned 18 nm electro-optically using pure terpolymer.	38
Figure 4.4: The spectrum of a LPFG is tuned approximately 10 nm using a $\sim 5\%$ volume fraction nanocomposite polymer.	39
Figure 4.5: A LPFG with a $\sim 1.5\%$ volume nanocomposite cladding had no resonant peak without an applied voltage. As the voltage was increased, the peak reappeared and tuned over 50 nm.	40
Figure 4.6: The spectrum of a thin cladding, ITO coated LPFG being tuned with index oils. The resonant peak is present in air, but disappears at an ambient index of 1.40. As the index increases, the peak reappears at longer wavelengths and tunes nearly 100 nm. (Fiber diameter = 35 μm , $\Lambda = 400 \mu\text{m}$).	41
Figure 5.1: The Anatech Hummer XII sputtering system used to perform our ITO depositions.	43
Figure 5.2: Effective refractive indices of the LP_{02} - LP_{08} cladding modes versus the surrounding refractive index in a high refractive index coated fiber with: (a) 150 nm thin film; (b) 200 nm thin film; (c) 250 nm thin film; and (d) 300 nm thin film [25].	46
Figure 5.3: Measured LPFG resonant wavelengths as a function of the ambient index for different ITO thicknesses. (Fiber diameter = 40 μm , $\Lambda = 400 \mu\text{m}$).	48
Figure 5.4: (a) Schematic structure of the E-O tunable LPG filter, (b) Cross-sectional view of the E-O tunable LPG filter [20].	49
Figure 5.5: Transversal electric field distributions of the 1 st cladding mode (a) with ITO ($n = 1.80$ at 1550 nm) and (b) without ITO.	60
Figure 5.6: Transversal electric field distributions of the 2 nd cladding mode (a) with ITO ($n = 1.80$ at 1550 nm) and (b) without ITO.	61
Figure 5.7: Transversal electric field distributions of the 3 rd cladding mode (a) with ITO ($n = 1.80$ at 1550 nm) and (b) without ITO.	61

Figure 5.8: Effective refractive indices of the 1 st cladding mode as a function of polymer refractive index in fibers with and without an ITO overlay. (ITO refractive index: 1.80; ITO thickness = 50 nm, Wavelength = 1550 nm)	63
Figure 5.9: Effective refractive indices of the 2 nd cladding mode as a function of polymer refractive index in fibers with and without an ITO overlay. (ITO refractive index: 1.80; ITO thickness = 50 nm, Wavelength = 1550 nm)	63
Figure 5.10: Effective refractive indices of the 3 rd cladding mode as a function of polymer refractive index in fibers with and without an ITO overlay. (ITO refractive index: 1.80; ITO thickness = 50 nm, Wavelength = 1550 nm)	64
Figure 6.1: Experimentally measured spectra of an LPFG in several different ambient indices (a) before and (b) after being coated with a 50 nm ITO overlay. (Fiber diameter = 40 μm , Grating period = 400 μm , Grating length = 8 mm (20 periods))	68
Figure 6.2: LPFG resonant wavelengths as a function of the ambient oil index with and without ITO.....	69
Figure 6.3: The calculated effective indices of the 1 st cladding mode are converted into resonant wavelengths and compared to the measured spectral data. (No ITO; Effective core index ($n_{\text{eff}}^{\text{co}}$) \sim 1.4465, Grating Period (Λ) = 400 μm).....	72
Figure 6.4: The calculated effective indices of the 1 st cladding mode are converted into resonant wavelengths using the full phase matching condition and compared to the measured spectral data. (No ITO; Effective core index ($n_{\text{eff}}^{\text{co}}$) \sim 1.4465, Grating Period (Λ) = 400 μm , Grating Strength (σ) = 7.5×10^{-4}).....	76
Figure 6.5: ITO coated LPFG wavelengths as a function of the ambient index compared to the resonant wavelengths calculated from the model effective cladding indices. (Effective core index ($n_{\text{eff}}^{\text{co}}$) \sim 1.4465, Grating Period (Λ) = 400 μm , Grating Strength (σ) = 7.5×10^{-4} , ITO thickness = 50 nm, ITO refractive index \sim 1.80).....	77
Figure 6.6: Several pictures of the grating writing setup.....	79
Figure 6.7: Tuning spectra taken from six, batch processed ITO coated LPFGs.	81
Figure 6.8: The measured resonant wavelengths from the six batch processed, ITO coated LPFG samples as a function of the ambient oil index.....	82
Figure 6.9: Resonant wavelengths from the six batch processed, ITO coated LPFGs as a function of the ambient index compared to the resonant wavelengths calculated from the model effective cladding indices. (Effective	

core index (n_{eff}^{co}) ~ 1.4465, Grating Period (Λ) = 400 μ m, Grating Strength (σ) = 7.5x10 ⁻⁴ , ITO thickness = 50 nm, ITO refractive index ~1.80).....	85
Figure 6.10: Resonant wavelengths from the six batch processed, ITO coated LPFGs as a function of the ambient index compared to the resonant wavelengths calculated from the model effective cladding indices. (Effective core index (n_{eff}^{co}) ~ 1.4465, Grating Period (Λ) = 400 μ m, Grating Strength (σ) = 4.9x10 ⁻⁴ , ITO thickness = 50 nm, ITO refractive index ~ 1.80).....	86
Figure 6.11: The calculated coupling constants (κ) of the first three cladding modes as a function of the ambient index. In the top plot (a), the ambient index range is 1.000-1.445. The bottom plot (b) is an exploded view of the 1.400-1.445 ambient index range. (ITO thickness = 50 nm, ITO refractive index ~ 1.80).....	89
Figure 6.12: The measure peak depths from the six batch processed LPFGs as a function of the ambient index. In the top plot (a), the ambient index range is 1.000-1.445. The bottom plot (b) is an exploded view of the 1.400-1.445 ambient index range.....	92
Figure 6.13: The tuning spectra of an LPFG that maintains a stable peak depth over nearly 150 nm of its tuning range. (Fiber diameter = 40 μ m, Grating period (Λ) = 400 μ m, Grating length = 8 mm, ITO thickness = 50 nm, ITO refractive index ~1.80).....	94
Figure 6.14: Tuning spectra of several LPFGs whose initial peak wavelengths were 1356 nm. (Fiber diameter = 40 μ m, Grating period (Λ) = 400 μ m, Grating length = 8 mm, ITO thickness = 50 nm, ITO refractive index ~ 1.80)	96
Figure 7.1: The resonant peak bandwidths of two LPFGs are compared: (a) an LPFG that has a 400 μ m grating period and is 8 mm in length versus (b) an LPFG that has a 400 μ m grating period and is 40 mm in length. When the number of periods is increased by a factor of five, the bandwidth is reduced by approximately the same factor.....	100
Figure 7.2: Optical add/drop filter design featuring a tunable IPG.	109

ACKNOWLEDGEMENTS

I would first like to thank Dr. Stuart Yin for his advice, support, and guidance throughout the duration of my doctoral research and this thesis. I would also like to thank Dr. Karl Reichard for co-advising this project. Both Dr. Yin and Dr. Reichard provided invaluable input throughout the course of this work and were instrumental to its successful completion. I would like to thank Dr. Qiming Zhang, Dr. C. Russell Philbrick, and Dr. Qi Li for agreeing to be members of my thesis committee. This material in this thesis is based upon work partially supported by the Penn State Electro-Optic Center and sponsored by the Naval Air Systems Command under Contract Number N00421-03-D-0044, Delivery Order Number 01.

I would like to thank Chun Zhan, Jae Hun Kim and the rest of my fellow lab members for assisting me with various portions of this project and for making the E-O lab an enjoyable place to work. I would especially like to thank Qin Chen and Minren Lin for their help developing and programming the four-layer model and for their work on the E-O polymers. I would also like to thank Corey Hahn and Sung Hyun Nam for their contributions to this project.

Finally, I would like to thank my parents for their love and support throughout my doctoral work. Their guidance has always been a key to my success. I would also like to thank my girlfriend, Heather, for her love and support ever since I started my graduate work. You always find ways to make me keep things in perspective and can always put a smile on my face. I am lucky to have you in my life.

Chapter 1

Introduction

In recent years, a great deal of research has been done in the area of integrated optical devices. Fiber optic gratings have been an area of particular interest because of their potential use in a wide range of applications, including optical filters, sensors, and optical communications components [1-21]. One device that we have been working on in our lab is an electro-optically tunable, fiber optic filter based on a long period fiber grating (LPFG) [15-21]. A schematic diagram of an LPFG is shown in Figure 1.1, and the basic configuration of the tunable filter is shown in Figure 1.2. An LPFG couples energy at discrete wavelengths from the forward propagating core mode to forward propagating cladding modes. In the output spectrum, resonant peaks appear at the wavelengths which

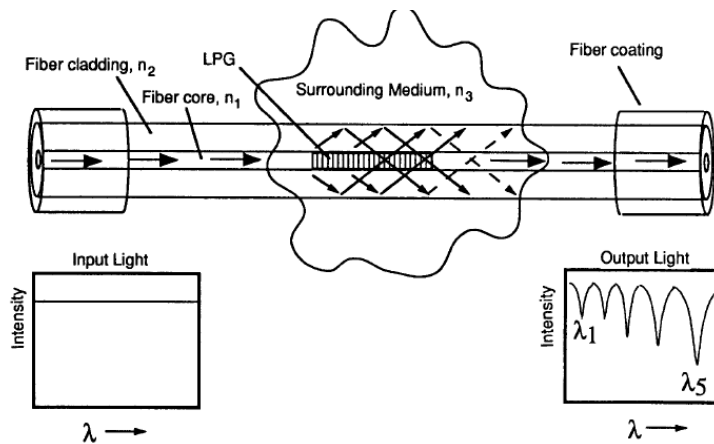


Figure 1.1: Schematic of an LPFG [22].

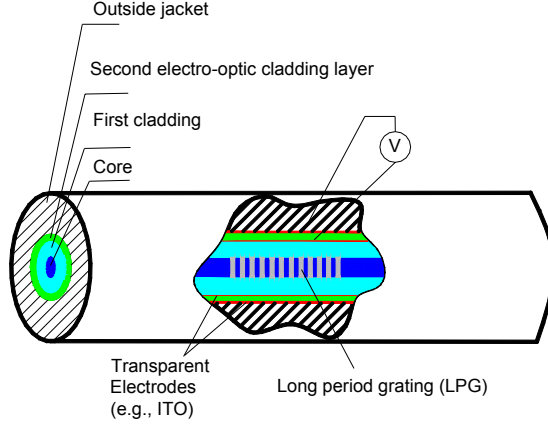


Figure 1.2: A tunable, fiber optic filter design based on a thin cladding LPFG with an E-O polymer second cladding [16].

were coupled out of the core. The tunable filter consists of a thin cladding LPFG surrounded by a second cladding layer made of electro-optic (E-O) polymer [16-21]. By applying an electric field across the polymer second cladding, the refractive index of the E-O polymer is changed, causing the resonant wavelength(s) in the output spectrum to tune.

The tunable filter design leverages the LPFG's intrinsic sensitivity to changes in the surrounding, or ambient, refractive index [17-24] and the thin silica cladding of the fiber in which the LPFG is written. A three-layer model, where the three layers are the silica fiber core, the silica first cladding, and the E-O polymer second cladding, was developed to quantitatively analyze the device and demonstrate its feasibility. The model results show that by reducing the thickness of the silica cladding around the fiber core, the LPFG's sensitivity to changes in the ambient index increases and a single resonant band is achieved in the output spectrum [24].

Using the three-layer model as a guide, the primary goal of our research effort was to develop a working prototype of the tunable filter device. The targeted performance specifications for the device included a 40 nm minimum tuning range to cover the entire

optical C-band (1525-1565 nm), a resonant peak bandwidth of less than 1 nm, and nanosecond switching speeds. This goal required us to engineer approximately six fiber processing steps: 1) fiber etching; 2) LPFG fabrication; 3) inner electrode coating; 4) application of the E-O polymer second cladding; 5) outer electrode coating; and finally, 6) wiring and packaging. There are unique challenges associated with each of the steps, and several of them required multiple processes to complete. We also collaborated with polymer groups in the electrical engineering and material science departments to develop an E-O polymer with characteristics suitable for this device. The input parameters for the three-layer model were used as a starting point for fabricating the device. The model used numerical analysis to find the effective refractive indices of the core and cladding modes, which could then be used to calculate the position of an LPFG's resonant peak. It assumed that all aspects of the device were ideal, meaning that the fabrication parameters were both uniform and precise and that the device had perfect cylindrical symmetry. Due to the resources available in our lab and the nature of the processes required to make the device, we expected that experimental error would cause some differences between the measured data and the ideal model. However, we found that some aspects of our sample LPFGs deviated significantly from the model. In particular, the measured values for the resonant peak wavelength, the resonant peak depth, and the tuning characteristics did not agree with the predicted values.

Based on our early results, a more complete model of the tunable LPFG was needed to continue working toward a prototype. We discovered that the major cause of the differences between the three-layer model and our experimental data was the high index indium tin oxide (ITO) electrode that was sputtered onto the fiber before the E-O polymer was applied. Since the thin ITO layer was transparent and only about 50 nm thick (much less than the 1525-1565 nm wavelengths used in C-band fiber optic communications), it was

omitted from the three-layer model because its effect on the tunable filter was initially thought to be negligible. However, with additional research, we discovered that thin film overlays induce mode transitions in the fiber cladding as the ambient index is increased [25-30]. These mode transitions significantly affect the tuning characteristics of an LPFG and cannot be neglected. As a result, we needed to create a more complete four-layer model that included the high index ITO layer.

After a new four-layer model was created, we fit the model results to the data taken from our experimental LPFGs. In order for the model to be an effective research tool in the development of the tunable filter, it had to accurately simulate the performance of the LPFGs that were fabricated in the lab. Concurrently, we needed to be able to take the model parameters and fabricate an LPFG that agreed with the predicted performance metrics. Given the limitations of the equipment and the inevitability of experimental error, we did not expect the performance of our experimental LPFGs to perfectly match the metrics of the ideal-case LPFG simulated by the model. However, once we had calibrated the model by factoring in some of the known experimental variations, we nearly fit the model results to our measured data and confirmed that errors in our fabrication processes were having a significant effect on the consistency of our experimental LPFGs.

The thesis that follows consists of seven chapters in addition to the introduction presented here. Chapter 2 opens the thesis with background information on coupled mode theory and fiber optic gratings. The basic principles of coupled mode theory are explained and derived, and we examine the differences between fiber Bragg gratings (FBGs) and LPFGs. Chapter 3 presents the three-layer model, its results, and some of our early experimental data. In this chapter, we show how the model was used to prove the feasibility of the tunable LPFG filter. Chapter 4 looks at the LPFG filter design and the processes

needed to fabricate the device. We also detail how the LPFG filter samples were experimentally tested and highlight the unexpected experimental results that led to the development of a more complete four-layer model. Chapter 5 describes the cladding mode transitions that are induced by high index overlays and provides a theoretical analysis of the four-layer model. The results of the new model qualitatively and quantitatively verify the effects of cladding mode transitions on our tunable filter. In Chapter 6, the results of the four-layer model are compared to our experimental data. The model is calibrated to fit our measured results, and we show how the LPFG and ITO overlay parameters can be optimized to achieve a device with a large tuning range and a stable peak depth. Additionally, we present measured data from an optimized ITO coated LPFG that nearly matches the predicted performance of the model and discuss the effects of experimental errors on our measured results. Chapter 7 takes a brief look at some future research topics related to the work presented in this thesis. In addition to continuing the tunable filter work, we suggest that tunable grating technology be applied to planar waveguides, and optical add/drop filter, and sensing applications. The final chapter of the thesis presents a summary of the research effort and some conclusions.

Chapter 2

Coupled Mode Theory and Index Gratings in Fiber Optics

Coupled mode theory is a fundamental concept in optical waveguide technology.

The basic principle is that energy can be transferred from one propagating mode to another as long as certain boundary conditions are satisfied. In practice, mode coupling is used in a variety of applications, including lasers, optical splitters, and dispersion compensation techniques. An index grating is one type of passive waveguide structure that is commonly used to achieve mode coupling. Index gratings, which consist of periodic variations in the refractive index of a waveguide, induce wavelength dependent mode coupling and act as intrinsic optical filters. The wavelengths that are filtered from the incident wave are a function of the grating period, the magnitude of the refractive index difference in one period of the grating (i.e. the grating strength), and the refractive index of the surrounding medium. In this chapter, coupled mode theory is discussed and applied to index gratings in fiber optic waveguides. The formulae for the resonant wavelengths of a fiber Bragg grating (FBG) and a long period fiber grating (LPFG) are derived, and the differences between the two types of gratings are discussed.

2.1 - Coupled Mode Theory

Coupled modes can be either contradirectional or codirectional. Contradirectional coupling describes the interaction of two modes traveling in opposite directions, while

codirectional coupling describes the interaction between two modes traveling in the same direction. In a fiber optic cable, the modal interaction can occur between modes within the same core, between core modes and cladding modes, and/or between modes in adjacent cores. The general form of the coupled mode equations for two modes, A and B, is

$$\begin{aligned}\frac{dA}{dz} &= \kappa B e^{i\delta z}, \\ \frac{dB}{dz} &= -\kappa A e^{-i\delta z},\end{aligned}\quad \text{Eq. 2.1}$$

where κ is the coupling coefficient, A and B are the amplitudes of the propagating waves, and δ is the detuning parameter [30-31]. The sign of each equation will depend on which direction the mode is traveling ($+z$ or $-z$). For each additional mode considered, another differential equation can be added, but here, the discussion will be limited to two modes for simplicity and clarity.

Coupling takes place primarily between modes whose phases are matched. The detuning parameter, δ , is used to determine the phase matching condition and is defined as

$$\delta = (\Delta\beta - K) = ((\beta_A - \beta_B) - \frac{2\pi}{\Lambda}), \quad \text{Eq. 2.2}$$

where β_A and β_B are the propagation constants of modes A and B, respectively, and $K=2\pi/\Lambda$ is the wave number defined by the grating period Λ . The propagation constant of each mode can be further defined by the relation

$$\beta = k_0 n_{eff} = \frac{2\pi}{\lambda_0} n_{eff}, \quad \text{Eq. 2.3}$$

where λ_0 is the free space wavelength, and n_{eff} is the effective refractive index seen by the mode as it propagates through the fiber (more details about the effective refractive index will be presented in the next chapter). When the two modes are perfectly phased matched (i.e. $\beta_A - \beta_B = 2\pi/\Lambda$), the detuning parameter goes to zero, and the exponential term in the coupled mode equations is maximized. In theory, the detuning parameter can go to zero, but in practice, it is usually a very small finite value when the phases of the two modes are closely matched. When the detuning parameter is not equal to zero, coupling still occurs, but the exponential term is not maximized. In many cases, the core mode will couple energy to several different modes, each of which has its own propagation constant and requires an additional differential equation in Equation 2.1. The coupling coefficient, κ , the phase relation of the two modes, and the length of interaction will determine how much energy will be transferred from one mode to the other.

The coupled mode equations given in Equation 2.1 can be used as the basis for describing the interaction between two modes passing through an index grating. Index gratings are sections of periodic variations, uniform or nonuniform, in the refractive index of an optical waveguide (i.e. the fiber core in the case of a fiber optic cable). These gratings act as intrinsic filters by coupling energy away from the incident signal at specific wavelengths. There are two main types of index gratings in fiber optics – FBGs and LPFGs. Structurally, both types of gratings are identical except that the periods of Bragg gratings are two orders of magnitude smaller than those of LPFGs ($\sim 10^{-6}$ meters versus $\sim 10^{-4}$ meters, respectively). They each, however, affect an incident signal differently. FBGs induce contradirectional coupling. Light energy from forward propagating modes is transferred to modes traveling in the opposite direction. FBGs are

often referred to as reflection gratings because of this effect. LPFGs, on the other hand, couple energy codirectionally. Energy from the forward propagating incident modes is transferred to either forward propagating cladding or radiation modes depending on the structure of the waveguide. Using the phase matching condition in Equation 2.2, the wavelengths at which coupling occurs in each type of grating can be derived.

2.2 - Fiber Bragg Gratings

When an incident signal encounters a FBG, contradirectional coupling occurs, causing some of the energy from the incident signal to be “reflected” back in the $-z$ direction. In the case of a single mode fiber, the single, forward propagating core mode can couple energy to the core mode traveling in the $-z$ direction, which is most often the case with FBGs, or to cladding modes traveling in the $-z$ direction. Figure 2.1 illustrates contradirectional (a) core mode/core mode coupling and (b) core mode/cladding mode

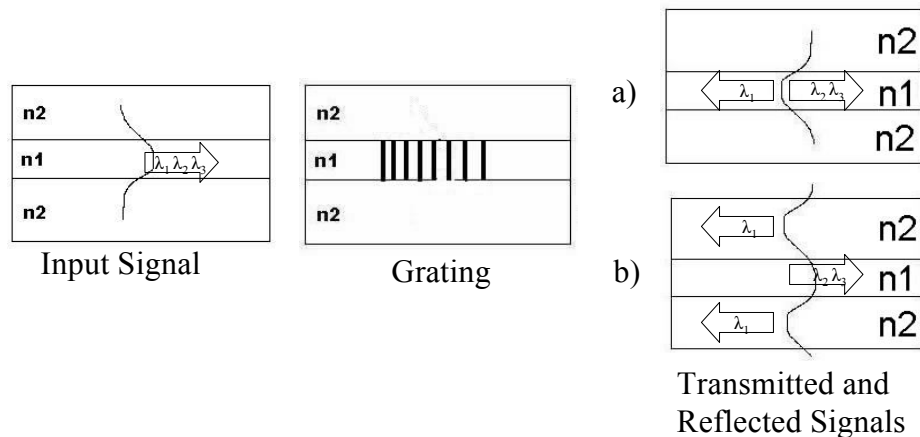


Figure 2.1: Contradirectional coupling in a single mode fiber for a) core mode/core mode coupling and b) core mode/cladding mode coupling.

coupling in a single mode fiber. Assuming that only two modes are interacting, the propagation constants will have different signs because they are traveling in opposite directions. If β_+ is the propagation constant for the core mode traveling in the $+z$ direction and $-\beta_-$ is the propagation constant for the core or cladding mode traveling in the $-z$ direction, the phase matching condition can be rewritten as [32-36]

$$(\beta_+ - (-\beta_-) - \frac{2\pi}{\Lambda}) = (\beta_+ + \beta_- - \frac{2\pi}{\Lambda}) = \frac{2\pi}{\lambda_0} (n_{eff+} + n_{eff-}) - \frac{2\pi}{\Lambda} = 0. \quad \text{Eq. 2.4}$$

The resonant, or filtered, wavelength is found from the phase matching condition by solving for λ ,

$$\lambda = (n_{eff+} + n_{eff-})\Lambda. \quad \text{Eq. 2.5}$$

Since a single mode fiber only has one propagating core mode in each direction, the propagation constants of these two core modes are equal in value but have opposite signs (i.e. $\beta_+ = -(-\beta_-)$). As a result, contradirectional core mode/core mode coupling in a single mode fiber is a special case, and the resonant wavelength can be written as

$$\lambda_B = 2n_{eff}\Lambda. \quad \text{Eq. 2.6}$$

λ_B in Equation 2.6 is often called the Bragg wavelength and is the center wavelength of the frequency band filtered from a signal that passes through a FBG. In fiber optic communication systems, FBGs usually filter signal wavelengths around 1550 nm, and the effective index of the core mode in a single mode fiber is normally around 1.44. Using these values, FBG grating periods are usually on the order of 10^{-6} to 10^{-7} meters.

2.3 - Long Period Fiber Gratings (LPFGs)

Unlike FBGs, LPFGs induce codirectional coupling. Energy transfer occurs between core and cladding modes traveling in the $+z$ direction. However, in single mode fibers, energy cannot be transferred to another mode within the core. Therefore, energy can only be coupled to cladding modes. Figure 2.2 illustrates codirectional coupling in a single mode fiber.

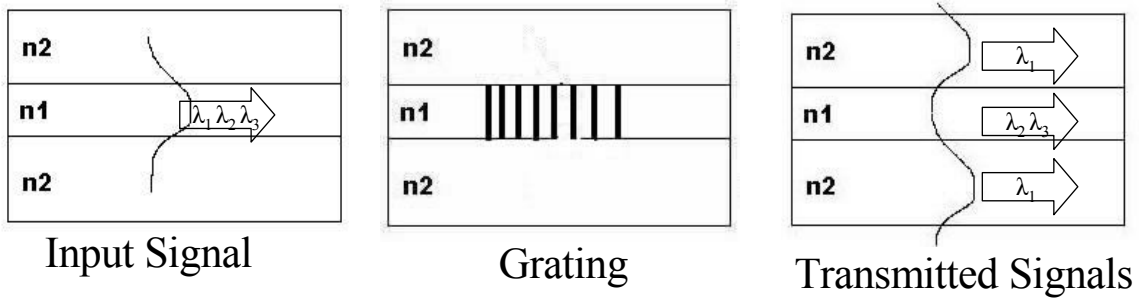


Figure 2.2: Codirectional coupling in a single mode fiber (core mode/cladding mode).

As before, only two forward propagating modes will be considered and each will have their own unique propagation constant. β_{co} is the propagation constant for the incident core mode and β_{cl} is the propagation constant for the interacting cladding mode. The phase matching condition is then written as

$$(\beta_{co} - \beta_{cl}) - \frac{2\pi}{\Lambda} = (\beta_{co} - \beta_{cl} - \frac{2\pi}{\Lambda}) = \frac{2\pi}{\lambda_0} (n_{eff_co} - n_{eff_cl}) - \frac{2\pi}{\Lambda} = 0, \quad \text{Eq. 2.7}$$

and the resonant wavelength of a LPFG in a single mode fiber is

$$\lambda = (n_{eff_co} - n_{eff_cl})\Lambda. \quad \text{Eq. 2.8}$$

As with the FBGs, LPFGs are often fabricated to filter wavelengths around 1550 nm. If $n_{eff_co} - n_{eff_cl}$ is on the order of 10^{-2} to 10^{-3} , the required grating period would be on the order of 10^{-3} to 10^{-4} meters, which is three orders of magnitude greater than the grating period required to filter 1550 nm with a FBG. Thus, LPFGs are so named because their grating periods are two to three orders of magnitude greater than the wavelengths of light that they couple out of the incident signal.

Chapter 3

LPFG Analysis Using a Three-Layer Model

In Chapter 2, coupled mode theory was used to derive the wavelengths filtered from fiber Bragg gratings (FBGs) and long period fiber gratings (LPFGs). The simplified cases presented in the chapter assumed that coupling only occurred between two modes. In reality, however, coupling is not limited to two modes, especially in the case of LPFGs. In single mode fibers, where the mode coupling analysis of FBGs is often limited to the two core modes traveling in opposite directions, LPFGs are capable of coupling energy to several cladding modes, giving rise to multiple resonant wavelengths. This chapter will expand the LPFG analysis presented in Chapter 2 to include the multiple cladding modes found in a single mode fiber. Using the three-layer model presented by Erdogan in reference [36], the effective indices of the core and cladding modes will be calculated, and the transmission spectrum will be simulated. The model will then be used to theoretically verify that (1) a single resonant band can be achieved in the near infrared spectrum (1000 nm to 1700 nm) by reducing the cladding thickness from $\sim 58.45 \mu\text{m}$ to $\sim 13.45\text{-}15.95 \mu\text{m}$ ¹ and (2) the single resonant band can be tuned by

¹ The single mode fibers that are simulated in this chapter and that will be used in our experiments have a total diameter of 125 μm before the cladding layer is reduced. The core radius is approximately 4.05 μm (8.1 μm diameter), and the cladding is 58.45 μm thick (4.05 μm core radius + 58.45 μm cladding thickness = 62.50 μm fiber radius, or 125 μm total diameter). When the cladding layer is reduced to 13.45–15.95 μm , the total fiber diameter will be reduced to 35–40 μm , respectively. When entering information into our models, we often input the fiber core radius and cladding thickness individually. In our simulated output spectra and in our experiments, however, we will primarily refer to the total fiber diameter since that is the measurable fiber parameter.

varying the ambient refractive index. These two aspects will serve as the foundation for the tunable filter design.

3.1 - Three-Layer Model Theory and Calculations

The equation used to find the resonant wavelengths of a LPFG (Eq. 2.8) can be written in the following form to incorporate multiple cladding modes

$$\lambda_j = (n_{\text{eff_co}} - n^j_{\text{eff_cl}})\Lambda, \quad \text{Eq. 3.1}$$

where $n_{\text{eff_co}}$ is the effective index of the core, $n^j_{\text{eff_cl}}$ is the effective index of the j th cladding mode, and Λ is the grating period. While the equation itself is very simple, calculating the required effective indices is difficult and requires an understanding of the mode structure within a fiber optic cable.

An optical mode is defined as a specific solution to the wave equation that satisfies the appropriate boundary equations. The normalized frequency, or V-parameter, is a key parameter in determining what modes propagate in a fiber core and is defined as [35-36]

$$V = k_0 a \sqrt{n_1^2 - n_2^2}, \quad \text{Eq. 3.2}$$

where, $k_0 = 2\pi/\lambda$ is the wave number in free space, a is the radius of the core, n_1 is the

refractive index of the core, and n_2 is the refractive index of the cladding². The cutoff condition for a single propagating core mode is $V = 2.405$, and as V increases, so do the number of core modes that will propagate [36-37]. For the remainder of this discussion, only single mode fibers will be considered.

Although each propagating core mode does not have a unique V number, it can be uniquely determined by its propagation constant, β , which was defined as $\beta = k_0 n_{eff}$ in Chapter 2. Unlike the material refractive index, which is a function of wavelength only, the effective refractive index, or more simply the effective index, is a function of wavelength and fiber geometry. Each core mode propagates with a unique effective index whose value lies between n_1 and n_2 . A core mode ceases to be guided when $n_{eff} < n_2$, at which point it becomes an evanescent mode. The propagation constant can be solved for numerically by taking the parameters used to calculate V (i.e. k_0 , a , n_1 , and n_2) and solving the following dispersion relation [35-38]

$$V\sqrt{1-b}\frac{J_1(V\sqrt{1-b})}{J_0(V\sqrt{1-b})} = V\sqrt{b}\frac{K_1(V\sqrt{b})}{K_0(V\sqrt{b})}, \quad \text{Eq. 3.3}$$

where J_m ($m = 0,1$) is a Bessel function of the first kind, K_m ($m = 0,1$) is a modified Bessel function of the second kind, and b is the normalized propagation constant defined as [34-36]

² A comment must be made on refractive index and the notation that will be used throughout this thesis. In any material, refractive index is a wavelength dependent, complex valued quantity. The real part of the index is a ratio of the speed of an electromagnetic wave in a vacuum to that in the material, and the imaginary part of the index describes the absorption of the material [31]. In this thesis, the focus is on the propagation of light through the fiber, and therefore, any reference to refractive index, unless otherwise noted, refers to the real part of the index. Also, the dispersion of the material is implied in all formulae, so that $n(\lambda)$ will be written as n for simplicity.

$$b = \frac{(\beta/k_0) - n_2}{n_1 - n_2} = \frac{n_{\text{eff_co}} - n_2}{n_1 - n_2}. \quad \text{Eq. 3.4}$$

It is important to note that the dispersion relation presented here uses a linearly polarized (LP) approximation [36]. Under this approximation, the calculation of low order LP modes is sufficient to describe a cylindrical dielectric waveguide, assuming weak guidance [38]. This approximation is used to simplify and reduce the amount of propagation constant calculations [36-38]. The effective index of the core mode is a function of the material indices of the core and the cladding, n_1 and n_2 , respectively, the core radius, a , and the wavelength at which the effective index is to be calculated, λ . For a given wavelength, the effective index is found by solving the dispersion relation (Eq. 3.3) for b and using the result in Equation 3.4 to calculate $n_{\text{eff_co}}$. The dispersion relation can only be solved numerically and can be done fairly quickly using a computer program. Depending on the degree of accuracy required, the effective index can also be approximated by reading it off a plot like the one shown in Figure 3.1. The plot shows b as a function of V with the corresponding effective index shown on the right hand side of the plot. After calculating V using the fiber parameters, the effective index, or its b value, can be read off the plot for the mode of interest [34-35].

As is the case with the effective index of the core mode, the effective indices of the cladding modes must be found using numerical techniques. Unfortunately, the dispersion relation for the cladding modes is considerably more complex. The effective indices of the cladding modes are not only a function of the material indices of the

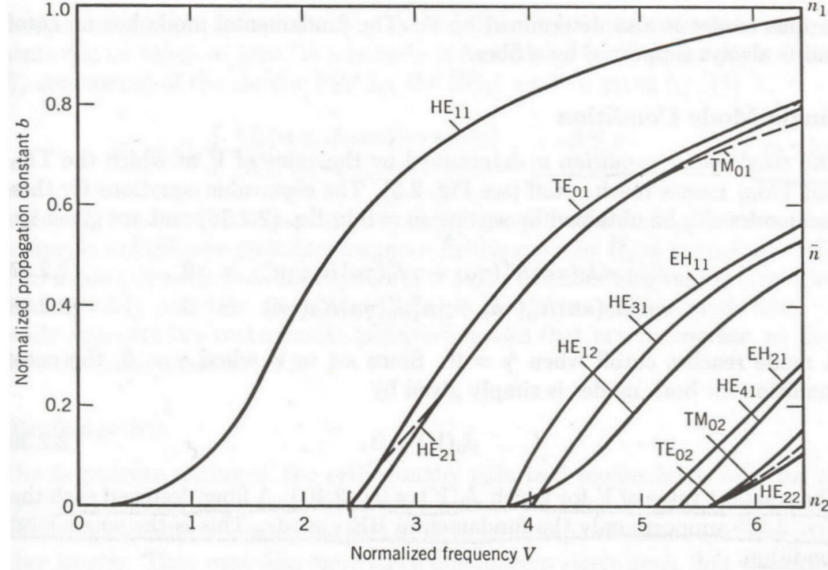


Figure 3.1: The normalized propagation constants, b , and the effective indices, n_{eff} , of a number of modes are plotted as a function of the V-parameter [35].

core (n_1) and cladding (n_2), but also of the ambient index (n_3), the radius of the core (a_1), and the cladding thickness (a_2). The dispersion relation used to calculate the effective cladding indices is [36,40]

$$\zeta_0 = \zeta_0', \quad \text{Eq. 3.5}$$

where

$$\zeta_0 = \frac{1}{\sigma_2} \frac{u_2(JK + \frac{\sigma_1 \sigma_2 u_{21} u_{32}}{n_2^2 a_1 a_2}) p_l(a_2) - K q_l(a_2) + J r_l(a_2) - \frac{1}{u_2} s_l(a_2)}{-u_2(\frac{u_{32}}{n_2^2 a_2} J - \frac{u_{21}}{n_1^2 a_1} K) p_l(a_2) + \frac{u_{32}}{n_1^2 a_2} q_l(a_2) + \frac{u_{21}}{n_1^2 a_1} r_l(a_2)}, \quad \text{Eq. 3.6}$$

$$\zeta_0' = \sigma_1 \frac{u_2(\frac{u_{32}}{a_2} J - \frac{n_3^2 u_{21}}{n_1^2 a_1} K) p_l(a_2) - \frac{u_{32}}{b} q_l(a_2) + \frac{u_{21}}{a} r_l(a_2)}{u_2(\frac{n_3^2}{n_2^2} JK + \frac{\sigma_1 \sigma_2 u_2 u_{32}}{n_1^2 a_1 a_2}) p_l(a_2) - \frac{n_3^2}{n_1^2} K q_l(a_2) - \frac{n_3^2}{n_1^2} K q_l(a_2) + J r_l(a_2) - \frac{n_2^2}{n_1^2 u_2} s_l(a_2)}, \quad \text{Eq. 3.7}$$

and the following definitions have been used,

$$\begin{aligned}
\sigma_1 &\equiv i \ln_{ef} f / Z_0, \\
\sigma_2 &\equiv i \ln_{eff} Z_0, \\
u_{21} &\equiv \frac{1}{u_2^2} - \frac{1}{u_1^2}, \\
u_{32} &\equiv \frac{1}{w_3^2} + \frac{1}{u_2^2}, \\
u_j^2 &\equiv (2\pi/\lambda)^2 (n_j^2 - n_{eff}^2), [j \in (1,2)], \\
w_3^2 &\equiv (2\pi/\lambda)^2 (n_{eff}^2 - n_3^2), \\
J_l &\equiv \frac{J'_l(u_1 a_1)}{u_1 J_l(u_1 a_1)}, \\
K_l &\equiv \frac{K'_l(w_3 a_2)}{w_3 K_l(w_3 a_2)}, \\
p_l(r) &\equiv J_l(u_2 r) N_l(u_2 a_1) - J'_l(u_2 a_1) N_l(u_2 r), \\
q_l(r) &\equiv J_l(u_2 r) N'_l(u_2 a_1) - J_l(u_2 a_1) N'_l(u_2 r), \\
r_l(r) &\equiv J'_l(u_2 r) N_l(u_2 a_1) - J_l(u_2 a_1) N'_l(u_2 r), \\
s_l(r) &\equiv J'_l(u_2 r) N'_l(u_2 a_1) - J_l(u_2 a_1) N'_l(u_2 r).
\end{aligned}$$

In the preceding equations, l is the azimuthal number, Z_0 is the electromagnetic impedance in a vacuum, J_l is a Bessel function of the first kind, K_l is a modified Bessel function of the second kind, N_l is a Bessel function of the second kind, and the prime notation indicates differentiation with respect to the total argument [36,40]. Once the effective indices of both the core and cladding modes have been determined, the resonant wavelengths of an LPFG can be found.

Figure 3.2 is a plot of the effective indices of the core and cladding modes for a 125 μm diameter, single mode fiber. The plots were generated by a program that solved the dispersion relations given above for wavelengths ranging from 1.00 μm to 1.70 μm . The differences between the effective indices of the cladding modes are very small. At a

wavelength of 1.50 μm , for example, a 0.002 difference in index separates the first 10 cladding modes. These small differences cause several resonant peaks to form within the near infrared spectrum. By rearranging the equation for the resonant wavelengths of an LPFG, the effect of the closely spaced cladding modes on the output spectrum of an LPFG can be seen more clearly. Figure 3.3 shows the grating period plotted as a function of wavelength (i.e. $\Lambda(\lambda) = \lambda \Delta n_{0j}(\lambda)$, where Δn_{0j} is the effective index difference between the core mode and the j th cladding mode). The resonant wavelengths of a grating with period Λ are found at the intersections between the horizontal line and the modal lines. The horizontal line drawn in Figure 3.3 corresponds to an LPFG with a 500 μm grating period. Figure 3.4 shows the simulated output spectrum of the grating. The depth of each resonant peak is determined by the coupling coefficient, κ , which is a function of the overlap integral between the radial and azimuthal fields of the core mode and the j th cladding mode. Figure 3.5 shows a plot of the normalized coupling coefficient values. For lower order cladding modes, the coefficients are proportional to the cladding mode number, and coupling between the core and odd cladding modes is much stronger than that between the core and even cladding modes. Figures 3.3 and 3.5 verify these results. Intersections between the horizontal grating period line and the even numbered mode lines do not result in a resonant peak in the output spectrum. Coupling between the core mode and odd numbered modes produces resonant peaks that grow deeper as the cladding mode number increases.

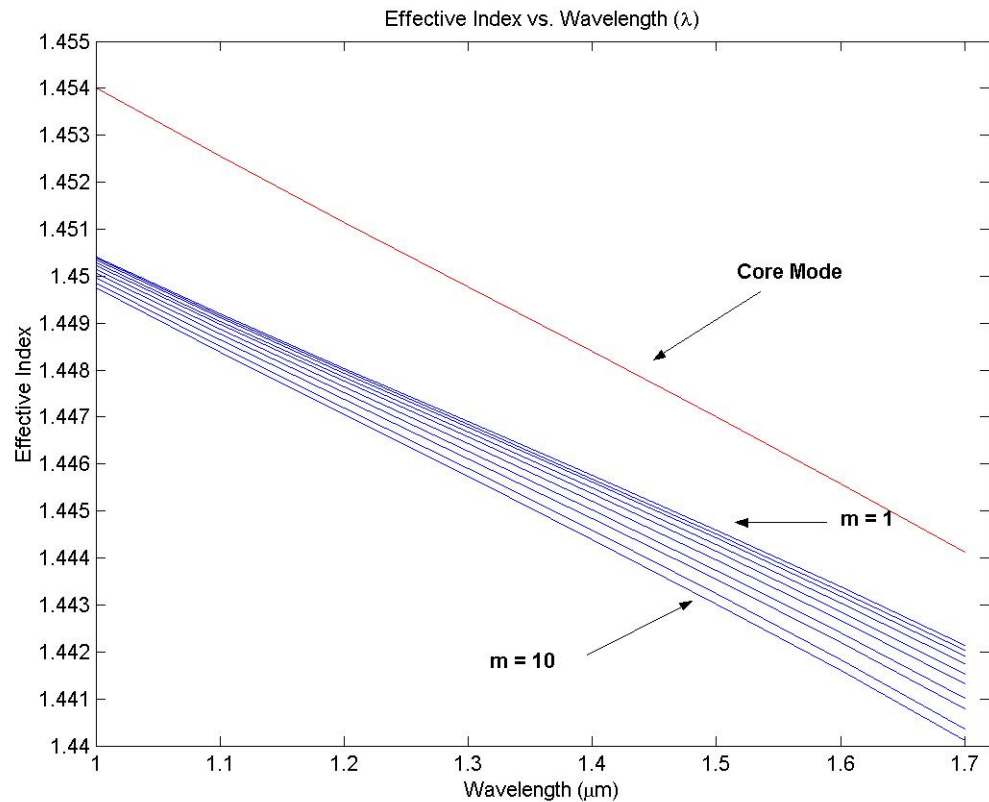


Figure 3.2: Effective indices of the core and cladding modes as a function of wavelength (Fiber diameter = 125 μm).

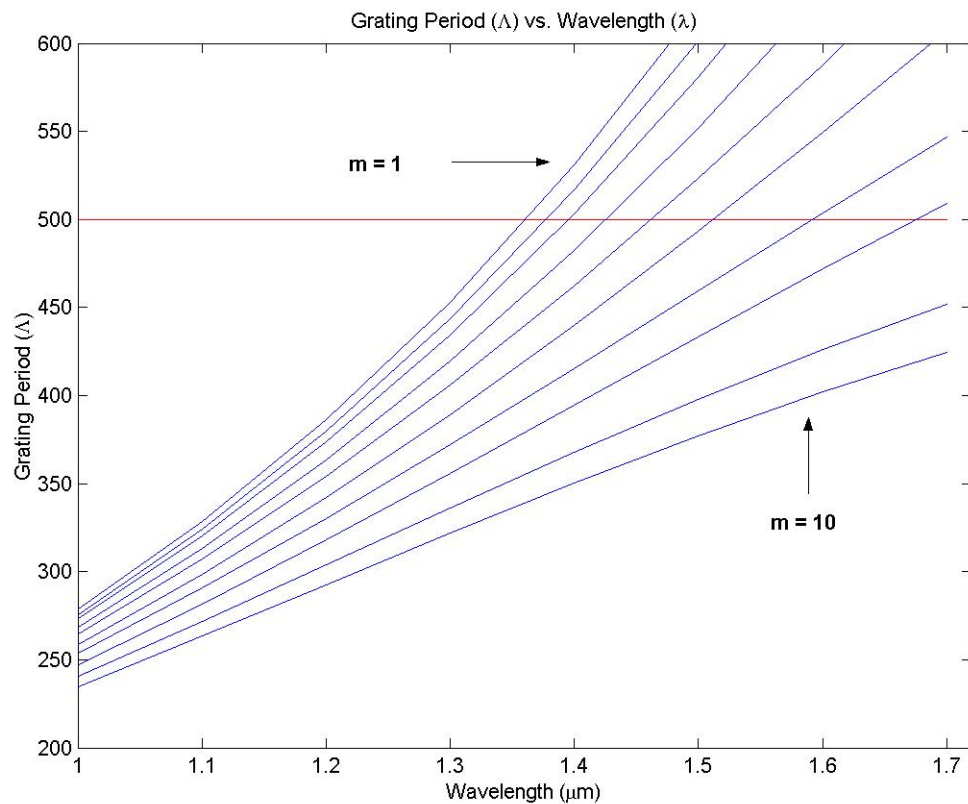


Figure 3.3: Grating period as a function of wavelength (Fiber diameter = 125 μm , $\Lambda = 500$).

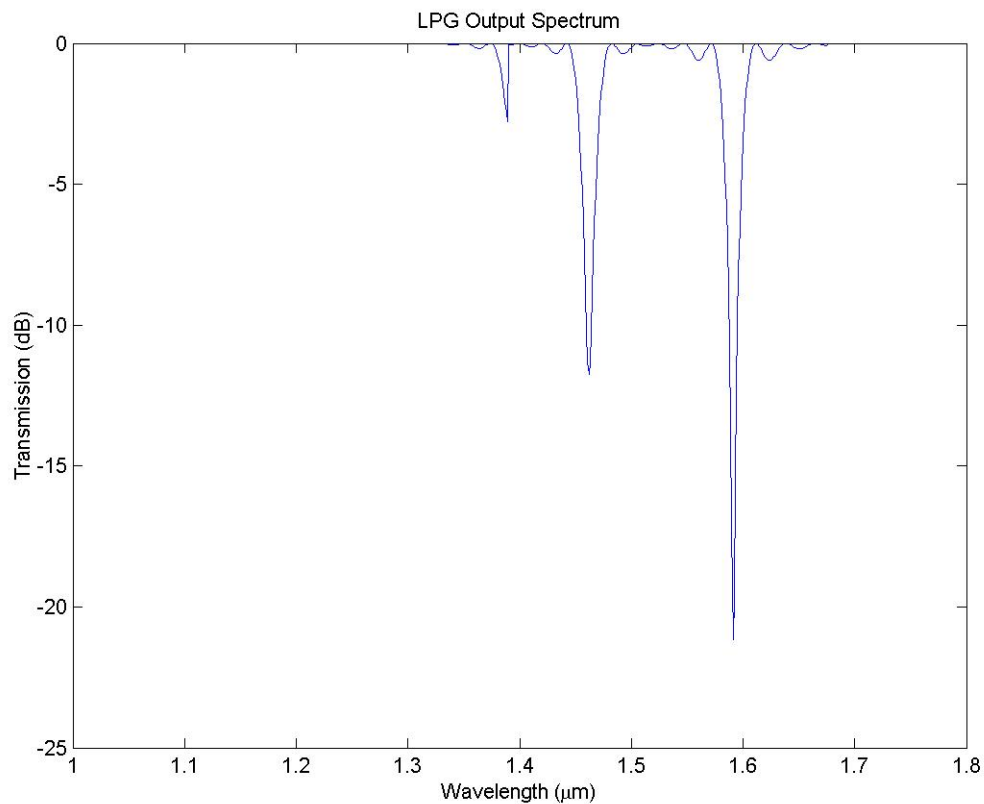


Figure 3.4: LPFG output spectrum (Fiber Diameter = 125 μm , $\Lambda = 500$).

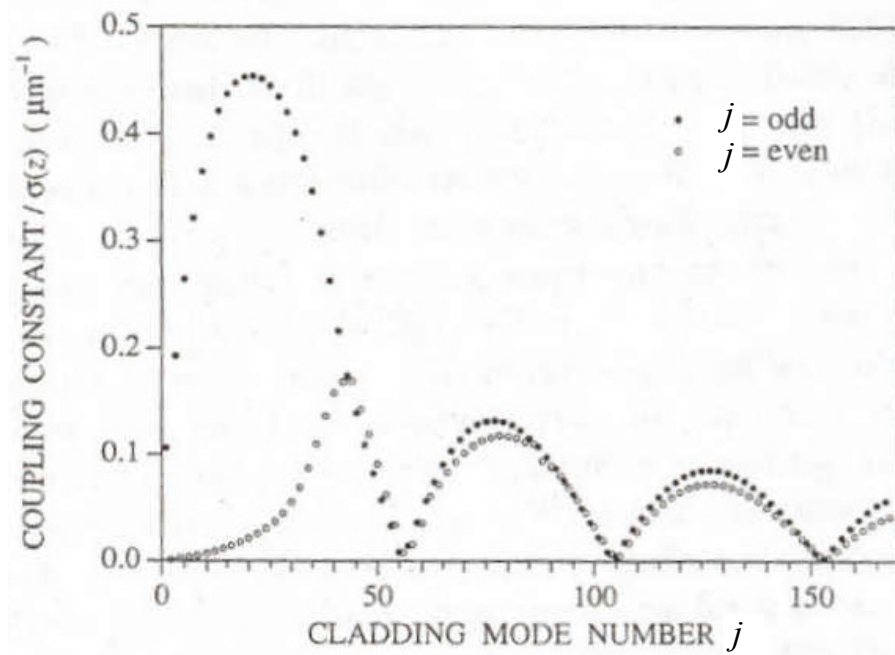


Figure 3.5: The coupling constants, κ , divided by the grating profile, σ , for coupling between the core mode and the j^{th} cladding mode. The even and odd modes are shown separately [36].

3.2 - A Single Resonant Band LPFG

Once the analysis of an LPFG in a 125 μm fiber had been completed, the dispersion relations were resolved using a thin cladding layer ($a_2 = 13.45 \mu\text{m}$). Figure 3.6 shows the effective indices of the core mode and the cladding modes in a 35 μm diameter fiber. A thinner cladding increases the differences between the effective indices in the cladding, thereby increasing the distance between resonant peaks. By comparing Figure 3.6 to Figure 3.2, the increased cladding mode separation is very apparent. At 1.50 μm , where a 0.002 index difference separated the first 10 cladding modes in a 125 μm diameter fiber, a 0.02 index difference separates the first 10 modes in the thin fiber. The effects of this increased mode separation are shown in Figures 3.7 and 3.8. Figure 3.7 shows the grating period as a function of wavelength for a thin fiber, and Figure 3.8 is the output spectrum of a thin cladding LPFG. The analysis of a thin cladding LPFG verified that a single resonant peak over the entire near infrared spectrum (i.e. 1.00 μm to 1.70 μm) could be achieved by reducing the cladding thickness.

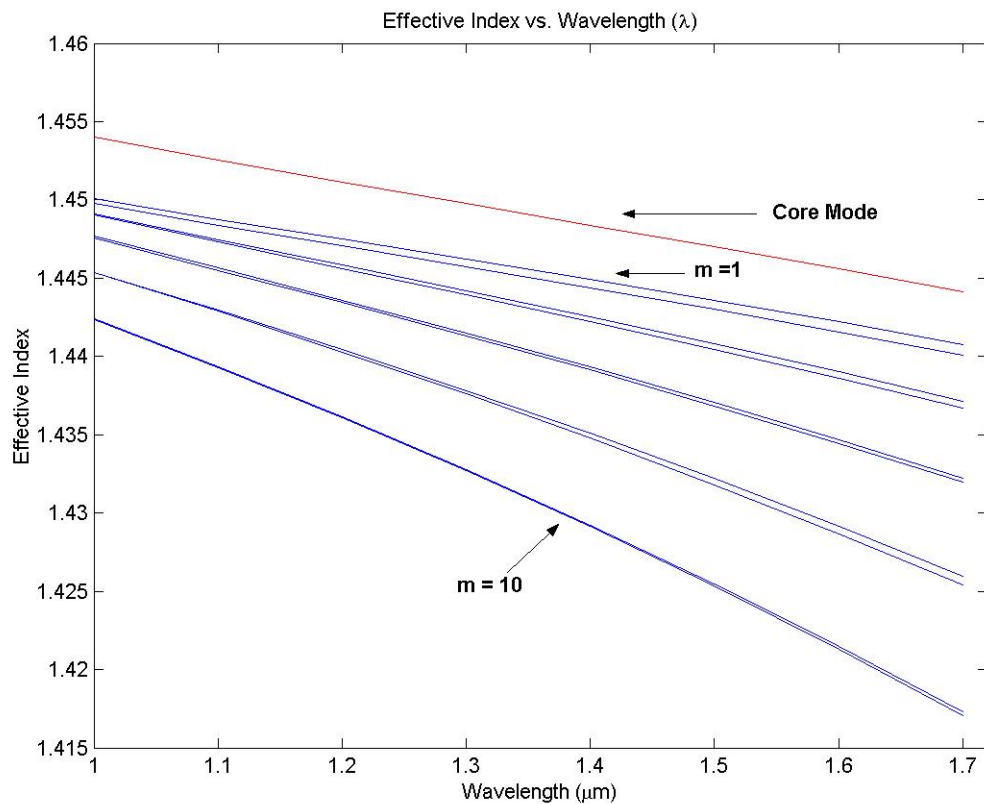


Figure 3.6: Effective indices of the core and cladding modes as a function of wavelength (Fiber diameter = 35 μm).

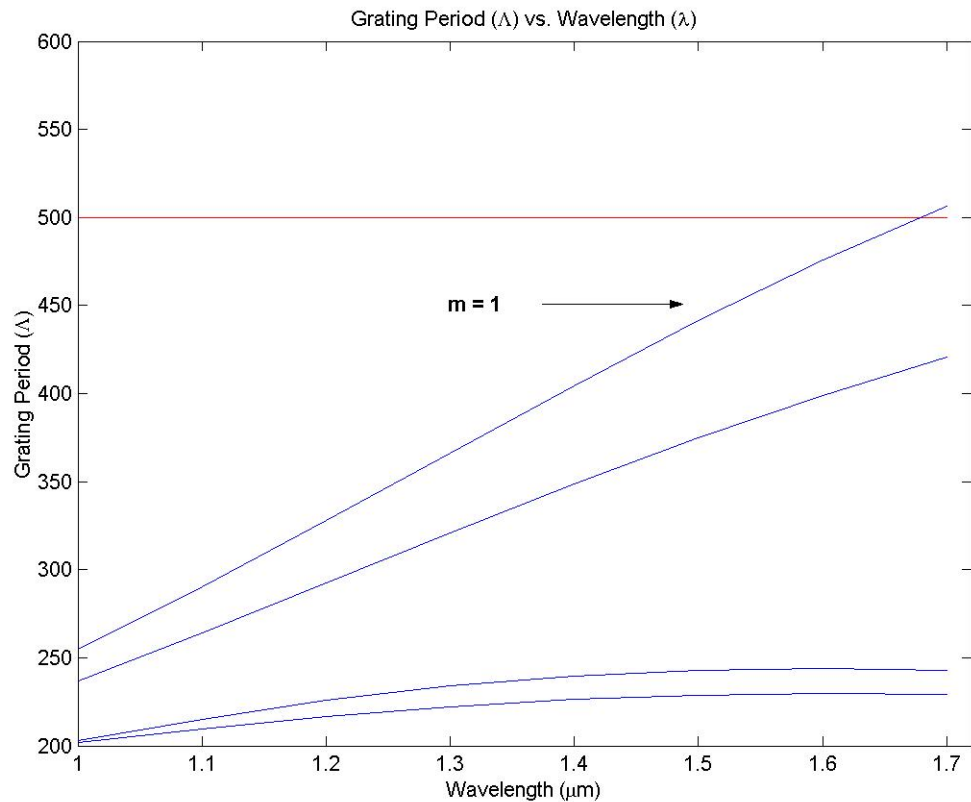


Figure 3.7: Grating period as a function of wavelength (Fiber Diameter = 35 μm , $\Lambda = 500$).

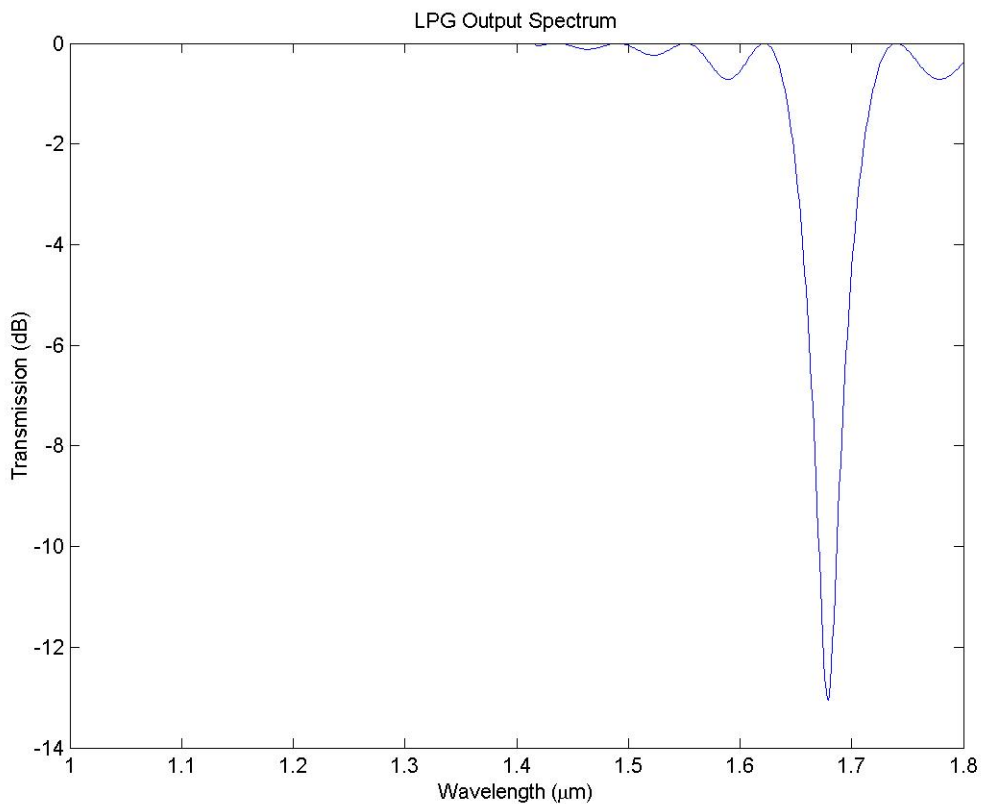


Figure 3.8: LPFG output spectrum (Fiber Diameter = 35 μm , $\Lambda = 500$).

3.3 - LPFG Tuning

The dispersion relations used to calculate the effective indices were collectively named the three-layer model because the refractive indices of three different material layers were needed to perform the calculations. Those three layers were the silica core, the thin silica cladding, and the ambient air. Thus far, all of the plots were generated with the ambient being air ($n_3 = 1.00$). However, the resonant wavelength of an LPFG is not static and can be tuned by varying the ambient index. Assuming that the grating period is fixed, as it is in most cases, the effective indices must be changed to tune the resonant wavelength. The effective core index is a function of the material indices of the core and cladding layers and the core diameter, none of which are changed by reducing cladding thickness or by varying the ambient index. Therefore, the thin cladding LPFG must be tuned by adjusting the effective index of the cladding mode to which light is being coupled. Unlike the effective core index, the effective cladding indices are a function of the cladding thickness and the material index of the ambient, and as a result, the LPFG can be tuned by adjusting the value of the ambient index. Figure 3.10 shows the simulated spectrum of a thin cladding LPFG at several different ambient indices.

In order to experimentally verify that the LPFG could be tuned by varying the ambient index, a $35\text{ }\mu\text{m}$ diameter fiber with a $400\text{ }\mu\text{m}$ period LPFG was immersed in a series of index matching oils. Figure 3.10 shows the LPFG spectra for the various oils. The peak wavelength and peak depth were recorded for each oil, and they were each plotted as a function of the ambient index. The results are shown in Figure 3.11. The top plot shows that the resonant wavelength decreases linearly from 1.00 to 1.40 before

falling sharply to a minimum around 1.45, at which point, it jumps back up to a wavelength near its original position and stays there for indices higher than 1.45. The LPFG is most sensitive to changes in the ambient index when the indices are close to the material index of the cladding (n_2), which is approximately 1.45. The bottom plot shows that the depth of the resonant peak stays fairly constant until the cladding threshold is approached, at which point it begins to decrease. At the cladding threshold, the peak nearly disappears and then slowly begins to increase in depth with the ambient index. The results shown in Figure 3.11 are consistent with the experimental results published by Patrick [22] for a 125 μm diameter fiber with an LPFG (Figure 3.12). One important difference to note is the sensitivity of the two LPFGs around the cladding index. The slope of the curve for the thin cladding LPFG is steeper than Patrick's curve in this region. Thus, the thinner cladding not only reduces the transmission spectrum to a single resonant peak, but it also increases the sensitivity of the peak to changes in the ambient around the cladding threshold.

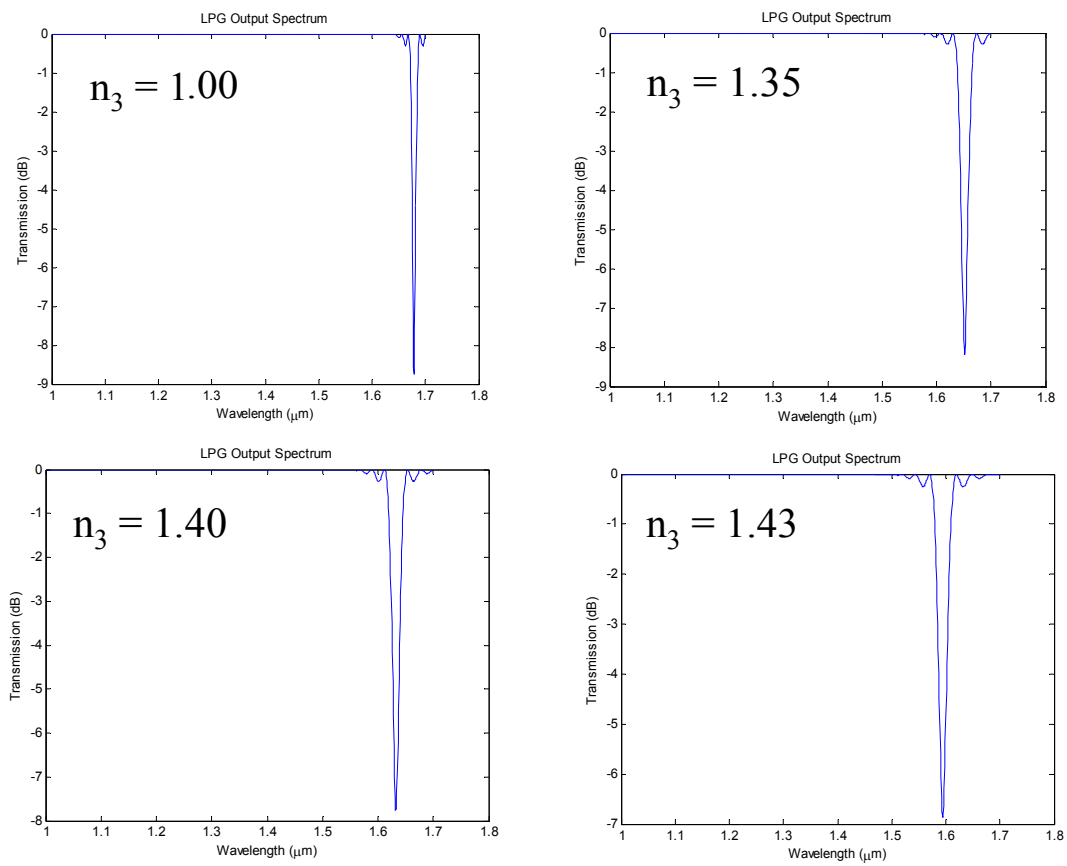


Figure 3.9: The simulated spectrum of a thin cladding LPFG at several different ambient indices.

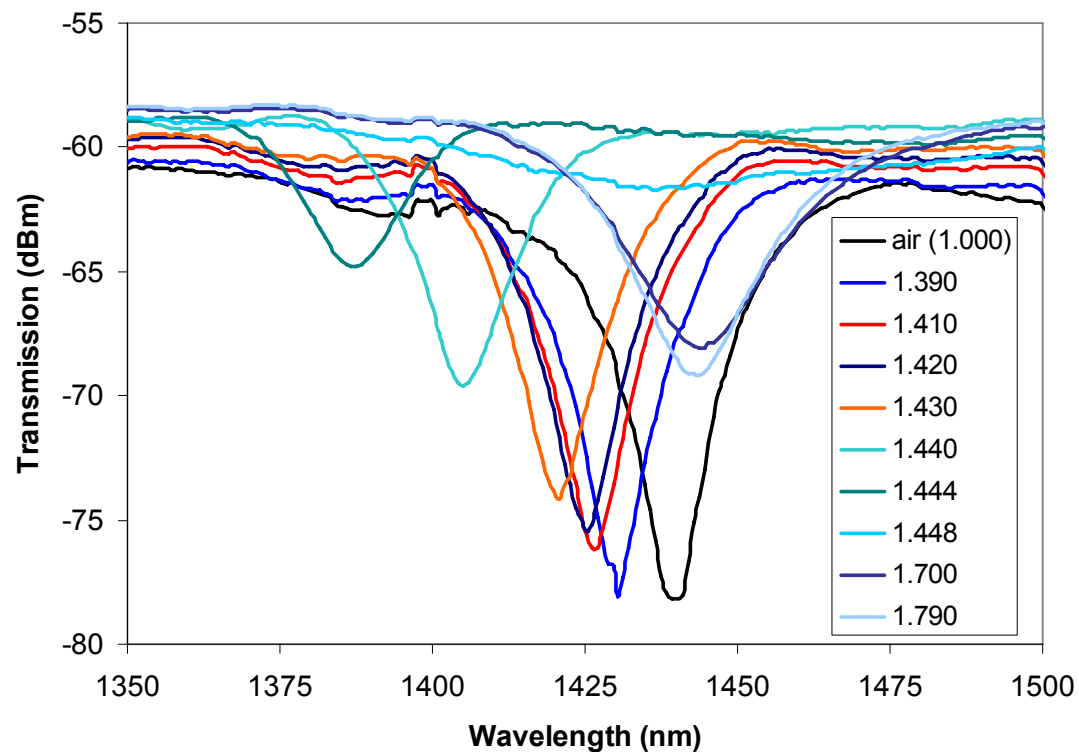


Figure 3.10: LPFG spectra for various index matching oils (Fiber diameter = 35 μm , Λ = 400 μm).

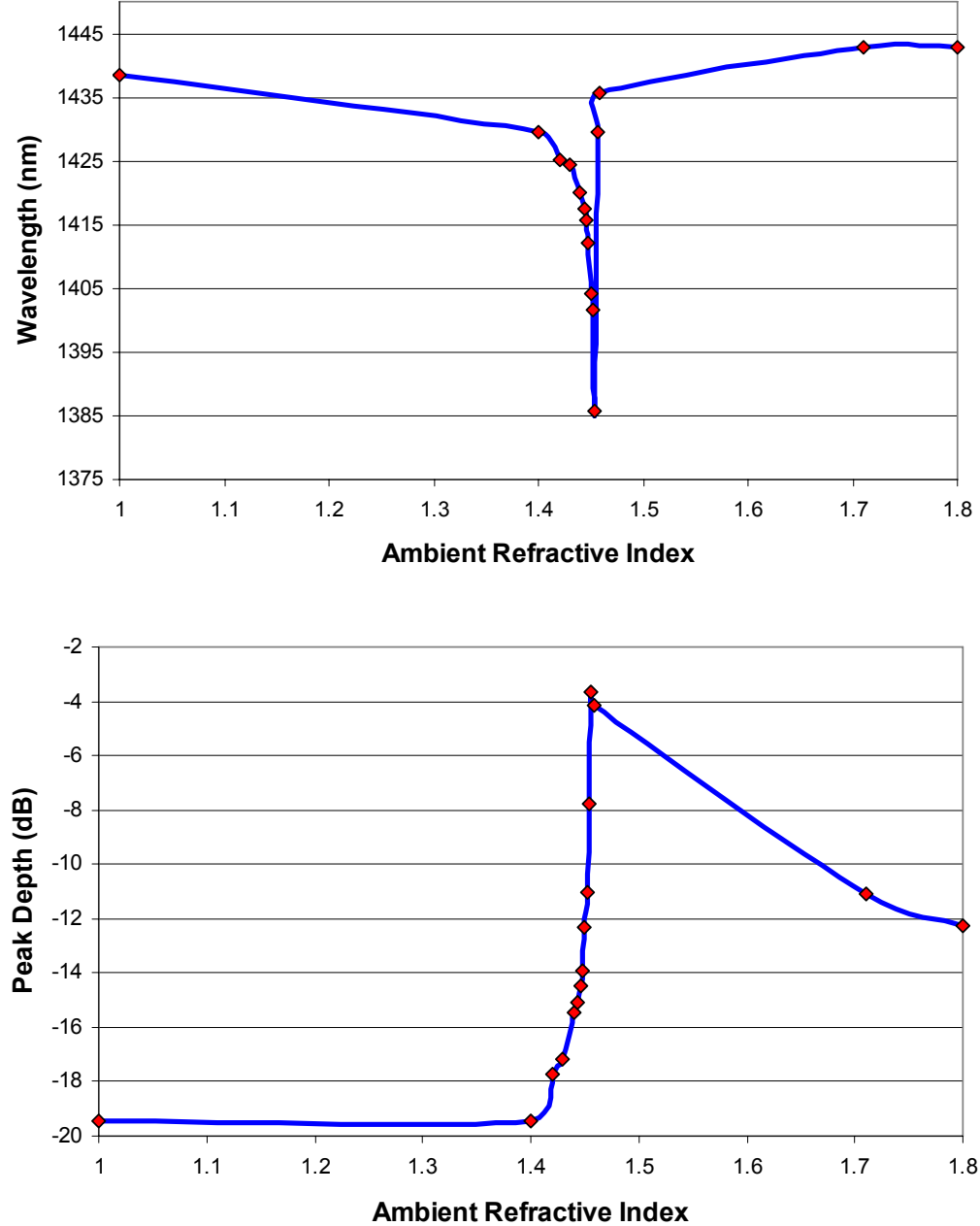


Figure 3.11: Resonant wavelength (top) and peak depth (bottom) as a function of ambient refractive index (Fiber diameter = 35 μm , $\Lambda = 400 \mu\text{m}$).

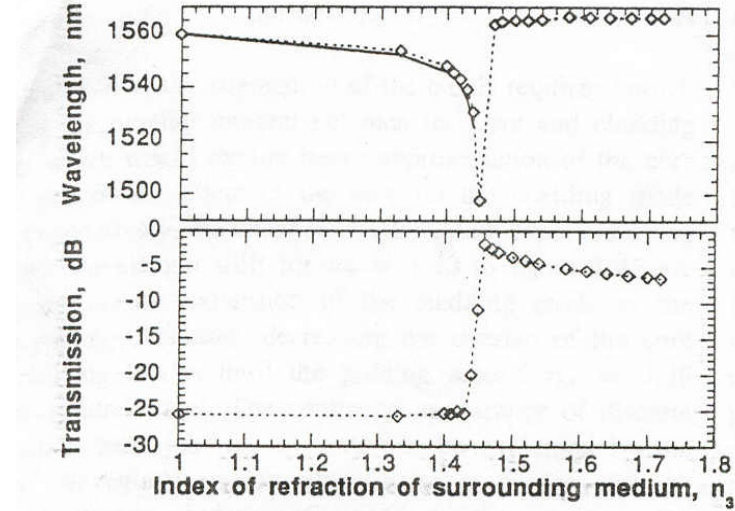


Figure 3.12: Top graph: experimentally measured resonant wavelength of the longest wavelength attenuation band (Fiber diameter = 125 μm , $\Lambda = 275 \mu\text{m}$). Bottom graph: depth of resonant peak as a function of n_3 [22].

Chapter 4

A Tunable Filter Design Based on a Single Resonant Band LPFG

Both the model and experimental results presented in Chapter 3 verified the feasibility of a single resonant band LPFG that could be tuned by varying the ambient refractive index. Using the three-layer model as a guide, an all-fiber tunable filter design was developed. The design is based on a single resonant band LPFG and includes a second cladding layer that is to be made of electro-optic (E-O) polymer [41-48]. The polymer cladding layer serves as the effective ambient, and its refractive index is controlled by an applied electric field. By varying the index of the polymer, the resonant peak of the LPFG is tuned through a range of wavelengths. The basic filter design is shown in Figure 4.1. A thin (~ 50 nm) layer of conductive indium tin oxide (ITO) is sputtered onto the thin cladding LPFG and functions as an electrode. The E-O polymer cladding is then coated onto the electrode and a second electrode layer, either ITO or gold, is applied overtop. The entire device is then packaged into a jacket or protective housing, and two leads are wired out to attach to a power source. The advantages of this design over current filtering technology include (1) faster tuning speeds due to the absence of mechanical movement, (2) a wide tuning range (~ 50 nm), as predicted by the experimental data, and (3) an integrated design that can be spliced directly into a fiber optic system and has low insertion loss.

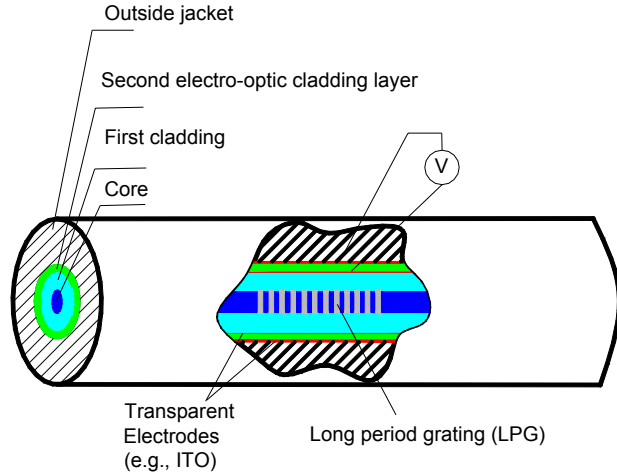


Figure 4.1: An all-fiber, electrically tunable, fiber optic filter based on a single period long period fiber grating with an electro-optic polymer second cladding [16].

4.1 - LPFG Fabrication

Six major steps are required to fabricate the tunable filter and they are shown in Figure 4.2. In order to write LPFGs using a UV laser, the fiber core must first be doped with germanium (Ge) and boron (B) or hydrogen (H) to increase its sensitivity to UV light. Specialty photosensitive fibers (Fibercore PS1500) can be bought commercially, or they can be made by loading conventional fibers under high temperature and pressure. Once the fiber is doped, a section of the polymer jacket is stripped, and the exposed fiber section is subject to high intensity UV radiation through an amplitude mask. The energy imparted by the radiation causes the dopants in the exposed areas of the fiber to react with the silica, which leads to an increase in refractive index. While the LPG is being

written, the evolution of the peaks in the fiber transmission spectrum can be monitored on an optical spectrum analyzer (OSA).

Once the LPFG has been written, the fiber is immersed in a bath of hydrofluoric acid (HF) to etch the cladding. The etch is timed and is also monitored by placing several test fibers in the bath. The test fibers are removed from the bath at fixed intervals to help monitor the etch rate and the cladding thickness. (From our experiences making thin cladding LPFGs, the writing and etching steps are interchangeable.) After the fiber has been etched, an ITO electrode is sputtered directly onto the cladding, and then the E-O polymer layer is applied. The top electrode is coated on the polymer cladding, and the device is packaged. (During the testing stages, the devices are not packaged in order to save time and materials.)

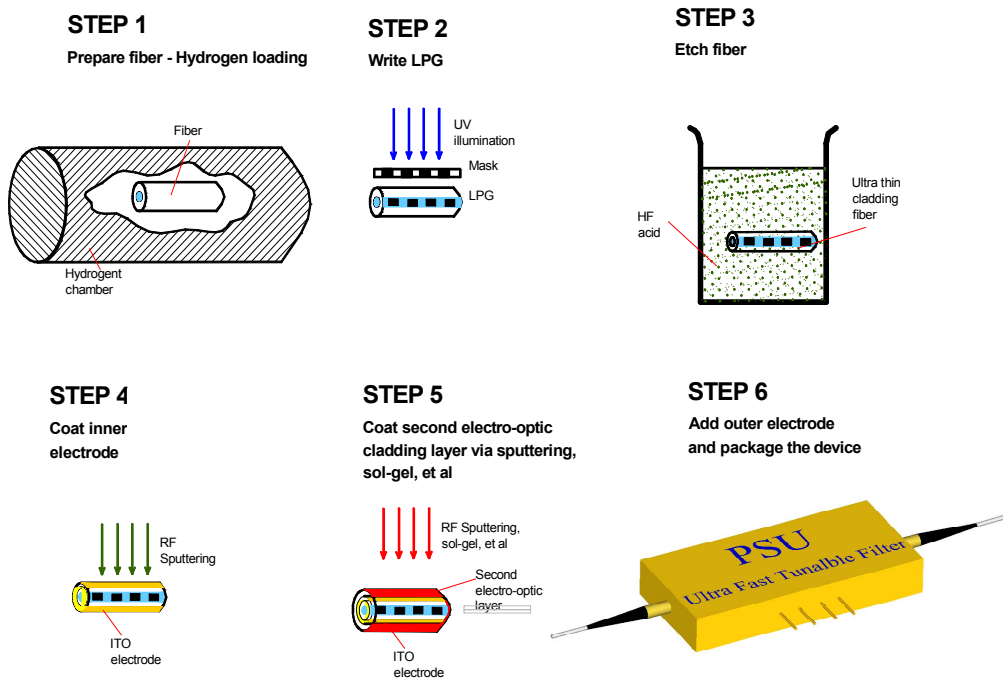


Figure 4.2: The six basic steps required to fabricate the tunable LPFG filter.

4.2 - Filter Testing

The initial LPFG filters that we tested were fabricated using the steps described above. We enlisted the help of an E-O materials group within the electrical engineering department to develop an E-O polymer to tune the LPFGs. Based on the data from the three layer model and our experiments, the polymer cladding must have a native index in the 1.44 range to maximize tuning and must be able to achieve a refractive index change of approximately 1% (i.e. 0.01). Using these guidelines, a ferroelectric relaxor (polyvinylidene fluoride-trifluoroethylene-chlorofluoroethylene) terpolymer, or P(VDF-TrFE-CFE), was chosen to tune the LPFGs. The terpolymer has a native refractive index of 1.41, and a relative refractive index change of -2.6% has been measured under an applied electric field of 80 V/ μ m for free standing films [48]. For clamped films, a 0.52% index change has been measured under an applied electric field of 100 V/ μ m [48]. Figure 4.3 shows the spectrum of an LPFG being tuned by the E-O terpolymer. From the figure, an applied voltage of 42 V/ μ m tuned the spectrum about 18 nm, which is the largest tuning range we achieved using the terpolymer. These results seemed to imply that the native index of the terpolymer was too low to maximize the LPFG tuning range.

In order to achieve a larger tuning range, the refractive index of the terpolymer needed to be increased to match the index of fiber cladding. This could be achieved by adding zinc sulfide (ZnS) nanoparticles into the terpolymer matrix to form a nanocomposite. Due to the high refractive index of ZnS ($n = 2.27$), less than 5% volume fraction is sufficient to achieve index matching. The small particle size and low volume fraction ensures that the material transparency and E-O response will only

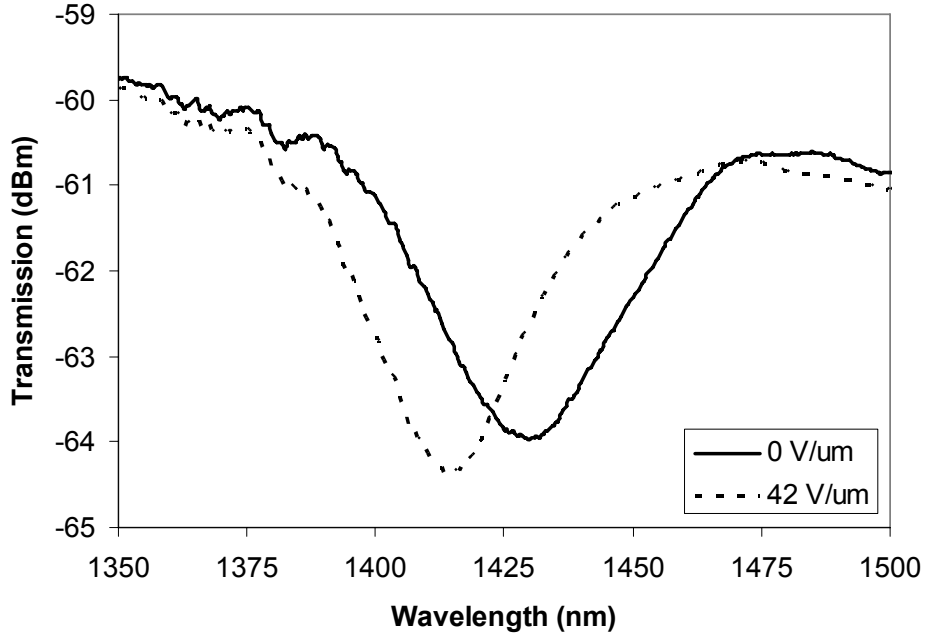


Figure 4.3: The spectrum of a LPFG is tuned 18 nm electro-optically using pure terpolymer.

experience a small amount of degradation. The nanocomposite is coated on the LPFG by a dip-coating process using dimethylformamide (DMF) as a solvent. The coating thickness is controlled by the solution concentration and the drawing rate of the fiber. Figure 4.4 shows the results from using a ~5% volume nanocomposite to tune the LPFG. A tuning range of 10 nm was achieved with an applied voltage of 40 V/ μ m, and there was very little degradation in peak depth or bandwidth. This tuning range was slightly less than what we were able to achieve with the pure terpolymer, but the peak shape and depth were significantly better.

Once we had shown that the nanoparticles did not significantly affect the E-O properties of the polymer, we needed to find the concentration of nanoparticles that would maximize the tuning range. The nanoparticle concentration was varied from 0.5%

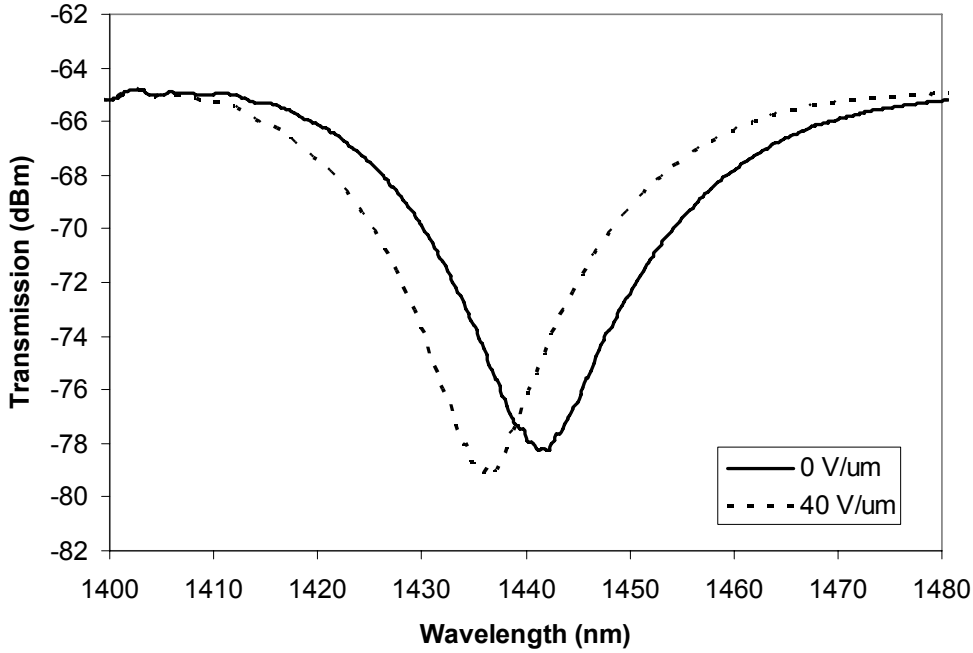


Figure 4.4: The spectrum of a LPFG is tuned approximately 10 nm using a $\sim 5\%$ volume fraction nanocomposite polymer.

volume to up to 5% volume, and the results were varied. In many cases, there was no resonant peak in the transmission spectrum after the composite had been applied. After seeing this result a number of times, we applied a field to the polymer cladding of an LPFGs that had no visible peak. The results are shown in Figure 4.5. Not only did the peak reappear as the field increased, but it also tuned over 50 nm. These results were highly unusual and were significantly different than what had been predicted by the three-layer model and our index oil data.

To better understand the results shown in Figure 4.5, we performed the index matching oils experiment with a thin cladding LPFG that had been coated with ITO, and the results are shown in Figure 4.6. The spectra shown in the figure are similar to those

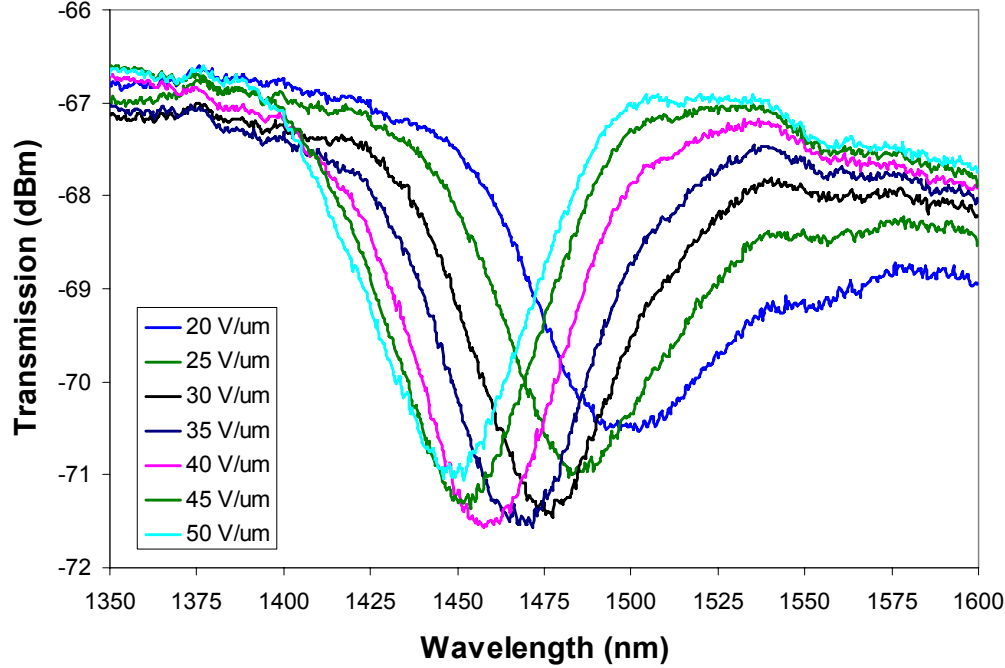


Figure 4.5: A LPFG with a ~1.5% volume nanocomposite cladding had no resonant peak without an applied voltage. As the voltage was increased, the peak reappeared and tuned over 50 nm.

we recorded while tuning the LPFG with the nanocomposite and are in stark contrast to the tuning spectra in Figure 3.10. In air, the resonant peak of the ITO coated LPFG is strong, but as soon as it was immersed in 1.39 index oil, the peak completely disappeared, similar to the case of the nanocomposite coated LPFG with no voltage applied. As the index of the oil was increased to 1.41, the peak reappeared, but the peak wavelength was now longer than it was in the air. The peak continued to deepen as the oil index was increased and tuned over 100 nm. By the time the oil index reached 1.442, the peak depth was slightly deeper than it had been in ambient air. These results were completely opposite from what we had seen in the three layer model, where an increasing ambient index caused the peak to shift to shorter wavelengths and decrease in depth.

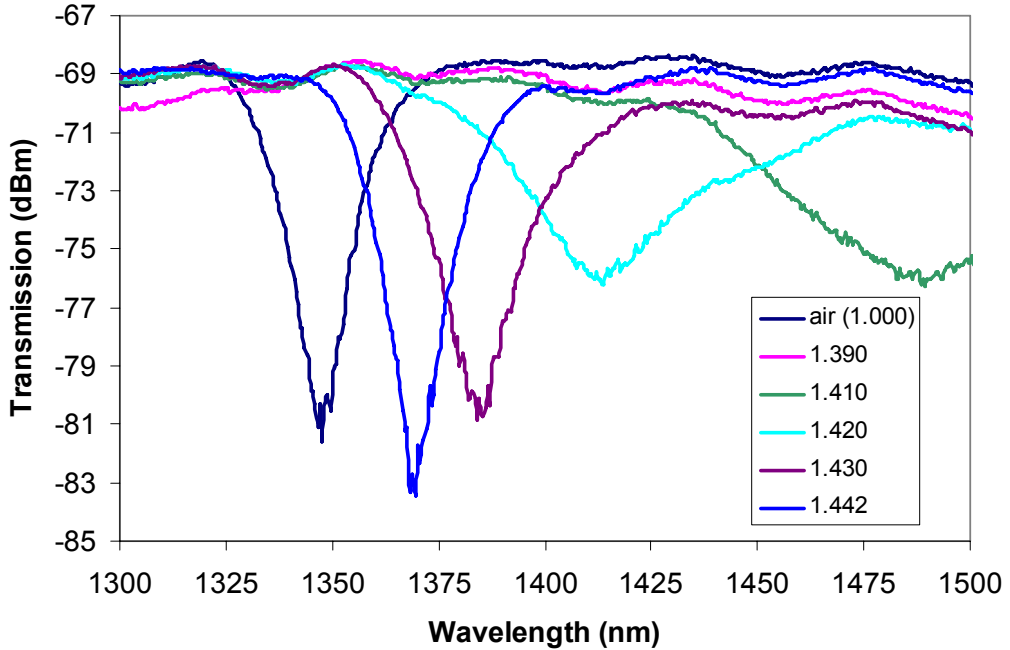


Figure 4.6: The spectrum of a thin cladding, ITO coated LPFG being tuned with index oils. The resonant peak is present in air, but disappears at an ambient index of 1.40. As the index increases, the peak reappears at longer wavelengths and tunes nearly 100 nm. (Fiber diameter = 35 μm , $\Lambda = 400 \mu\text{m}$).

The same index oil experiment was run for multiple LPFGs, and they all displayed the similar tuning characteristics as those shown in Figure 4.6. From these results, we concluded that the ITO layer, which had been neglected in the three-layer model, was causing this tuning behavior. In order to characterize the tunable filter more accurately, a four-layer model that included the ITO layer was needed.

Chapter 5

Cladding Mode Transitions and the Four Layer Model

After observing how the thin ITO layer affected our LPFGs, there were two main issues to address. First, we needed to characterize the ITO films that we were sputtering and look for any research that had been done on LPFGs coated with thin film overlays. Secondly, the three-layer model that we had been using to simulate our tunable filter was no longer accurate, and a model that included the ITO layer was needed.

5.1 - ITO Characterization and Cladding Mode Transitions

When the original tunable filter design was proposed, the thin ITO electrode that was to be coated onto the surface of the LPFG was thought to have negligible effect on the filter characteristics. In the ideal case, this transparent conductive layer would be approximately 50 nm thick (much thinner than the ~1550 nm light that would be passing through the LPFG), and its refractive index would match that of the fiber cladding. However, ITO can be a difficult material to work with because of its complex microstructure, and its optical properties can vary significantly with the deposition conditions and post-deposition processing [49-54]. As a result, we used Jung's paper on ITO depositions to help us determine sputtering conditions that would yield an ITO film with the proper refractive index [50]. Unfortunately, due to the limitations of our



Figure 5.1: The Anatech Hummer XII sputtering system used to perform our ITO depositions.

sputtering system and the sensitivity of the photosensitive fibers to high temperatures, we could not duplicate the conditions in the paper and had to make some concessions.

We used an Anatech Hummer XII sputtering system, shown in Figure 5.1, to deposit our ITO films. This is an older sputtering system and does not have some of the features that newer systems have to prevent contamination and to control film quality. In particular, it does not have a load lock, and the actual sputtering chamber is opened any time we load or unload fibers. By exposing the chamber to the atmosphere after every deposition, contaminants are routinely allowed into the sputtering environment. Since the ITO films were only 50-100 nm thick, small amounts of contamination could significantly affect the quality of the films. Additionally, the configuration of this system only allows for a single working gas, and the controls used to regulate the flow of the working gas into the sputtering chamber are all analog, not digital, as is the case in many

newer systems. These two aspects of our system are significant because of the ITO's high sensitivity to fluctuations in the chamber conditions during deposition. In many applications that use ITO, the films only need to be transparent and have a certain minimum conductivity. The optical properties of the film do not need to be exact. However, in the case of the tunable filer, where the ITO film thickness, refractive index, and conductivity are all being considered, small variations in the gas mixture or chamber pressure affect all of these properties [49-51]. The lack of a digital control system with feedback, in particular, was much more detrimental to the consistency our films than not being able to introduce multiple gases into the chamber during deposition. With the analog controls on the Hummer system, it was very difficult to achieve the exact same pressure conditions during each deposition, and some fluctuations in the refractive index and deposition rate were inevitable. This limitation was made worse by having to sputter the fibers one side at a time. The fibers are loaded into a caddy and placed on a flat stage for sputtering. After one side has been sputtered, the caddy is flipped and the process is repeated. Since the fibers are cylindrical and have to be coated using two separate depositions, the thickness of the ITO layer on the fiber surface is not completely uniform, and the optical properties of the layer may vary from one side to the other.

While these factors affect the quality and uniformity of our films, the biggest concession we had to make was to sputter at room temperature. When the photosensitive fibers are subject to elevated temperatures ($> 125^{\circ}\text{C}$) for a significant amount of time, the dopants that are responsible for the change in refractive index tend to anneal out, destroying the grating. This is a major limitation because sputtering at high temperatures ($100\text{-}500^{\circ}\text{C}$) can greatly reduce the refractive index of a sputtered ITO film - the higher

the temperature, the lower the index [49-51]. Furthermore, post-deposition anneals at temperatures in 300-400 °C range, which have been shown to improve the optical and electronic properties of ITO films, could not be implemented [51-54].

Given these limitations, we sputtered ITO films onto glass slides and pieces of silicon wafer using different conditions and measured their characteristics (i.e. refractive index, thickness, and conductivity). Many of the trends reported in references [49-51] held for our films, but all of the film indices were substantially higher than the ~ 1.444 index of the fiber cladding. The lowest index that we could achieve at room temperature was ~ 1.888 at 632 nm. The chamber pressure and sputtering power used to achieve this refractive index were 10 mTorr of pure argon, and 5 mW, respectively. The ellipsometer that we used to measure the refractive index of our ITO films used a helium-neon laser, which has a wavelength that is less than half of the 1550 nm light that is most commonly used in fiber optic communications. Based on the data in Jung's paper, we estimated the ITO refractive at 1550 nm to be about 1.80.

In addition to characterizing the ITO films from our sputtering machine, we also looked for any related research on coated LPFGs. We found a number of publications that dealt with thin film overlays on LPFGs [25-30]. While most of the papers examined overlays on 125 μm fibers, the published results gave us better insight into how the ITO layer was affecting the fiber modes, and thus, the tunability of our LPFG. The references identified cladding mode transitions that occur as a result of an LPFG being coated with a high index overlay (i.e. an overlay with refractive index higher than that of the cladding).

Figure 5.2 was taken from reference [25] and shows the effective indices of the

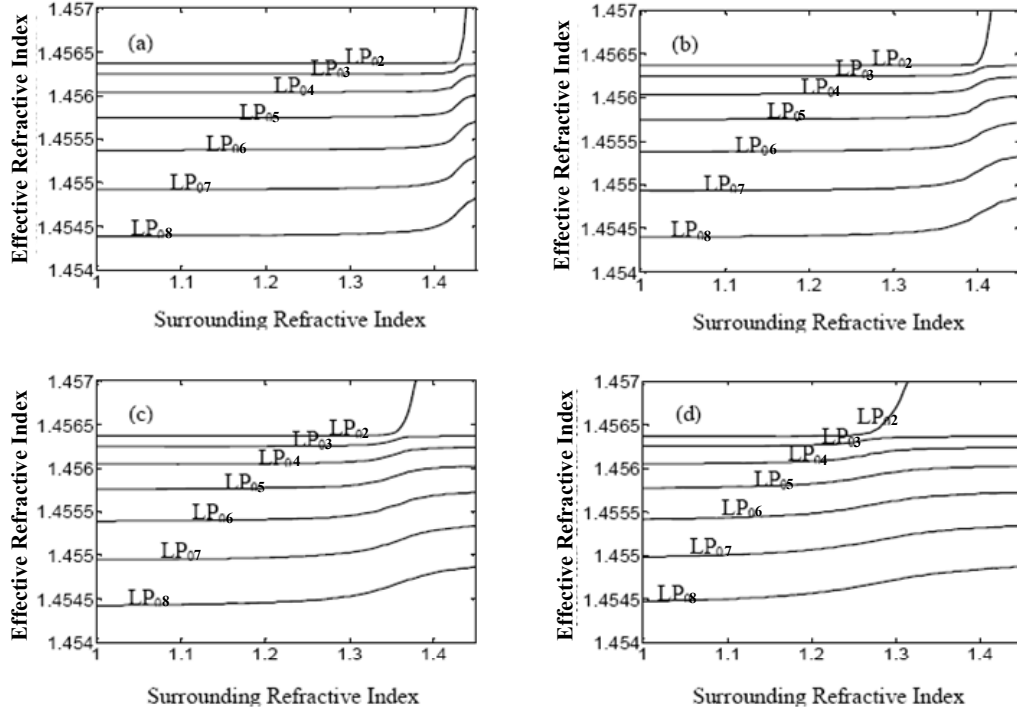


Figure 5.2: Effective refractive indices of the LP₀₂-LP₀₈ cladding modes versus the surrounding refractive index in a high refractive index coated fiber with: (a) 150 nm thin film; (b) 200 nm thin film; (c) 250 nm thin film; and (d) 300 nm thin film [25].

LP₀₂-LP₀₈ cladding modes of an LPFG coated with a high index overlay as a function of the surrounding refractive index. The plots in Figure 5.2 show that as the surrounding index increases, the cladding modes shift out of the cladding and become overlay modes. The lower order modes are the first to transition, and the higher order modes shift within the cladding to replace the mode that has moved out. The surround index at which this transition occurs is a function of the overlay refractive index and thickness. The overlay refractive index for the plots shown is 1.578, which is still lower than the ~ 1.80 index films produced by our sputtering system [25]. In terms of the transmission spectrum, these results substantiate the experimental data that we recorded with the index matching oils (Figure 4.6). At a certain oil index (~ 1.400 in the case of Figure 4.6), the resonant

peak disappeared because the cladding mode to which the core mode was coupling shifted to the overlay. As the oil index increased, a new resonant peak formed at a higher wavelength because the core mode began coupling to a higher order cladding mode that was moving in to replace the lower order mode that had transitioned out. When the modes had fully transitioned, the final location of the resonant peak was at a wavelength that was slightly higher than resonant peak in air because the higher order mode does not quite reach the position once occupied by the lower order mode.

Since the mode transition references all considered 125 μm diameter LPFGs [25-30], we sputtered several 40 μm diameter LPFGs with different thicknesses of ITO to see how the thin cladding affected the mode transitions. (In all of the experiments described in the last chapter, we had used 35 μm diameter fibers. After refining our LPFG fabrication setup and working with ITO coated fibers, however, we found that we could produce stronger LPFGs with more consistent peak positions, depths, and tuning ranges in a slightly thicker fiber. Additionally, the added thickness made the fibers slightly stronger and reduced the number of samples that we broke.) Figure 5.3 shows a plot of coated LPFGs' peak wavelengths as a function of the ambient index for different thicknesses of ITO. Knowing that a shift in resonant wavelength will accompany a cladding mode transition, the data in Figure 5.2 showed us that the mode transition moved to a lower ambient index as the ITO thickness was increased (as was the case for 125 μm LPFGs). The data also showed us that the tuning ranges of our LPFGs were affected by the ITO thickness. A much larger tuning range could be achieved by using a thinner ITO overlay. However, the added tuning range that is gained by reducing

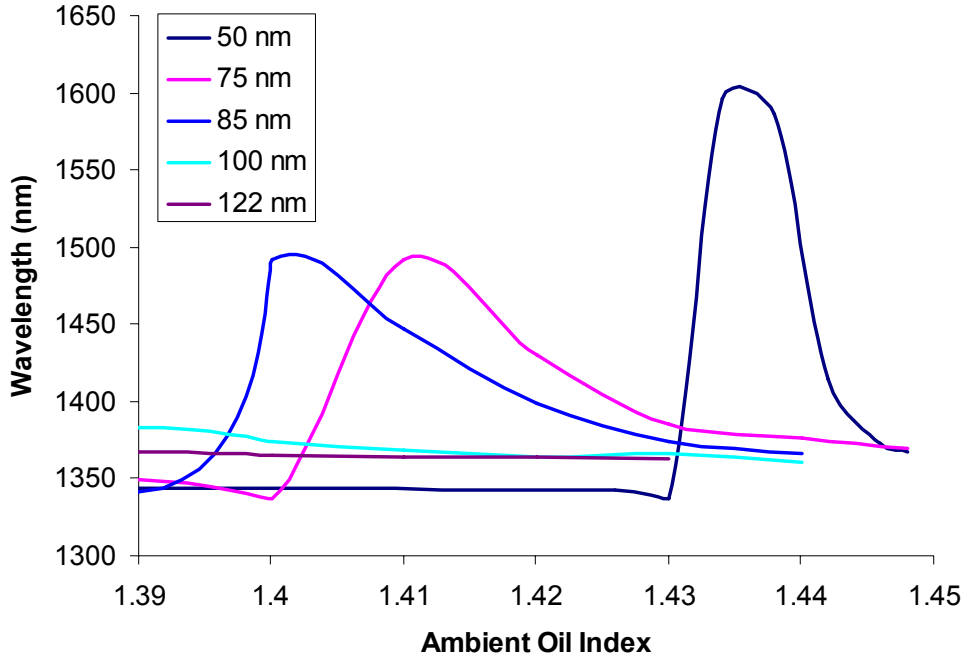


Figure 5.3: Measured LPFG resonant wavelengths as a function of the ambient index for different ITO thicknesses. (Fiber diameter = 40 μm , $\Lambda = 400 \mu\text{m}$).

the thickness of the ITO overlay must be kept in perspective. The data shown in Figure 5.3 is only based on the resonant wavelength position, not the depth of the peak. A practical LPFG based tunable filter must have a consistent peak depth across the range of operating wavelengths. Additionally, there is a limit to how thin the ITO overlay can be. The resistance of the ITO layer is inversely proportional to its thickness, which will affect the switching speed of an electro-optically tunable LPFG. When optimizing the ITO layer, all of these factors must be considered, but given our sputtering capabilities and the results in Figure 5.3, we used a 50 nm ITO layer in our experiments. Of the sample LPFGs that we made (all of which are not shown), a 50 nm ITO layer produced the most consistent results in terms of tuning performance and can be deposited in the least amount of time.

5.2 - Theoretical analysis of the four-layer model

Although the reference papers helped us understand the mode transition phenomenon, we still needed a way to analyze the effects of an arbitrary high index ITO layer on our thin cladding LPFG. A new model was needed to quantitatively analyze our filter and guide our research. Figures 5.4(a) and 5.4(b) are cross-sectional views of the LPFG filter design, which includes six layers: (1) the silica core layer, (2) the thin silica cladding layer, (3) the inner ITO electrode layer, (4) the electro-optic polymer layer, (5) the outer metal electrode layer, and (6) the surrounding medium.

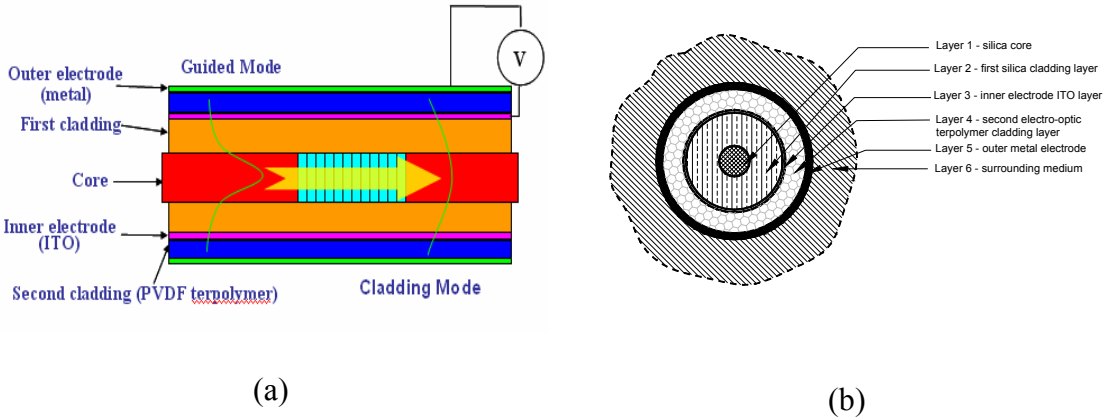


Figure 5.4: (a) Schematic structure of the E-O tunable LPG filter, (b) Cross-sectional view of the E-O tunable LPG filter [20].

For an uncoated LPFG, phase matching between the core mode and the i^{th} forward-propagating cladding mode is achieved at resonant wavelengths given by [31-40]:

$$\frac{2\pi}{\lambda} (n_{eff}^{co-1} - n_{eff}^{cl-i}) + s_o (\tau_{l,l} - \tau_{i,i}) = \frac{2\pi}{A} \quad \text{Eq. 5.1}$$

where n_{eff}^{co-1} is the effective refractive index of the core mode, n_{eff}^{cl-i} is the effective refractive index of the i^{th} radial order cladding mode in the thin silica cladding layer, s_o is

the coefficient of the first Fourier component of the grating, $\tau_{l,l}$ and $\tau_{i,i}$ are the self-coupling coefficients of the core and the i^{th} cladding modes, respectively, and Λ is the grating period. (The simplified version of the phase matching condition (Eq. 2.8) is derived from Equation 5.1 by assuming that the core mode is only interacting with a single cladding mode and that the self coupling coefficients of the two modes are equal.) In Chapter 3, a three-layer model was used to show that the effective refractive indices of the silica cladding modes, n_{eff}^{cl-i} , are strongly dependent on the refractive index of the outside layers. Thus, the resonant wavelength of the LPFG can be tuned by adjusting the refractive index of the layer(s) surrounding the cladding. Strictly speaking, n_{eff}^{cl-i} depends on the refractive indices of all outside layers (i.e., layers 3-6, as shown in Figure 5.4(b)). However, the influence from layers 5 and 6 is assumed to be negligible because they are sufficiently far (ten or more wavelengths in this case) from the silica cladding layer. As a result, a four-layer model that only considers layers 1-4 is sufficient to analyze the tuning characteristics of the filter.

Two main steps are needed to simulate the performance of our LPFG filter. First, the propagation constants and mode profiles of the core and cladding modes are determined. Second, the coupling coefficients between the core and cladding modes are found using coupled mode theory. A couple different approaches have been taken to perform these calculations [36-40,55-58]. Erdogan created a three-layer model that incorporated the LP approximation to precisely solve for the fields propagating through an LPFG [36,56]. In Chapter 3, this model was used to verify that a thin cladding LPFG would have a single resonant band in its output spectrum and would have an increased

sensitivity to changes in the ambient refractive index. Another approach, developed by Anemogiannis et al [39], used the Transfer Matrix Method together with the LP approximation to solve for eigenmodes. Unfortunately, neither method is well suited to model our multi-layer structure. Erdogan's approach is mathematically rigorous, computationally intensive, and is difficult to extend to four layers. Additionally, the LP approximation used to simplify Erdogan's calculations was originally meant for weakly guiding fibers where the difference in index between the core and cladding layers was small. In our case, the difference between the core and cladding layers is small, but the same cannot be said about the cladding and ITO layers. As a result, the LP approximation may reduce the accuracy of our model and a more rigorous calculation should be used. The Transfer Matrix Method provides a viable alternative for simulating LPFGs because it is less computationally intensive for numerical solvers, and additional layers can be added easily. However, Anemogiannis' formulation still relies on the LP approximation. Since we needed a model that could simulate structures with an arbitrary number of layers with an arbitrary refractive index profile while maintaining relatively high calculation speed, our group developed a four-layer model that combined the matrix method for eigenmode calculation introduced by Yeh [55] and the coupled mode method presented by Erdogan [36,56].

The following description shows how the matrix method and the coupled mode method are combined to create our four-layer model. First, the equations for the electric and magnetic fields in a cylindrical fiber are fit into 4x4 matrices using the matrix method adapted from Yeh [55]. After specifying the boundary conditions, a numerical solver, such as MATLAB, is used to find the field distributions and propagation constants

for the modes of interest. Using this information, we can see how the modal field distributions are affected by the addition of an ITO layer and determine the propagation constants, which are substituted into the coupled mode equations to find the coupling coefficients, as well as the LPFG resonant wavelength, transmission, and relative bandwidth.

In an optical fiber, the electric field along the propagation direction (longitudinal component) has a general form of $E_z(r, \theta, z, t) = E_z(r)e^{iv\theta}e^{i\beta z}e^{-i\omega t}$, where r, θ, z are the radial, azimuthal, and axial cylindrical variables; v is the azimuthal order of the mode; β is the propagation constant of the mode; ω is the angular frequency of the propagating light, and $E_z(r)$ is the radial dependence of the longitudinal component, which is governed by the following Bessel's equation:

$$\frac{d^2 E_z(r)}{dr^2} + \frac{1}{r} \frac{dE_z(r)}{dr} + [(\{k_i n_i\}^2 - \beta^2) - \frac{\nu^2}{r^2}] E_z(r) = 0 \quad \text{Eq. 5.2}$$

where $\beta = k_i n_{eff_i}$ for the i^{th} layer. By solving Equation 5.2, the longitudinal electric field components for an $m+1$ layer fiber are [20,55-57]:

Layer 1:

$$E_z^{(1)} = C_1 J_\nu(p_1 r) \quad \text{Eq. 5.3}$$

Layer i ($i = 2, 3, \dots, m$)

$$E_z^{(i)} = C_i J_\nu(p_i r) + C'_i Y_\nu(p_i r) \quad \text{Eq. 5.4}$$

Guided Wave Solution ($n_{\text{eff},i} < n_i$)

$$E_z^{(i)} = C_i I_\nu(q_i r) + C'_i K_\nu(q_i r) \quad \text{Eq. 5.5}$$

Evanescence Wave Solution ($n_{\text{eff},i} > n_i$)

Layer $m+1$:

$$E_z^{(m+1)} = C'_{m+1} K_\nu(q_{m+1} r) \quad \text{Eq. 5.6}$$

where $p_i = (k_i n_i)^2 - \beta^2$, $q_i = \beta^2 - (k_i n_i)^2$, n_i is the material refractive index of the i^{th} layer, J_ν is a Bessel function of the first kind, Y_ν is a Bessel function of the second kind, I_ν is a modified Bessel function of the first kind, and K_ν is a modified Bessel function of the second kind. A derivation similar to the one presented above can be used to find the longitudinal components of the magnetic field. The longitudinal field solutions are then substituted into the following transverse-longitudinal relations [20,57]:

$$E_r = -\frac{1}{p_i^2} \left(\frac{\nu \omega \mu_0}{r} H_z - j\beta \frac{\partial E_z}{\partial r} \right) \quad \text{Eq. 5.7}$$

$$E_\theta = -\frac{1}{p_i^2} \left(j\omega \mu_0 \frac{\partial H_z}{\partial r} + \frac{\beta \nu}{r} E_z \right) \quad \text{Eq. 5.8}$$

to find the radial and azimuthal field components.

After electric and magnetic fields of the first layer have been found, the longitudinal (z) and azimuthal (θ) components can be rewritten in a matrix form as [20,55]:

$$\begin{pmatrix} E_z^{(l)}(r) \\ -jH_z^{(l)}(r) \\ E_\theta^{(l)}(r) \\ -jH_\theta^{(l)}(r) \end{pmatrix} = M_l(r) \begin{pmatrix} C_l \\ D_l \\ C'_l \\ D'_l \end{pmatrix} \quad \text{Eq. 5.9}$$

where:

$$M_l(r) = \begin{pmatrix} J_\nu(p_l r) & 0 & 0 & 0 \\ 0 & J_\nu(p_l r) & 0 & 0 \\ -\frac{\beta\nu}{p_l^2 r} J_\nu(p_l r) & \frac{\omega\mu_0}{p_l} J'_\nu(p_l r) & 0 & 0 \\ \frac{n_l^2 \epsilon_0 \omega}{p_l} J'_\nu(p_l r) & -\frac{\beta\nu}{p_l^2 r} J_\nu(p_l r) & 0 & 0 \end{pmatrix} \quad \text{Eq. 5.10}$$

is the transfer matrix for the first layer. According to electromagnetic boundary conditions, these two field components must be continuous at the layer boundaries, which allow us to write the field coefficients in subsequent layers as:

$$M_i(r_i) \begin{pmatrix} C_i \\ D_i \\ C'_i \\ D'_i \end{pmatrix} = M_{i+1}(r_i) \begin{pmatrix} C_{i+1} \\ D_{i+1} \\ C'_{i+1} \\ D'_{i+1} \end{pmatrix}, \quad i = 1, 2, 3 \dots m \quad \text{Eq. 5.11}$$

Using this method, the field coefficients in any layer can be expressed by those in the adjacent layer. Additionally, the fields must be finite at both $r=0$ and $r=\infty$, meaning that the coefficients in the first and last layers must satisfy $C'_l = D'_l = C_{m+1} = D_{m+1} = 0$, assuming that there are $m+1$ total layers. Once the boundary conditions are satisfied, fields in the first layer can be expressed by those in the last layer by multiplying the transfer matrices of each layer [20,55]:

$$M_1(r_1) \begin{pmatrix} C_1 \\ D_1 \\ 0 \\ 0 \end{pmatrix} = M_2(r_1) M_2^{-1}(r_2) \cdots M_m(r_{m-1}) M_m^{-1}(r_m) M_{m+1}(r_m) \begin{pmatrix} 0 \\ 0 \\ C'_{m+1} \\ D'_{m+1} \end{pmatrix} \quad \text{Eq. 5.12}$$

Equation 5.12 produces a set of four equations containing four variables and the complete matrix equation can be expressed as:

$$\begin{pmatrix} J_v(p_1 r_1) & 0 & -M_{13} & -M_{14} \\ 0 & J_v(p_1 r_1) & -M_{23} & -M_{24} \\ -\frac{\beta \nu}{p_1^2 r_1} J_v(p_1 r_1) & \frac{\omega \mu_0}{p_1} J'_v(p_1 r_1) & -M_{33} & -M_{34} \\ \frac{n_1^2 \epsilon_0 \omega}{p_1} J'_v(p_1 r_1) & -\frac{\beta \nu}{p_1^2 r_1} J_v(p_1 r_1) & -M_{43} & -M_{44} \end{pmatrix} \begin{pmatrix} C_1 \\ D_1 \\ C'_{m+1} \\ D'_{m+1} \end{pmatrix} = 0. \quad \text{Eq. 5.13}$$

In order for it to have a non-trivial solution, the determinant of the coefficient matrix must be zero:

$$\begin{vmatrix} J_v(p_1 r_1) & 0 & -M_{13} & -M_{14} \\ 0 & J_v(p_1 r_1) & -M_{23} & -M_{24} \\ -\frac{\beta \nu}{p_1^2 r_1} J_v(p_1 r_1) & \frac{\omega \mu_0}{p_1} J'_v(p_1 r_1) & -M_{33} & -M_{34} \\ \frac{n_1^2 \epsilon_0 \omega}{p_1} J'_v(p_1 r_1) & -\frac{\beta \nu}{p_1^2 r_1} J_v(p_1 r_1) & -M_{43} & -M_{44} \end{vmatrix} = 0 \quad \text{Eq. 5.14}$$

and by setting the determinant equal to zero and solving, the propagation constants, β , can be obtained. After solving for the propagation constants, the field components can be determined from the equations. When compared to other methods, the advantage of this matrix formalism is that as the number of layers increases, it is only necessary to manipulate 4x4 matrixes, which is much more efficient than solving the large matrices that arise when solving for all the boundary conditions directly.

Once the field components are obtained, the LPFG parameters can be calculated using coupled mode theory [25,30,36,39,57]. The coupling between different modes in a fiber can be described by the following coupled mode equations:

$$\frac{dA_\mu}{dz} = -j \sum_v A_v (K_{v\mu}^t + K_{v\mu}^z) \exp[-j(\beta_v - \beta_\mu)z] + B_v (K_{v\mu}^t - K_{v\mu}^z) \exp[j(\beta_v + \beta_\mu)z] \quad \text{Eq. 5.15}$$

$$\frac{dB_\mu}{dz} = j \sum_v A_v (K_{v\mu}^t - K_{v\mu}^z) \exp[-j(\beta_v + \beta_\mu)z] + B_v (K_{v\mu}^t + K_{v\mu}^z) \exp[j(\beta_v - \beta_\mu)z] \quad \text{Eq. 5.16}$$

where A and B are the amplitudes of the interacting modes; μ and v are the orders and β is the propagation constant of a certain mode, respectively. K^t and K^z are the transverse and longitudinal coupling coefficients defined by [25,30,36,39,57]:

$$K_{v\mu}^t = \omega \iint \Delta\epsilon \vec{E}_v^t \cdot \vec{E}_\mu^{t*} \quad \text{Eq. 5.17}$$

$$K_{v\mu}^z = \omega \iint \frac{\Delta\epsilon \cdot \epsilon}{\Delta\epsilon + \epsilon} \vec{E}_v^z \cdot \vec{E}_\mu^{z*} \quad \text{Eq. 5.18}$$

where ϵ and $\Delta\epsilon$ are the permittivity and permittivity variations, respectively. However, in our model we will only consider the transverse coupling coefficient because the transverse components of the electric field are significantly larger than their longitudinal counterparts. As a result, the longitudinal coupling coefficients can be considered negligible, and we can recast Equation 5.17 in cylindrical coordinates as:

$$K_{v\mu}^t(z) = \frac{\omega}{4} \int_0^{2\pi} d\phi \int_0^\infty r dr \Delta\epsilon(r, z) \vec{E}_v^t(r, \phi) \cdot \vec{E}_\mu^t(r, \phi) \quad \text{Eq. 5.19}$$

We can obtain an expression for $\Delta\epsilon$ from the refractive index profile the grating structure, which is expressed as [25,30,36,39,57]:

$$n(r, z) = n_0 \left\{ 1 + \sigma(z) \left[1 + m \cos\left(\frac{2\pi}{\Lambda} z\right) \right] \right\} \quad \text{Eq. 5.20}$$

where n_0 is the original refractive index of the fiber core, $\sigma(z)$ is the slow varying envelope of the refractive index modulation, and m is the induced-index fringe modulation, where $0 \leq m \leq 1$. The maximum induced index change at any z along the grating is $\sigma(z)n_0(1+m)$ and the minimum induced index change is $\sigma(z)n_0(1-m)$. Since the LPFGs that we are considering are uniform, $\sigma(z)$ is constant, and we can use [25,30,36,39,57]

$$\Delta\epsilon = \epsilon_0 \Delta(n^2) \approx 2\epsilon_0 n_0 \Delta n = 2\epsilon_0 n_0 [n_0 \sigma(1 + m \cos \frac{2\pi}{\Lambda} z)] \quad \text{Eq. 5.21}$$

to approximate the transverse coupling coefficient as:

$$K_{\nu\mu}^t(z) = \tau + 2\kappa \cos \frac{2\pi}{\Lambda} z \quad \text{Eq. 5.22}$$

$$\kappa = \frac{m}{2} \tau$$

where τ is a “dc” coupling constant and κ is an “ac” coupling constant. The general equation for τ can be expressed as [25,30,36,39,57]:

$$\tau_{\nu\mu} = \frac{\omega \epsilon_0 n_0^2 \sigma}{2} \int_0^{2\pi} d\phi \int_0^{r_l} r dr \vec{E}_{\nu t} \cdot \vec{E}_{\mu t} \quad \text{Eq. 5.23}$$

where r_l is the core radius.

For LPFGs, we need to calculate coupling constants for core mode/core mode coupling and core mode/cladding mode coupling. Coupling between two cladding modes is neglected because it is much weaker than the other two cases. The core/core coupling constant is found by solving [25,30,36,39,57]:

$$\tau_{0l-0l}^{co-co} = \omega \epsilon_0 n_0^2 \sigma \pi \int_0^{r_l} r dr (|E_r^{co}|^2 + |E_\phi^{co}|^2) \quad \text{Eq. 5.24}$$

and the core/cladding coupling constant is:

$$\tau_{0l-lv}^{co-cl} = \omega \epsilon_0 n_0^2 \sigma \pi \int_0^{r_l} r dr (E_r^{cl} E_r^{co*} + E_\phi^{cl} E_\phi^{co*}) \quad \text{Eq. 5.25}$$

In the case of core/cladding coupling (Eq 5.25), the azimuthal integral is:

$$\int_0^{2\pi} d\phi \exp[i(l-1)\phi] = 2\pi \delta_{ll} \quad \text{Eq. 5.26}$$

where δ_{ll} is a delta function that is equal to 1 when $l = 1$ and 0 when $l \neq 1$. Using this integral, the only nonzero coupling constants are those between the core mode and the $l = 1$ cladding modes.

To simplify the model and reduce the number of calculations, we will assume that the core mode only couples to one cladding mode at a time, and we rewrite the coupled mode equations (Eqs. 5.15 and 5.16) as:

$$\frac{dA^{co}}{dz} = iK_{0l-0l}^{co-co} A^{co} + iK_{lv-0l}^{cl-co} A_v^{cl} \exp[i(\beta_v^{cl} - \beta^{co})z] \quad \text{Eq. 5.27}$$

$$\frac{dA_v^{cl}}{dz} = iK_{0l-lv}^{co-cl} A^{co} \exp[i(\beta^{co} - \beta_v^{cl})z] \quad \text{Eq. 5.28}$$

By solving these equations, the transmission of an LPFG can be expressed as [25,30,36,39,57]:

$$T = \cos^2\left(\sqrt{\kappa^2 + \hat{\sigma}^2}L\right) + \frac{\hat{\sigma}^2}{\hat{\sigma}^2 + \kappa^2} \sin^2\left(\sqrt{\kappa^2 + \hat{\sigma}^2}L\right) \quad \text{Eq. 5.29}$$

where,

$$\kappa = \kappa_{lv-0l}^{cl-co} = \kappa_{0l-lv}^{co-cl*} = \frac{m}{2} \tau_{0l-lv}^{cl-co}, \quad \text{Eq. 5.30}$$

$$\hat{\sigma} = \frac{\tau^{co-co}}{2} + \delta, \quad \text{Eq. 5.31}$$

and

$$\delta = \frac{1}{2} \left(\beta^{co} - \beta_v^{cl} - \frac{2\pi}{\Lambda} \right) \quad \text{Eq. 5.32}$$

From Equation 5.29, much of the useful LPFG information can be determined, including the on-resonance transmission:

$$T = \cos^2(\kappa L) \quad \text{Eq. 5.33}$$

the resonant wavelength:

$$\lambda_0 = \frac{n_{eff}^{co} - n_{eff}^{cl}}{1 - \tau^{co-co} \frac{\Lambda}{2\pi}} \Lambda; \quad \text{Eq. 5.34}$$

and the relative bandwidth for weak gratings

$$\frac{\Delta\lambda}{\lambda} = \frac{2}{N}. \quad \text{Eq. 5.35}$$

It is important to note that although the LP approximation is not used in our model, three key assumptions have been made to simplify our calculations. Those assumptions are:

1. Neglect all off-resonant modes.
2. Neglect longitudinal mode coupling.
3. Neglect cladding/cladding coupling.

Using the four layer model described above, we calculated the transversal mode field distributions of the first three cladding modes of a fiber with and without an ITO overlay (Figures 5.5-5.7). In ambient air, the mode field distributions in the ITO coated fiber are nearly identical to those in the uncoated fiber. The field intensities of the 1st and 3rd cladding modes in the core region are much higher than that of the 2nd cladding mode. Since the coupling constant between the core mode and a given cladding mode is proportional to the overlap of their transversal fields, the coupling between the core mode

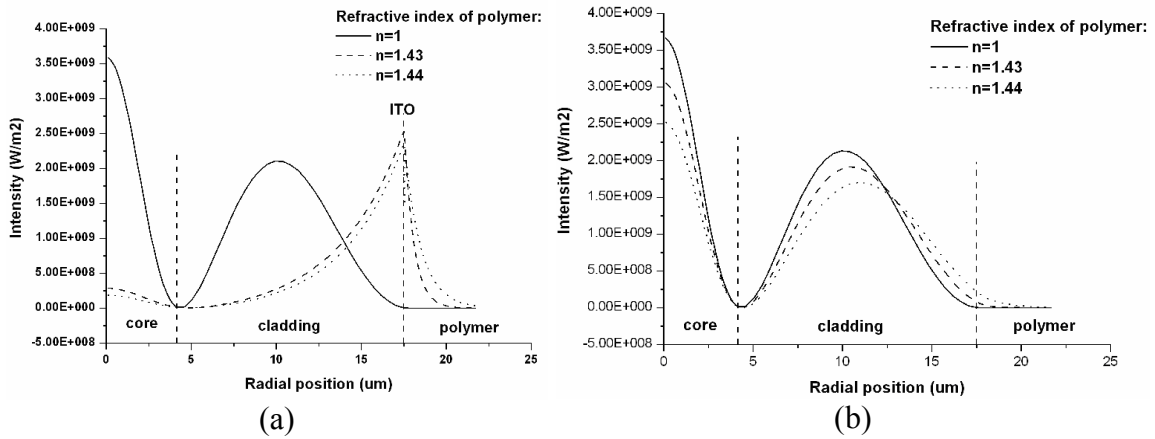


Figure 5.5: Transversal electric field distributions of the 1st cladding mode (a) with ITO ($n = 1.80$ at 1550 nm) and (b) without ITO.

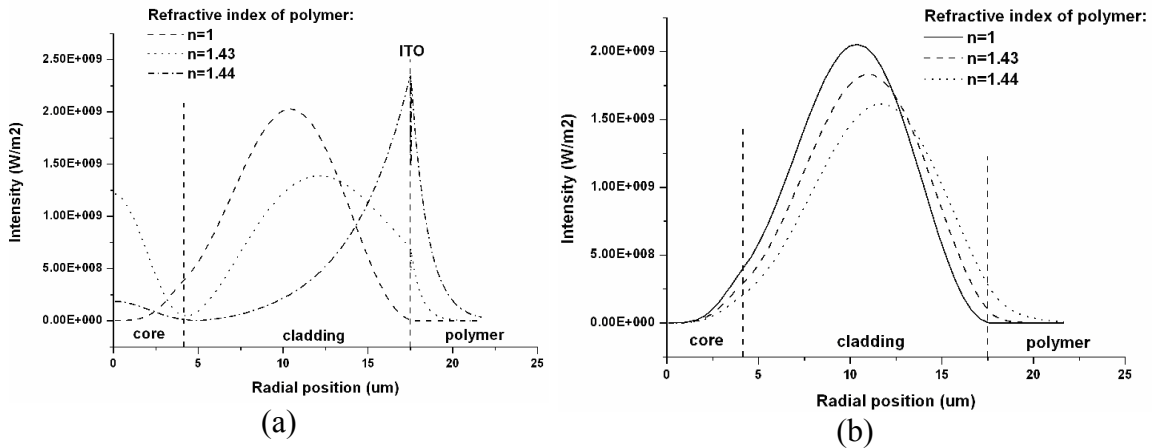


Figure 5.6: Transversal electric field distributions of the 2nd cladding mode (a) with ITO ($n = 1.80$ at 1550 nm) and (b) without ITO.

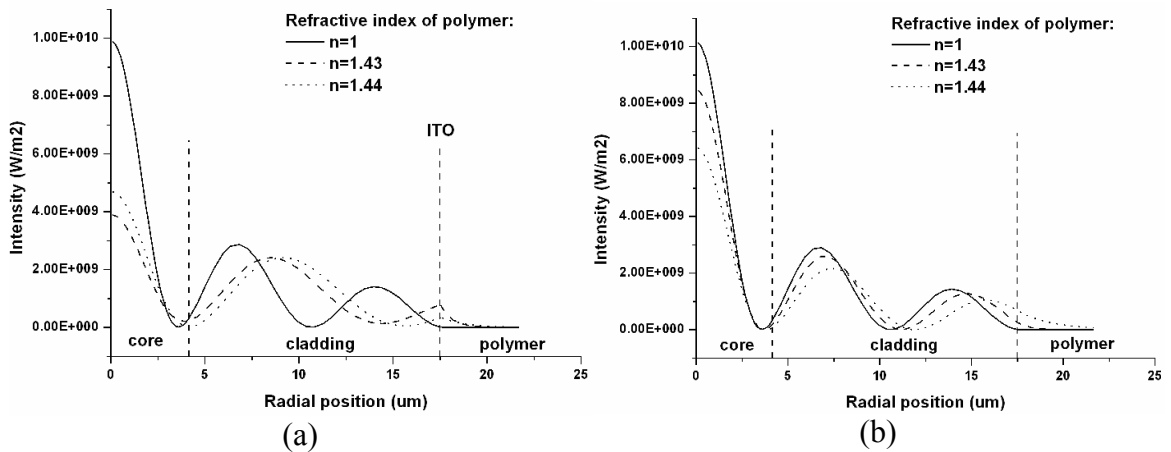


Figure 5.7: Transversal electric field distributions of the 3rd cladding mode (a) with ITO ($n = 1.80$ at 1550 nm) and (b) without ITO.

and the 1st and 3rd cladding modes will be stronger than the coupling between the core mode and the 2nd cladding mode. These results are consistent with those from the three-layer model, which showed that the major peak(s) in the output spectrum of an LPFG result from coupling to the odd cladding modes.

When the polymer index is close to that of the fiber cladding (1.43 and 1.44 in the figures), the mode field distributions in the ITO coated fiber deviate from those in the uncoated fiber. We find that the high refractive index of the ITO overlay forces more light energy to into the polymer layer. With a larger portion of the cladding mode fields affected by changes in the polymer, an enhanced tuning can be achieved. This tuning enhancement can be confirmed by comparing the effective cladding indices of a fiber with and without an ITO overlay. Since the resonant wavelength is proportional to the effective index of the cladding mode to which the core is coupling, the effective indices of a fiber with ITO should be more sensitive to changes in the polymer refractive index than an uncoated fiber.

Figures 5.8-5.10 show the effective indices of the cladding modes calculated by the four-layer model as a function of the polymer refractive index. In each of the figures, the effective indices of the ITO coated fiber rise more quickly than those of the uncoated fiber, quantifying the tuning enhancements that were predicted by the transversal mode field distributions. In each of the plots, the maximum range is set to 1.444, which is the material index of the fiber cladding, and once the effective index of a cladding mode exceeds 1.444, it is no longer guided and transitions to an overlay or radiation mode. In a fiber without an ITO overlay, all of the cladding modes transition to radiation modes almost simultaneously when the polymer refractive index reaches that of the cladding.

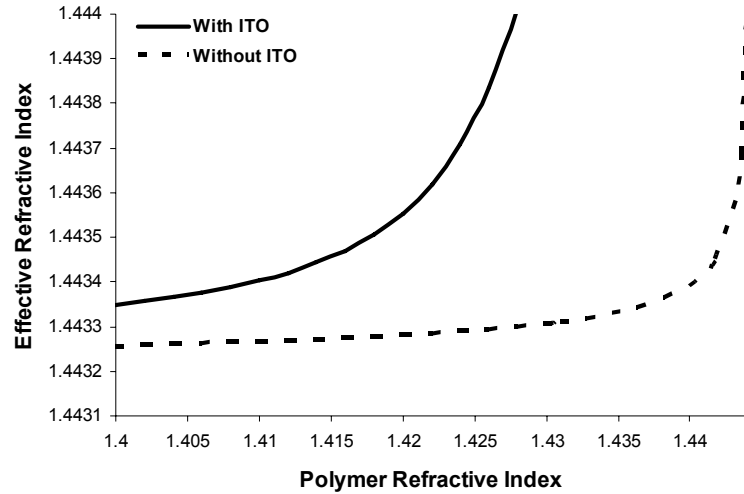


Figure 5.8: Effective refractive indices of the 1st cladding mode as a function of polymer refractive index in fibers with and without an ITO overlay. (ITO refractive index: 1.80; ITO thickness = 50 nm, Wavelength = 1550 nm)

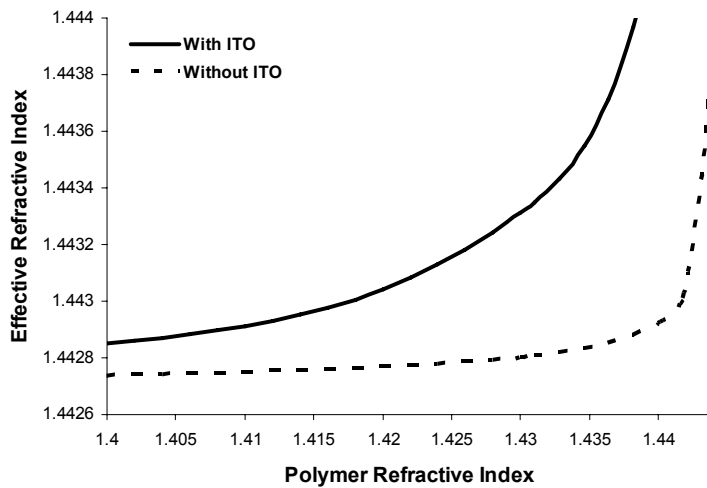


Figure 5.9: Effective refractive indices of the 2nd cladding mode as a function of polymer refractive index in fibers with and without an ITO overlay. (ITO refractive index: 1.80; ITO thickness = 50 nm, Wavelength = 1550 nm)

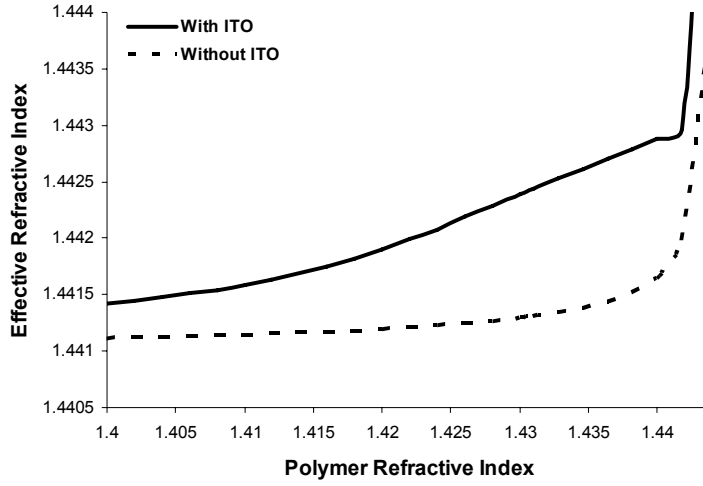


Figure 5.10: Effective refractive indices of the 3rd cladding mode as a function of polymer refractive index in fibers with and without an ITO overlay. (ITO refractive index: 1.80; ITO thickness = 50 nm, Wavelength = 1550 nm)

With ITO, however, the polymer index at which this transition occurs for each cladding mode is a function of the thickness and refractive index of the ITO [25-30]. In Figures 5.8 and 5.9, the 1st and 2nd cladding modes transition to overlay modes around 1.425 and 1.435, respectively, and leading up to the transition, the effective indices of these modes rise exponentially. The effective index of the 3rd cladding mode is slightly different than those of the lower order modes. Instead of rising exponentially prior to transition, the effective index of the 3rd cladding mode starts rising linearly around 1.410 and briefly plateaus around 1.440 before transitioning to the ITO. The effective index at which the 3rd cladding mode plateaus is very close to the effective index held by the 1st cladding mode at 1.400. This is consistent with Figure 5.2, which shows that higher order modes move in to replace those transitioning to the overlay. In Figure 5.2, the cladding mode transitioning to the overlay is replaced by the next higher order mode, meaning that we should see the 2nd cladding mode replace the 1st cladding mode, not the 3rd. In our model,

however, we did not use the LP or scalar approximations used in many of the references. Instead, our model treats the cladding modes as vectors and calculates all of the cladding modes. As a result, the LP_{0n} modes shown in Figure 5.2 correspond to the odd modes that are shown in Figures 5.5-5.10 [58].

The tuning enhancement caused by the high index ITO overlay does not come without a price. Generally speaking, the mode field energy that moves into the polymer layer is taken from the core region. In Figure 5.5, the mode field intensity of the 1st cladding mode nearly goes to zero when the polymer index is raised to 1.430 and 1.440. A similar drop in intensity is seen in Figure 5.8 for the 3rd cladding mode. However, in the case of the 3rd cladding mode, the intensity only drops an order of magnitude, and the intensity in the core at 1.44 is equal to, if not higher than, the intensity of the 1st cladding mode field in the core for ambient air. The intensity of the 2nd cladding mode field in the core is slightly different than the odd mode fields. In ambient air, the intensity is nearly zero, but it jumps up when the polymer index is increased to 1.430. When the polymer index is further increased to 1.440, the intensity falls back down.

Based on these results, we expect that the strong resonant peak in ambient air is a result of the core coupling with the 1st cladding mode. Even though the 3rd cladding mode field intensity in the core is higher than that of the 1st cladding mode in ambient air, the resonant peak resulting from coupling between the core mode and the 3rd cladding mode will fall outside of the 1000-1700 nm window. When the polymer index is increased to 1.430, the core mode will likely couple energy into both the 2nd and 3rd cladding modes, and at 1.440, it will couple primarily to the 3rd cladding mode.

While the transversal cladding mode distributions in the core region can help us predict the cladding modes to which the core mode will couple to at different polymer indices, it is important to note that these distributions exist in a ITO coated fiber whether or not a grating structure is present. Once a LPFG is fabricated in the fiber, the grating parameters, including its period, length, uniformity, and strength, will all play a role in the location and depth of the resonant peak (as was detailed in the derivation of the four-layer model) . In the next chapter, we will compare the results of the four-layer model to the measured tuning spectra from LPFGs that we fabricated in our lab. This comparison will not only help us determine the accuracy of the model, but it will also give us better insight into how some of the known errors in our fabrication processes affect the performance of a tunable LPFG.

Chapter 6

Experimental Results and Analysis

To experimentally test our model, we measured the tuning ranges of an LPFG before and after it had been coated with ITO. The LPFG had a 40 μm diameter, was 8 mm long (20 total periods), and had a 400 μm grating period. The thickness and refractive index of the ITO overlay were approximately 50 nm thick and 1.888 at 632 nm, respectively. Even though we had run similar experiments on LPFGs with and without ITO in the past (Figures 3.10 and 4.6, respectively), two different LPFGs were used in those experiments, and the spectra shown in Figure 4.6 may or may not accurately represent the LPFG that was used to generate Figure 3.10 had it been coated with ITO. Therefore, the data collected during those experiments was not sufficient to compare against the results of the four-layer model.

6.1 - LPFG Tuning Analysis

In this experiment, we used index matching oils to provide an ambient refractive index variation from 1.390 to 1.446. This particular range of indices was chosen for two reasons. First, the LPFG's intrinsic sensitivity to changes in the ambient index is highest in this region (as shown in Figures 3.11 and 3.12). Secondly, the four-layer model results shown in Figure 5.10 indicate that the largest improvement in tuning performance is

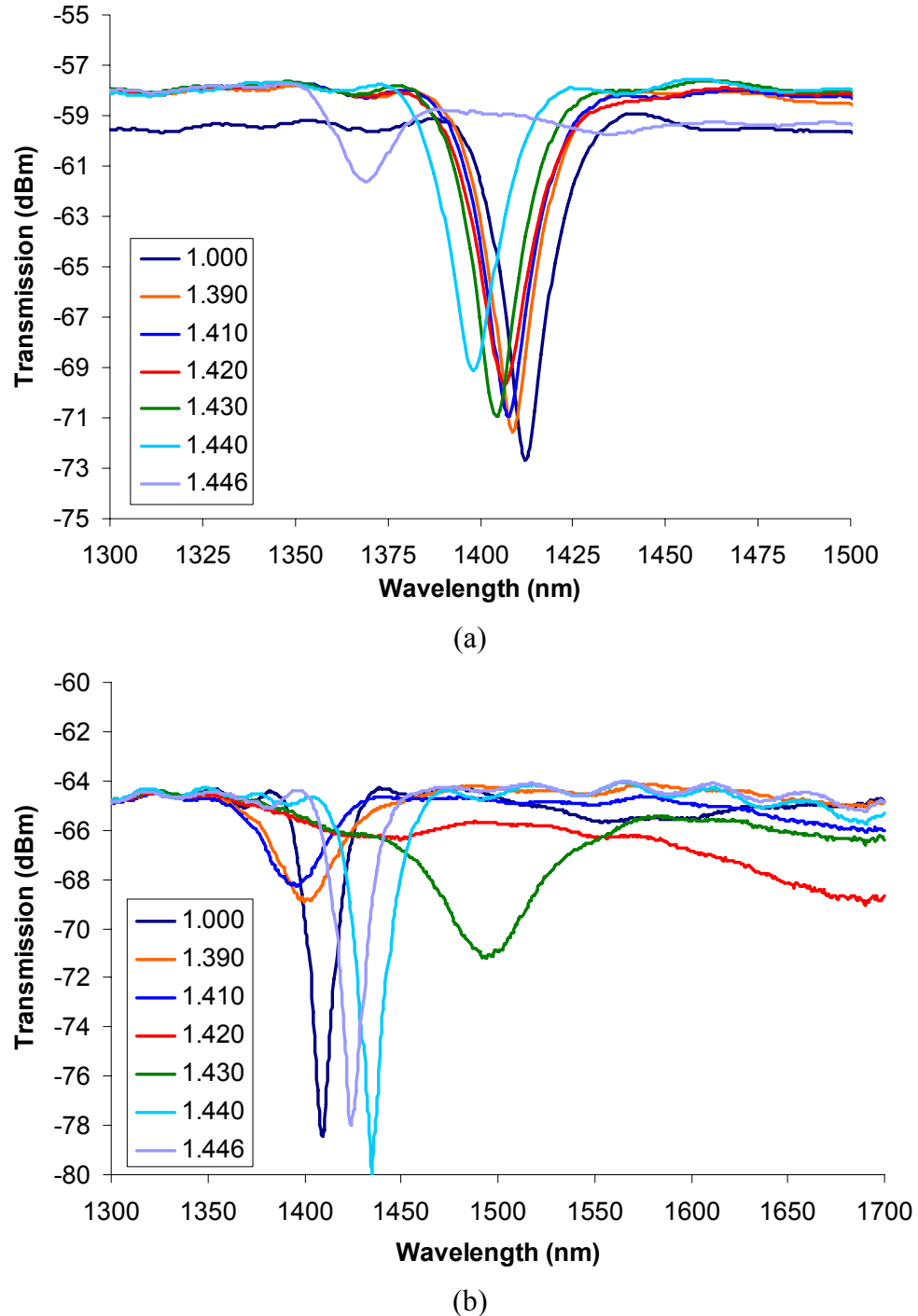


Figure 6.1: Experimentally measured spectra of an LPFG in several different ambient indices (a) before and (b) after being coated with a 50 nm ITO overlay. (Fiber diameter = 40 μm , Grating period = 400 μm , Grating length = 8 mm (20 periods))

achieved over these indices when the ITO overlay is added. The experimental data is presented in Figures 6.1-6.3. Figure 6.1 shows the tuning spectra recorded from the LPFG before and after adding the ITO overlay. The uncoated LPFG peak experienced non-uniform blue-shifts that totaled nearly 50 nm and became significantly shallower as the oil index was incrementally increased. After the ITO overlay was added, the peak blue-shifted non-uniformly about 10-12 nm and became significantly shallower as the oil index went from 1.390 to 1.410. At 1.420, however, mode transitions began to affect the spectrum. The original peak disappeared and a new peak began to take shape at a much longer wavelength. As the oil index continued to increase, the new peak became deeper and more defined. When the oil index reached 1.446, the peak looked nearly identical

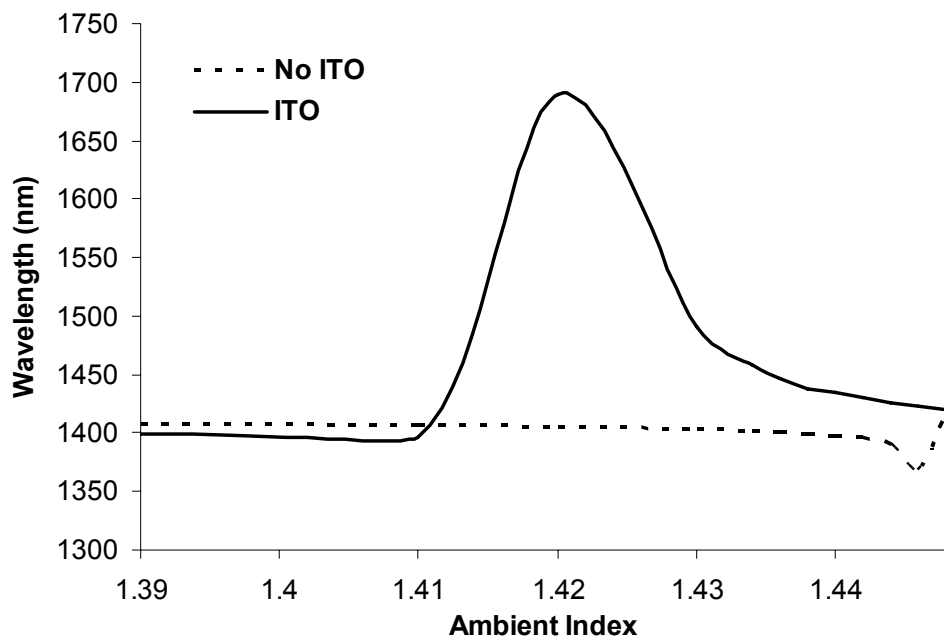


Figure 6.2: LPFG resonant wavelengths as a function of the ambient oil index with and without ITO.

to the original, but was positioned at a slightly longer wavelength. Over the 1.420 to 1.446 oil index range, the peak traveled nearly 250 nm. These spectra helped us identify and visualize the effect that mode transitions were having on our tunable filter, and the data taken from those spectra was used to generate Figure 6.2, in which the LPFG peak wavelengths are plotted as a function of the oil index. The data in this figure can be compared to the results from our model.

Since the data in Figure 6.2 cannot be directly compared to the calculated effective indices shown in Figure 5.10, we must first use the resonant wavelength equation, $\lambda = (n_{\text{eff}}^{\text{co}} - n_{\text{eff}}^{\text{cl-}i})\Lambda$, to convert the measured spectral data into effective indices, or conversely, convert the effective indices from the model into resonant wavelengths. However, before we choose either conversion, there are several important things to consider. First, the four-layer model incorporates several assumptions that were made to reduce the model's computational complexity. For the most part, we disregarded weaker coupling effects because their influence on the resonant coupling was deemed negligible. The measured spectral data, however, intrinsically includes all coupling effects, and if the weaker coupling effects neglected by the model had any significant effect on the LPFG spectra, there will be some discrepancies between the two data sets no matter which conversion is made. Secondly, we cannot explicitly determine the cladding mode to which the core mode is coupling from the measured spectral data. When no ITO is present and there are no mode transitions, we know that coupling occurs between the core mode and the 1st cladding mode, and thus, the data from the uncoated LPFG only needs to be compared to the calculated effective indices of the 1st cladding mode. When the

ITO overlay is present, however, the core mode initially couples with the 1st cladding mode, but it begins to couple with the 2nd and 3rd cladding modes once a certain ambient index threshold is eclipsed. This mode coupling transition is observed when the peak suddenly jumps to a much longer wavelength between the indices of 1.410 and 1.420. Immediately after the transition, the core mode will probably be coupling to both the 2nd and 3rd cladding modes (as discussed at the end of Chapter 5). As the ambient index increases toward the index of the cladding layer (~1.444), the core mode will gradually stop coupling to the 2nd cladding mode and will only couple to the 3rd cladding mode. The spectral data from the ITO coated LPFG must be grouped according to the cladding mode to which the core mode is coupling. The data from 1.390 to 1.410 should be compared to the calculated effective indices of the 1st cladding mode, while the data from 1.420 to 1.446 must be compared to the calculated effective indices of the 2nd and 3rd cladding modes. The final thing to consider before comparing the two data sets is the effect of experimental errors. The model makes calculations based on an ideal LPFG, meaning that the fiber and the ITO geometries are perfect and uniform. Accordingly, any peak wavelength calculations based on the model results would assume that the ITO coated LPFG was ideal. In reality, however, unavoidable errors that occur during the fabrication process, including, but not limited to, imperfect fiber geometries and diameters and non-uniform ITO coatings will undoubtedly have an effect on our tunable LPFG, but to what extent, we cannot be certain.

We will start our data analysis by looking at the data from the uncoated LPFG. This is the best place to start because the uncoated LPFG only involves coupling between the core mode and the 1st cladding mode, and the effects of an ITO layer do not have to

be considered. The effective index and coupling constant calculations for this scenario are relatively straightforward, and three-layer model would be sufficient to perform the analysis. However, we need to determine accuracy of the four-layer model for a basic LPFG before we consider the more complex ITO coated LPFG. By calibrating the model with the data from the uncoated LPFG, the model results for the ITO coated LPFG will hopefully be better fit to our measured data, and since the model will represent the ideal case, the remaining differences between the two data sets will help us isolate and identify the effects of experimental errors in the measured spectral data.

In Figure 6.3, the effective indices of the 1st cladding mode calculated by the four-

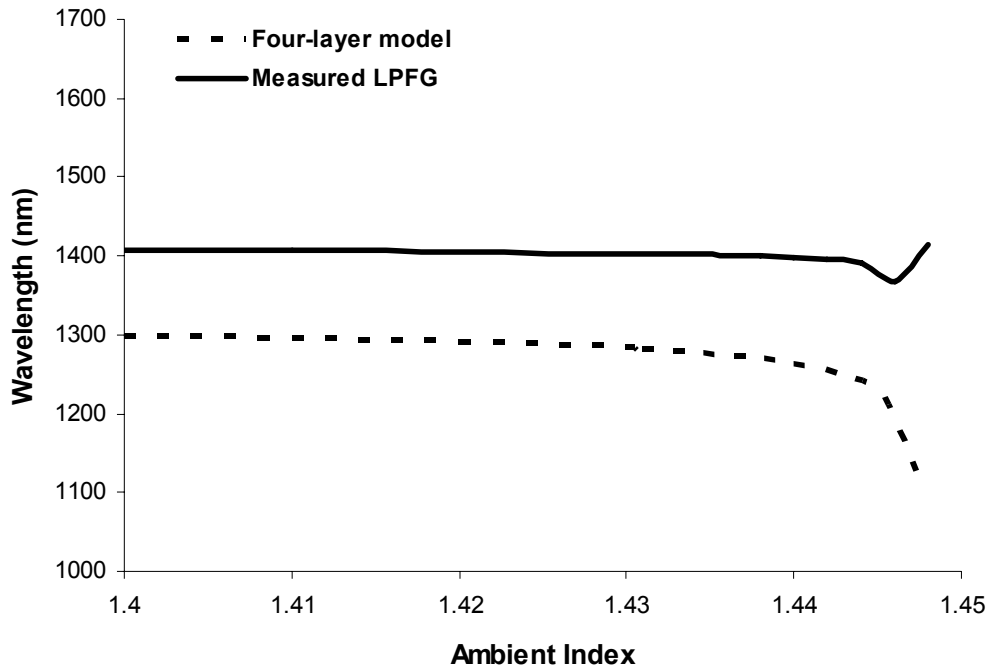


Figure 6.3: The calculated effective indices of the 1st cladding mode are converted into resonant wavelengths and compared to the measured spectral data. (No ITO; Effective core index (n_{eff}^{co}) \sim 1.4465, Grating Period (Λ) = 400 μ m)

layer model have been converted to resonant wavelengths and plotted with the measured spectral data from the uncoated LPFG. The effective cladding index used to make the conversion was approximately 1.4465. This value was calculated at 1550 nm using the diameter of the fiber core and the material indices of the core and the cladding. Two discrepancies between the calculated and measured data are immediately apparent: (1) the measured resonant wavelengths are over 100 nm longer than those calculated from the model's effective indices; and (2) the calculated wavelengths predict a much sharper blue-shift than was measured as the ambient index approaches that of the fiber cladding. The latter of these discrepancies is most likely a result of a limitation in our model's accuracy to predict the exact resonant wavelength at ambient indices equal to or above the cladding index. As mentioned in the previous chapter, the cladding modes of a fiber without ITO become radiation modes, which are essentially unguided leaky cladding modes, once the ambient index meets or exceeds that of the cladding. The model only calculates the effective indices of guided cladding modes. When the ambient index reaches that of the cladding, the model accuracy predicts that the mode is no longer guided, but the results that it produces for ambient indices higher than the cladding are not necessarily valid. This same inaccuracy will also appear when we examine cladding modes that transition to the overlay in an ITO coated fiber. Furthermore, the calculated resonant wavelengths are estimates that only consider coupling between the core mode and a single discrete cladding mode. They do not include the effects of the core mode coupling to multiple cladding modes simultaneously. They also do not take into account phenomena that begin to occur when the ambient index exceeds that of the cladding. For example, ambient indices that are higher than the cladding have been shown to cause

Fresnel reflections at the cladding/ambient interface [59]. These reflections can enable low-loss propagation in the cladding in the absence of a true guided mode and contribute to red-shift in the measured resonant wavelength around 1.445.

While the limitations of the model are the likely cause of discrepancies that occur at ambient indices near transitions or close to the cladding, they are not responsible for the large gap between the measured and predicted resonant wavelengths. Based on our knowledge of LPFGs and the formulation of the four-layer model, we were able to identify two potential sources of this error: (1) The resonant wavelengths in Figure 6.3 were calculated using $\lambda = (n_{eff}^{co} - n_{eff}^{cl-i})\Lambda$, which is a simplified version of the phase matching condition that does not take the grating strength into consideration; and (2) experimental errors, such as variations in the fiber thickness and non-uniform UV exposure, caused the measured resonant wavelength to differ from the model prediction. Each of these factors probably contributes to the error, but since we cannot undo the errors in the measured data and are trying to find the model that best predicts our LPFGs' behavior, we take a more detailed look at the first of the two factors listed above.

The resonant wavelengths in Figure 6.3 were calculated using $\lambda = (n_{eff}^{co} - n_{eff}^{cl-i})\Lambda$. With this formula, the only grating parameter that influences the resonant wavelength is the period, and the self-coupling constants are not taken into consideration. The complete phase matching condition for an LPFG is given by $\frac{2\pi}{\lambda}(n_{eff}^{co-i} - n_{eff}^{cl-i}) + s_o(\tau_{l,l} - \tau_{i,i}) = \frac{2\pi}{\Lambda}$ (Eq. 5.1). By solving this equation for the resonant wavelength, neglecting cladding/cladding coupling, and setting $s_0 = 1$, we arrive at:

$$\lambda = \frac{(n_{eff}^{co-i} - n_{eff}^{cl-i})}{I - \tau_{l,l} \frac{\Lambda}{2\pi}} \Lambda, \quad \text{Eq. 6.1}$$

which shows that the resonant wavelength is not only a function of the difference between the core and cladding effective indices and the grating period, but also of the first Fourier component of the grating (s_0) and the difference between the self-coupling constants of the core and cladding modes, $\tau_{l,l}$ and $\tau_{i,i}$, respectively. (Equation 6.1 is identical to the resonant wavelength equation that was derived from the four-layer model (Eq. 5.29)). More importantly, the self-coupling constants are proportional to the grating strength, or the magnitude of the photoinduced index change in the fiber core. Using this equation and the calculated refractive indices, the predicted resonant wavelengths should be much closer our measured values.

The self-coupling coefficients of the core and cladding modes were calculated by the four-layer model using a grating strength (σ) of 7.5×10^{-4} , and the first Fourier component was set to unity, which represents a sinusoidal grating. We did not have a means to accurately calculate the real photoinduced refractive index change, but we were able to find a reference that detailed the index change that could be induced in the Fibercore PS1500 fibers that we used for our gratings [60]. In the reference, 7.5×10^{-4} was the saturated photoinduced index change achieved using a high average power (up to 1 W), high repetition rate (6 kHz) low pulse energy (< 2 mJ) 255 nm source. We used a continuous wave (CW) UV laser with a 244nm wavelength and ~ 100 mW average power to fabricate our gratings. However, our exposure time was significantly higher

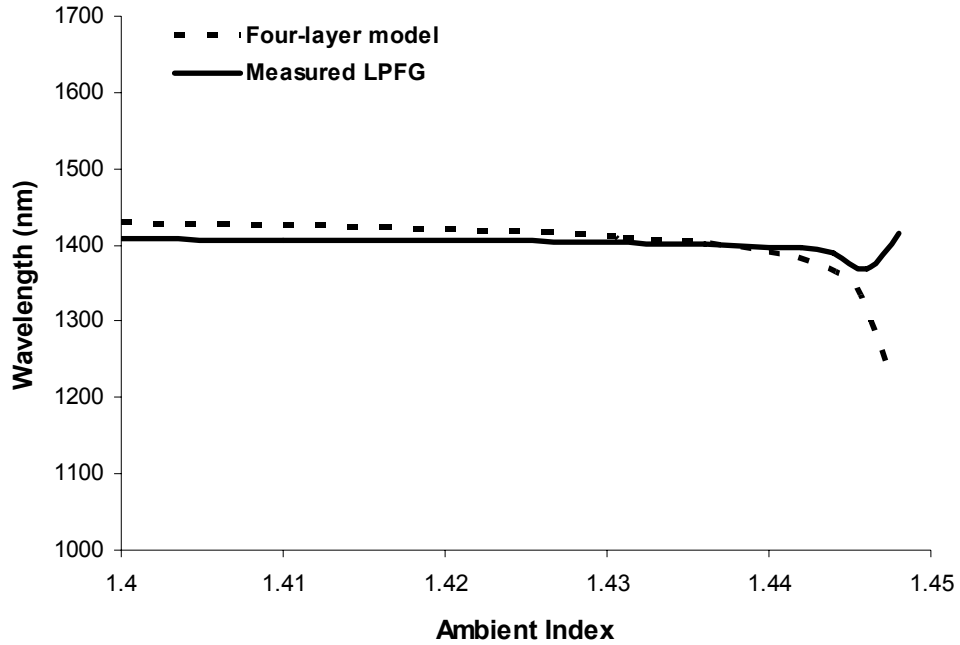


Figure 6.4: The calculated effective indices of the 1st cladding mode are converted into resonant wavelengths using the full phase matching condition and compared to the measured spectral data. (No ITO; Effective core index (n_{eff}^{co}) ~ 1.4465 , Grating Period (Λ) = 400 μm , Grating Strength (σ) = 7.5×10^{-4})

than the 100 s that was needed to reach index saturation in the reference. Therefore, we decided to use the saturation index in our model calculations. Figure 6.4 shows the resonant wavelengths that are calculated using the self-coupling constants and the full phase matching condition. The gap between the measured and predicted resonant wavelength was virtually eliminated. Aside from showing a slightly larger tuning range than what we measured, a difference that could easily be contributed to our fabrication errors, the model data fit our experimental data relatively well.

Once we had found the best fit model for the LPFG without ITO, we used the four-layer model and the full phase matching condition to predict the resonant

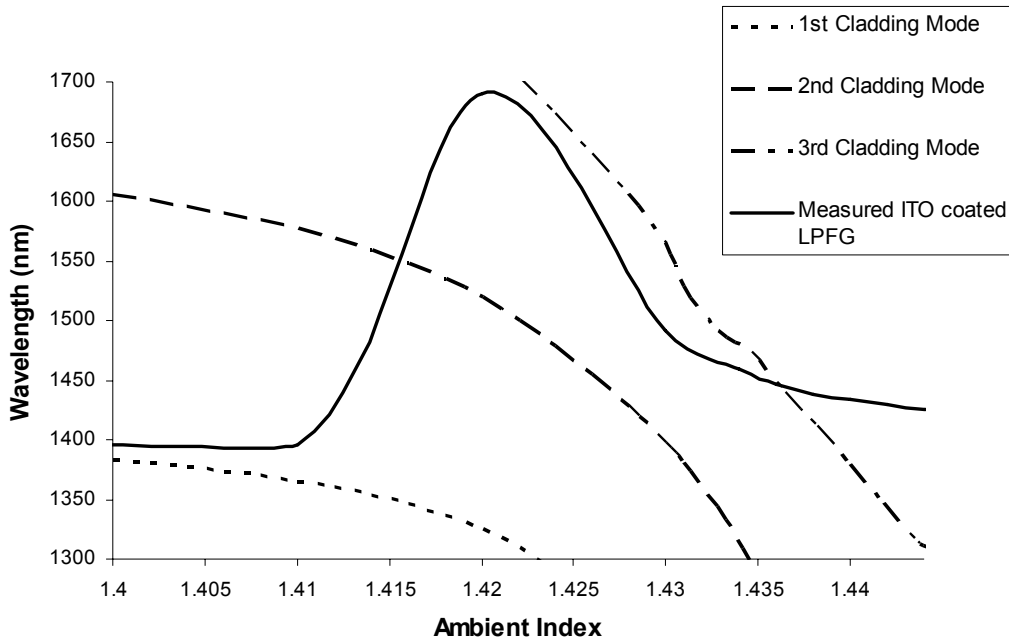


Figure 6.5: ITO coated LPFG wavelengths as a function of the ambient index compared to the resonant wavelengths calculated from the model effective cladding indices. (Effective core index (n_{eff}^{co}) ~ 1.4465 , Grating Period (A) = $400\mu\text{m}$, Grating Strength (σ) = 7.5×10^{-4} , ITO thickness = 50 nm , ITO refractive index ~ 1.80)

wavelengths and tuning behavior of an ITO coated LPFG. Unlike the uncoated LPFG case, we had to calculate the effective indices and self-coupling constants of the first three cladding modes. The grating strength was kept at 7.5×10^{-4} , and the ITO thickness and refractive index were set at 50 nm and 1.80 , respectively. Figure 6.5 shows the resonant wavelengths calculated from the first three cladding modes compared to the measured spectral data from our ITO coated LPFG. In the figure, the resonant wavelengths predicted by the model are very close to those that we measured. We can easily see that the core mode initially couples to the 1st cladding mode, and then after the transition around 1.420, it begins to couple to the 3rd cladding mode. Contrary to what we had predicted in Chapter 5, these results seem to imply that the 2nd cladding mode has

a limited effect on the resonant wavelength after the 1st cladding mode has transitioned to the cladding. Although the wavelengths do not match perfectly, the slope and shape of our measured curve coincide with that of the 3rd cladding mode curve after the transition, which means that the model is accurately predicting the resonant peak's sensitivity to changes in the ambient index. However, we still see the discrepancy between the predicted and measured wavelengths at indices close to that of the cladding (~1.44). In the case of an ITO coated LPFG, the optical phenomena responsible for keeping the resonant wavelength from further blue-shifting become even more complex than in the uncoated LPFG case because we have to consider Fresnel reflections at multiple interfaces (cladding/ITO and ITO/ambient) and modes that are guided, or partially guided, by the thin ITO layer [59].

Even though the model fits our measured data well, we cannot draw any substantial conclusions based on the data from a single sample. In order to sufficiently test the model, we needed to record the tuning behavior of more samples and compare the data to the model results. If the new samples are kept as uniform as possible through the fabrication processes, this comparison will serve a dual purpose. It will allow us to see how the spectra from a “uniform” group of samples are affected by experimental errors, and we can adjust parameters in our model to see how well we can account for the errors.

Six new LPFGs were fabricated and coated with ITO for our next round of index oil experiments. To make the samples as uniform as possible, we batch processed the fibers during etching and ITO sputtering. (Incidentally, we used six fibers because that is the maximum number that would fit into our fiber etching caddy.) If we assume that the fiber diameters and the ITO properties were the same for all six fibers, fabrication errors

will likely result from non-uniform UV exposure during grating writing and non-uniform ITO films.

Grating writing is inherently a single element process that does not lend itself to batch processing. Each fiber is manually placed in a single fiber caddy, which is then placed into the writing setup (Figure 6.6). A CW UV laser is focused through an amplitude mask of specified period to the core of the etched fiber. The optics that guide and focus the UV beam are mounted on a computer driven, nano-precision Aerotech ABL-1000 air bearing stage, which scans the beam back and forth across a specified length of the fiber. Even though the UV beam can be precisely aligned with the stage,

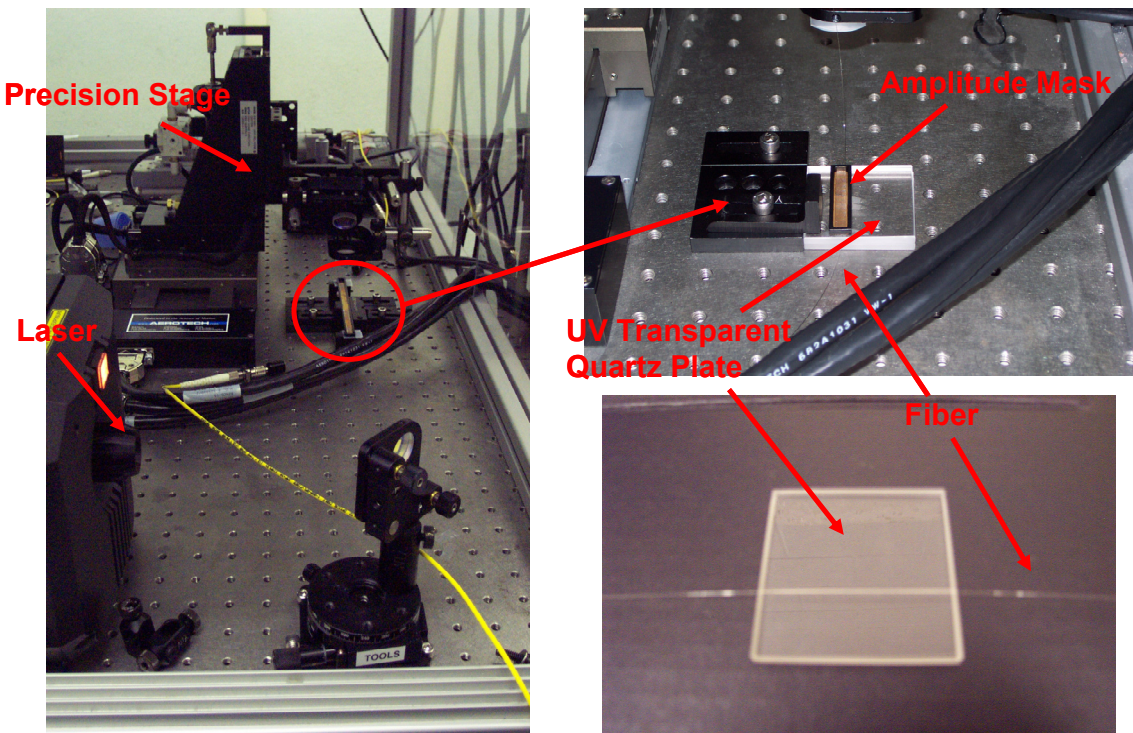


Figure 6.6: Several pictures of the grating writing setup.

the major source of error in the writing process comes from the manual alignment of the fiber in the caddy. The groove that has been cut into the caddy to hold the fiber is slightly larger than the fiber diameter, and the fiber's position within the groove varies from run to run. Thus, the characteristics of each grating are unique due the non-uniform UV exposure that occurs because of error in the alignment.

As discussed in Chapter 5, the configuration of our sputtering system will also contribute to fabrication error because we have to coat our fibers one side at a time. Since the fibers are cylindrical, the ITO layer will be thicker on the areas of the fiber surface closest to the ITO target. Additionally, the film thickness on batch processed fibers may vary slightly with their position relative to the ITO target. Since sputtering is primarily a line-of-sight process, the surface on which the film is being deposited should be parallel to and directly across from the target to achieve the best thickness uniformity. However, the thickness uniformity is not perfect, especially on surfaces across from the edges of the target. All of the batch processed fibers could not be placed directly across from the center of the ITO target, and some overlay thickness variations within a group of batch processed fibers are inevitable, particularly among those that are farther from the center of the ITO target.

Figure 6.7 shows the tuning spectra from the six new LPFGs. Each sample had a measured cladding diameter of 40 μm and a 50 nm ITO overlay with a 1.888 refractive index at 632 nm. The LPFGs were all 8 mm in length and had a grating period of 400 μm . Each ambient index at which spectra were measured was assigned a color, and the same color scheme was used in all six plots of Figure 6.7 to highlight any differences in

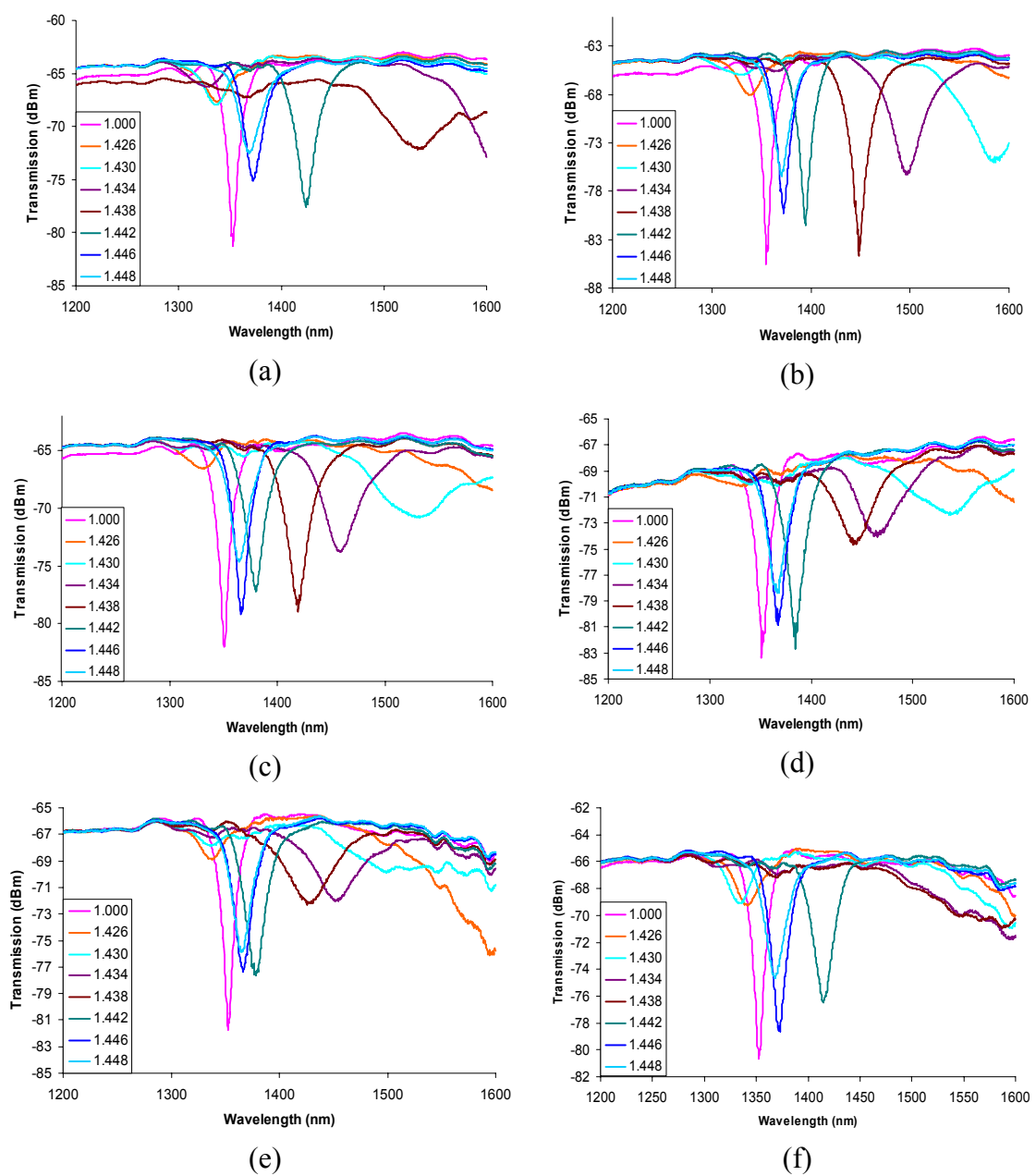


Figure 6.7: Tuning spectra taken from six, batch processed ITO coated LPFGs.

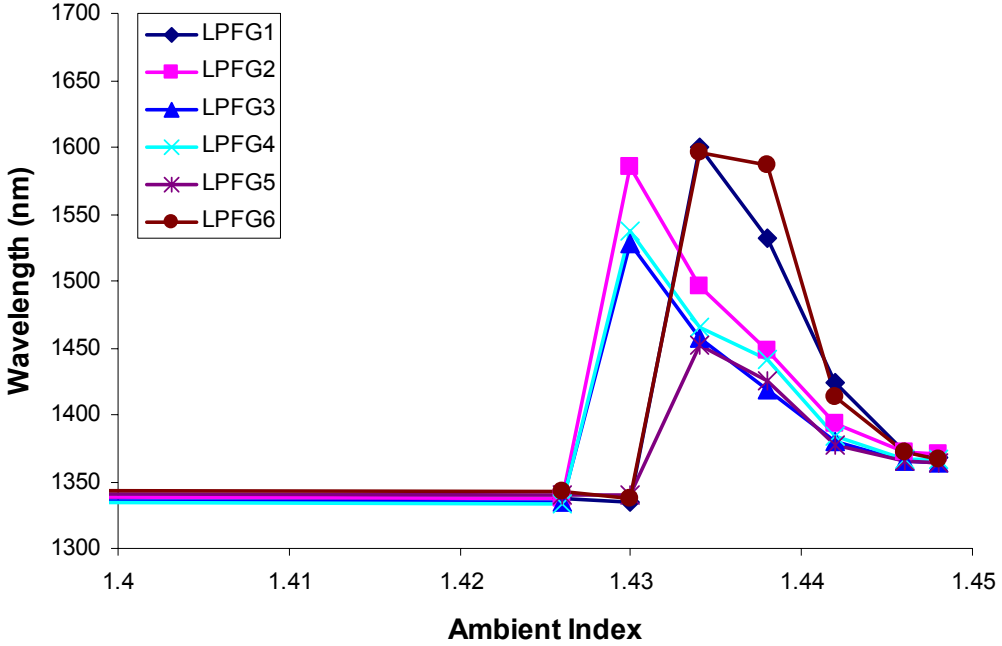


Figure 6.8: The measured resonant wavelengths from the six batch processed, ITO coated LPFG samples as a function of the ambient oil index.

the tuning performances of the samples. Upon examining the plots, the peaks of the six samples in ambient air (i.e the pink curves) are nearly identical in both position and in depth, measuring roughly 1352 nm and -16 dBm, respectively. Since the LPFGs and ITO overlays all had the same parameters, this is what we would expect, but the exposure times needed to achieve a resonant peak around this wavelength varied slightly, which meant that the grating strengths were not uniform (i.e. the fiber was misaligned during fabrication) and/or that there was some small thickness variations in the fibers. When the samples were tuned with index oils, no two samples generated the same tuning spectra. At any given oil index, the peaks of the samples were at different wavelengths and had different depths. In some cases, as in plots (c) and (d), evidence of the cladding mode transition was seen at 1.426. Other samples, such as (a) and (f), did not transition until

the oil index was in excess of 1.434. When the measured resonant wavelengths from the six LPFGs were plotted as a function of the ambient index (Figure 6.8), however, we saw that the tuning behavior of the six samples was more similar than it had appeared when we were only looking at the individual spectra. The shapes of the resonant wavelength curves were similar, and the indices at which the transitions take place only differed over an approximate 0.005 index range. The magnitude of the tuning ranges, on the other, varied more significantly. The results from these batch processed samples clearly illustrated that non-uniform errors introduced during the fabrication processes significantly affect an LPFG's tuning characteristics.

Before the new measured data is compared to the model data, we must mention that the resonant wavelength curves in Figure 6.8 must be kept in perspective. The curves shown in Figure 6.8 were adapted from the measured spectra in Figure 6.7, but in some cases, the location of the resonant peak was not clear cut. In Figure 6.7(b), for example, there is a very distinct peak present for each of the ambient indices, and at 1.430, we can actually see two peaks at two different wavelengths because the core is coupling to both the 1st and 3rd modes. In this case, we considered the larger of the two peaks, the peak corresponding to the core mode coupling with the 3rd cladding mode, as the resonant wavelength for the 1.430 ambient index. In Figure 6.7(f), on the other hand, there is not a very distinct peak at the either 1.434 or 1.438 ambient indices, but one could argue that the dip in the spectra around 1600 nm is the new peak taking form. In Figure 6.8, we used that dip as the "resonant wavelength" for LPFG6 at 1.434 and 1.438, and since the spectrum showed very little change over those two indices, the resonant wavelength curve for that sample is much broader than the others. While these

interpretations of the real data should not significantly affect our analysis, they are a contributing source of error that may cause some of the resonant wavelength curves in Figure 6.8 to deviate slightly from the model.

In Figure 6.9, the model calculated resonant wavelengths are individually compared to each of the six LPFG resonant wavelength curves. The parameters used in the model were the same as those used in the previous comparison, namely grating strength (σ) = 7.5×10^{-4} , ITO thickness = 50 nm, and ITO refractive index = 1.80. For the most part, the shapes and slopes of the measured resonant wavelength curves fit the model, with the core mode coupling to the 1st cladding and 3rd cladding modes before and after the transition, respectively. However, in all of the plots, the resonant wavelengths predicted by the model when the core mode is coupling to the 1st cladding mode are significantly longer than what was measured. Assuming that small differences in the fiber diameters and ITO coatings were not responsible for such a large discrepancy, we decided to vary the grating strength in the model to see if we could achieve a better fit. The results are shown in Figure 6.10.

In Figure 6.10, the measured resonant wavelengths from the six batch processed LPFGs are again compared to resonant wavelengths calculated from the model data. This time, however, the grating strength (σ) in the model data has been reduced to 4.9×10^{-4} . With this reduction, the model is much better fit to the measured data. In all of the plots, the large discrepancy that existed between the measured and calculated wavelengths at an ambient index of 1.40 has been eliminated or greatly reduced, and in some cases, the measured and calculated wavelengths are in better agreement following the transition as well.

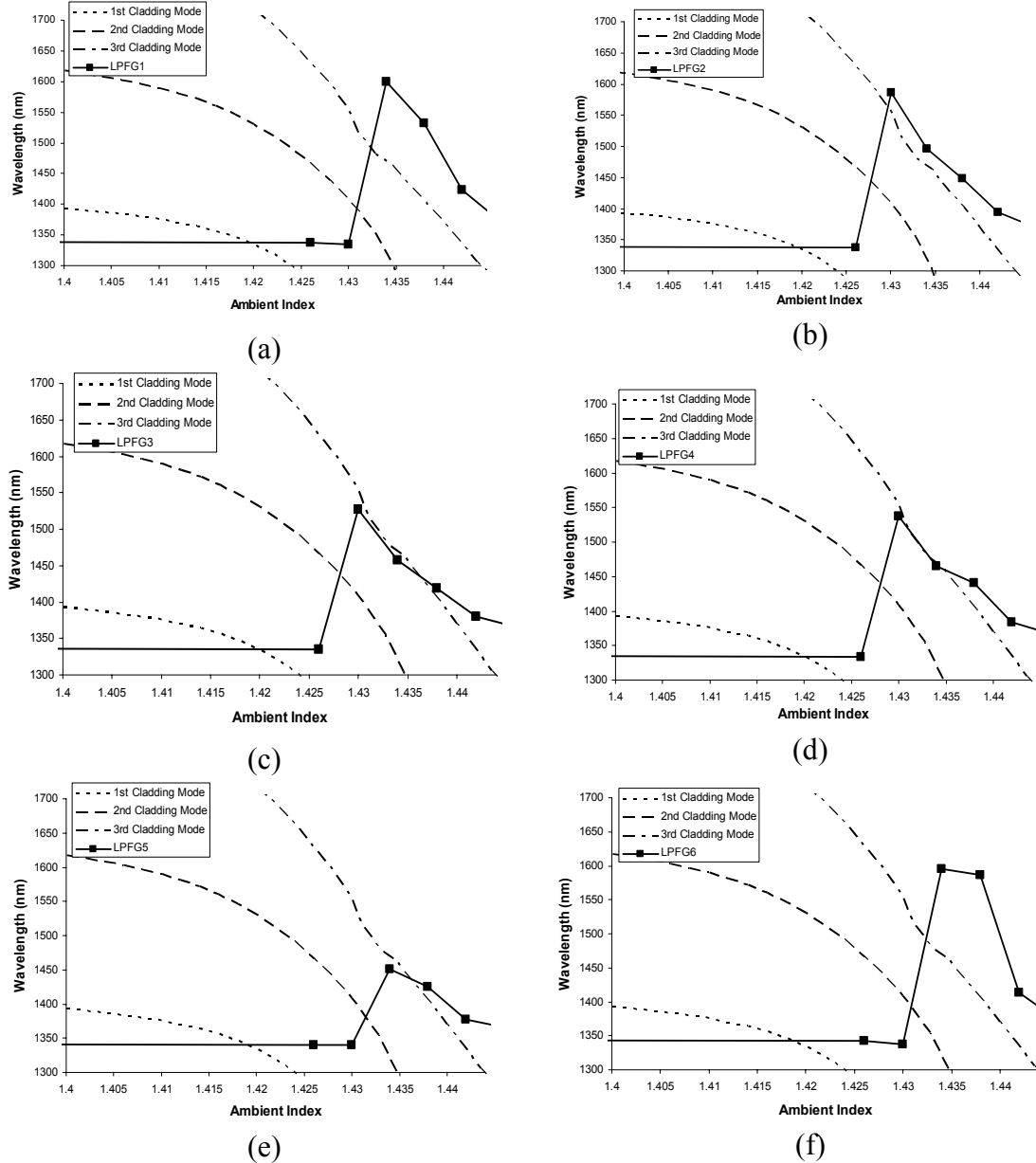


Figure 6.9: Resonant wavelengths from the six batch processed, ITO coated LPFGs as a function of the ambient index compared to the resonant wavelengths calculated from the model effective cladding indices. (Effective core index (n_{eff}^{co}) ~ 1.4465 , Grating Period (Λ) = $400\mu\text{m}$, Grating Strength (σ) = 7.5×10^{-4} , ITO thickness = 50 nm, ITO refractive index ~ 1.80)

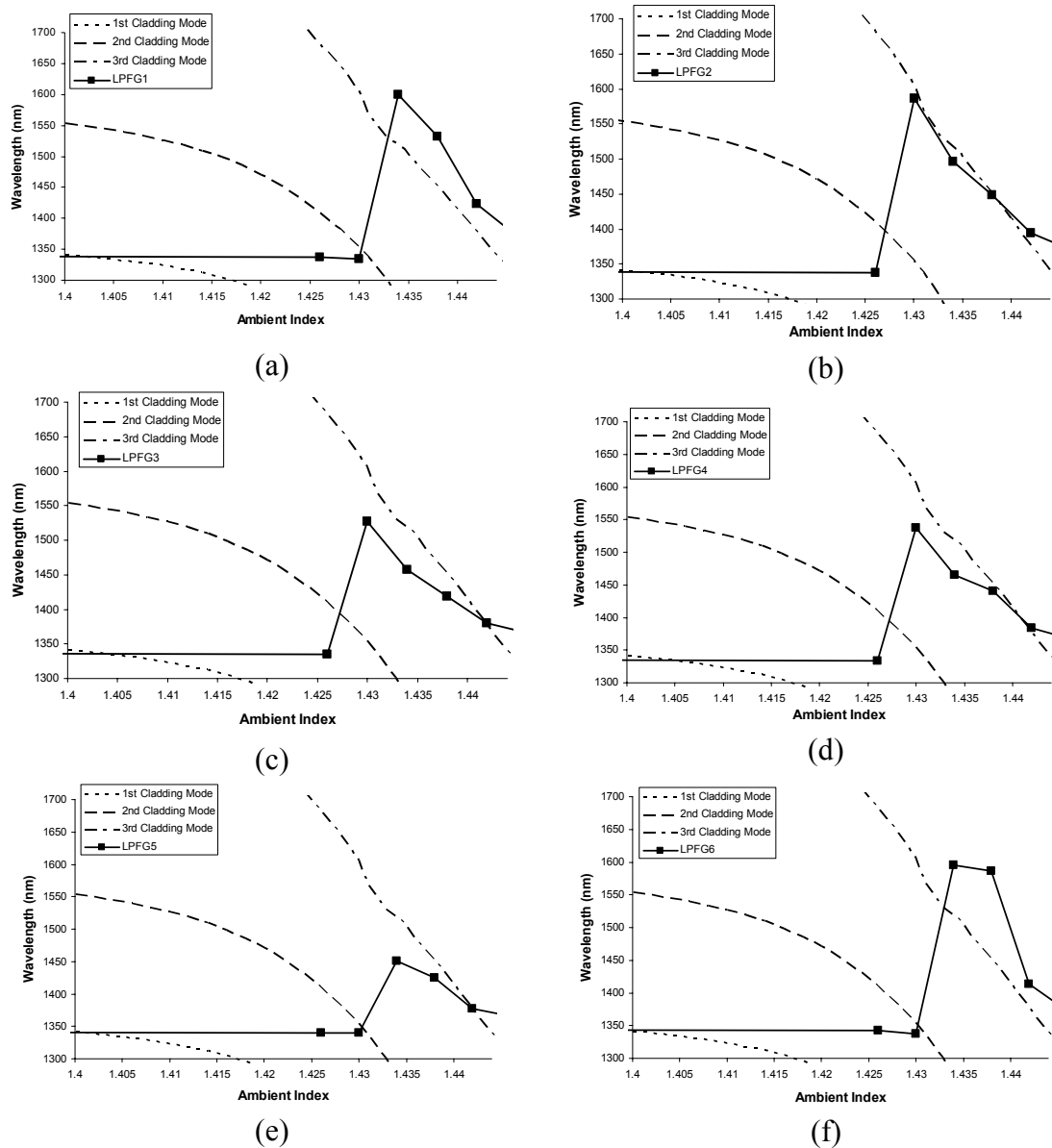


Figure 6.10: Resonant wavelengths from the six batch processed, ITO coated LPFGs as a function of the ambient index compared to the resonant wavelengths calculated from the model effective cladding indices. (Effective core index (n_{eff}^{co}) ~ 1.4465 , Grating Period (Λ) = $400\mu\text{m}$, Grating Strength (σ) = 4.9×10^{-4} , ITO thickness = 50 nm, ITO refractive index ~ 1.80)

As expected, a grating strength of 4.9×10^{-4} causes the model to fit some of the samples better than others, and we could further adjust the grating strength to optimize the model results for each of the six LPFGs. More importantly, the results in Figure 6.10 verify our claim that the grating writing process is a primary source of non-uniform error. Since grating strength is a function of the amount and uniformity of UV exposure and each LPFG was written individually, we were able to adapt our model to the measured results from each sample by simply adjusting the grating strength. Additional variations between the measured data and the model likely result from the geometries and properties of the ITO overlay being less than ideal.

6.2 - Peak Depth Analysis

Thus far in the analysis of our experimental data, we have focused solely on the tuning characteristics of our ITO coated LPFGs. We compared the measured resonant wavelength curves to those from the model and showed that the model was fairly accurate in predicting the tunability of the resonant peak after the mode transition. We also substantiated that some of the differences between our measured and model data sets were a result of errors from the grating writing process. In real world applications, however, the depth of the LPFGs resonant peak is just as important as the range over which the device can be tuned. In Chapter 5, Equation 5.29 showed that the grating length, L , and the coupling constants, κ , are most responsible for the depth of the resonant peak. The product of the grating length and the coupling coefficient is used as an argument to a cosine squared term, which dictates a grating's transmission, or depth, at a

specific wavelength. Using our four-layer model, we can calculate the coupling constants of the cladding modes and compare the results to the peak data that was collected from the sample LPFGs. By looking at both the tuning data and the peak data, we will better determine the accuracy of our model.

Figure 6.11 shows the coupling constants of the first three cladding modes as a function of the ambient index. The top plot shows the coupling constants over the 1.000 to 1.445 ambient index range while the bottom plot is an exploded view of the 1.400 to 1.445 ambient index range. The coupling constants were generated by the four-layer model for a 40 μm diameter fiber with a 50 nm, 1.80 index ITO overlay. In order to interpret the model data presented in Figure 6.11, we turn to Equation 5.33, $T = \cos^2(\kappa L)$. (To simplify our analysis, we will only focus on the on-resonance transmission equation instead of the full condition given by Equation 5.27.) According to this equation, the transmission at the resonant wavelength, or peak depth, is a sinusoidal function. Peak depth is maximized when $\kappa L = m \frac{\pi}{2}, m = 1, 3, 5, \dots$ and will vary as the coupling constant since the grating length is fixed. When the LPFG is in ambient air ($n = 1.000$), the core mode couples to the 1st cladding mode, and the measured peak is at or near its maximum depth. Since the sample gratings were all 8 mm in length (L), we would expect the coupling constant (κ) of the 1st cladding mode to be near 196 m^{-1} . In Figure 6.7, the coupling constant of the 1st cladding mode is approximately 184 m^{-1} when the ambient index is 1.000, which is very near the value we expected. The coupling constant of the 1st cladding mode remains fairly constant as the ambient index is increased from 1.000 to 1.400. At 1.400, however, it begins to fall off while the

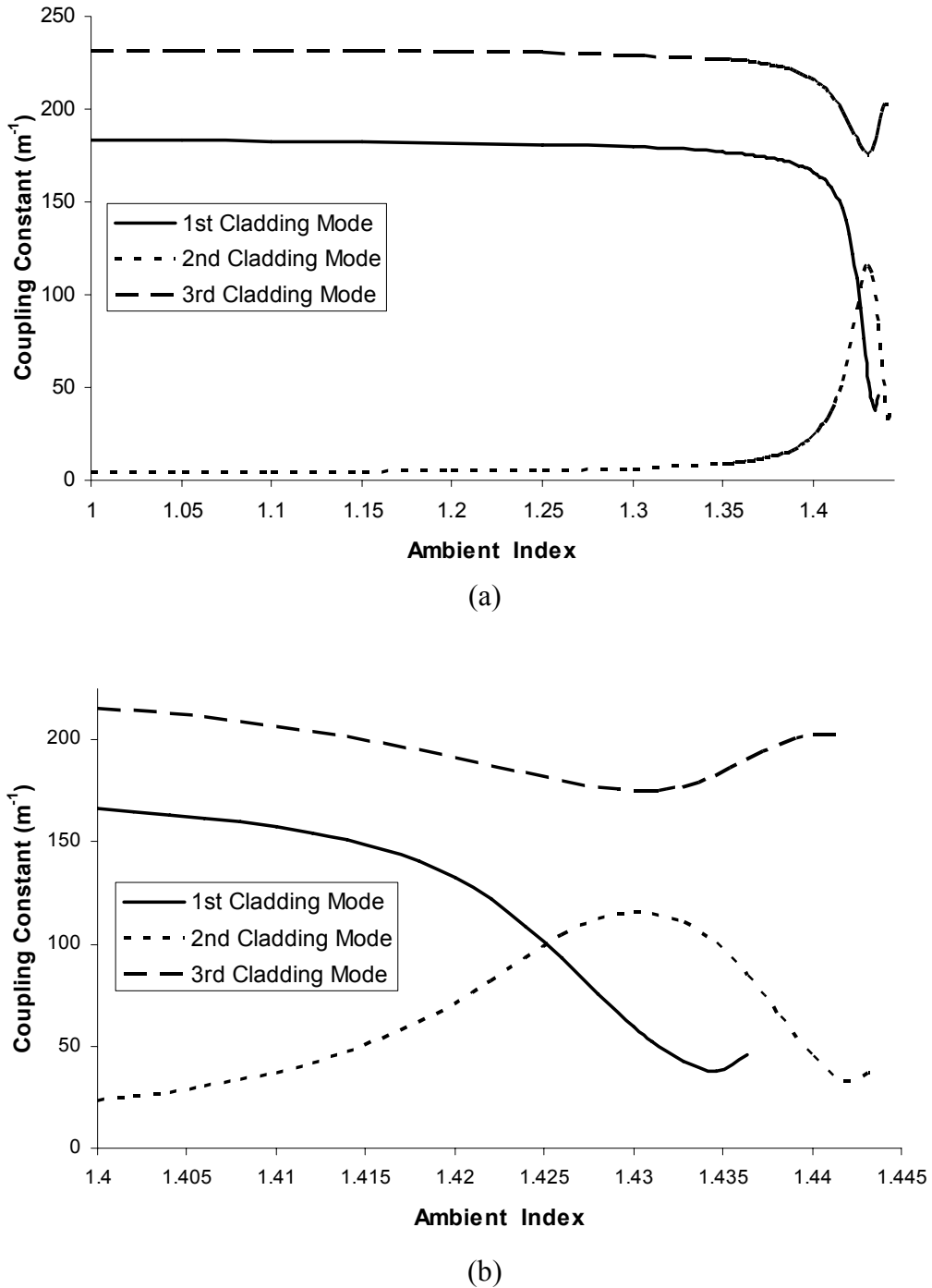
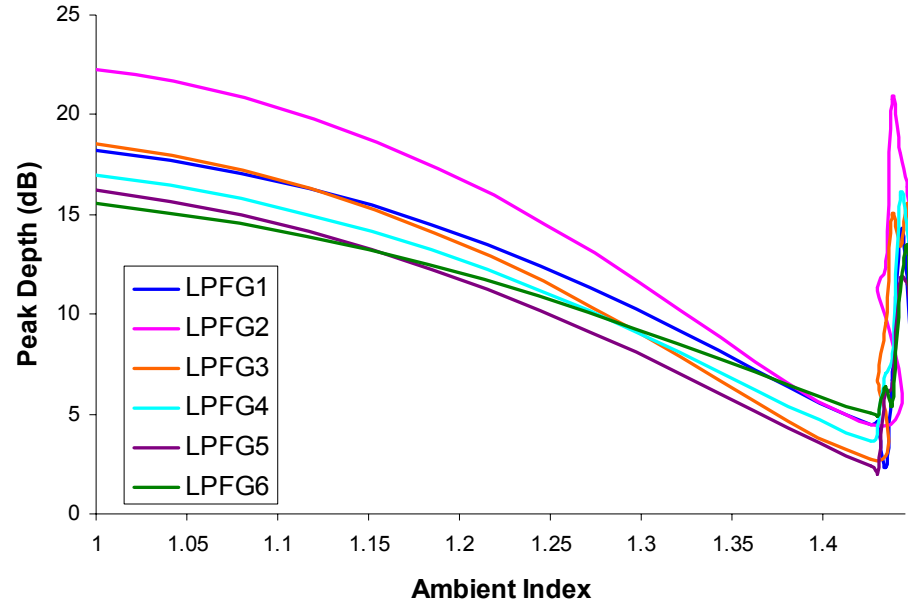


Figure 6.11: The calculated coupling constants (κ) of the first three cladding modes as a function of the ambient index. In the top plot (a), the ambient index range is 1.000-1.445. The bottom plot (b) is an exploded view of the 1.400-1.445 ambient index range. (ITO thickness = 50 nm, ITO refractive index ~ 1.80)

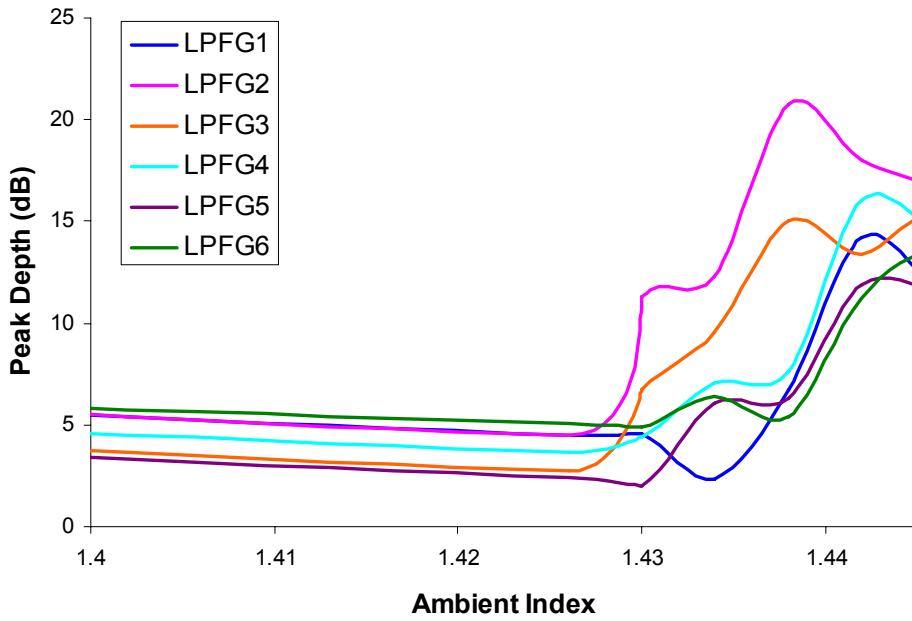
coupling constant of the 2nd cladding mode begins to increase. Concurrently, the coupling constant of the 3rd cladding mode decreases slightly. Around 1.430, the coupling constant of the 2nd cladding mode is maximized, and the coupling constant of the 3rd cladding mode is minimized. Above 1.430, the coupling constant of the 2nd cladding mode falls toward zero while the coupling constant of the 3rd cladding mode increases slightly. If we were to anticipate the LPFG peak depth solely on the coupling constant data in Figure 6.10, we would expect a strong peak in air, followed by a decrease in peak depth as the ambient index is increased from 1.400 to 1.420. Between 1.420 and 1.430, the core mode would begin coupling to the 2nd and/or 3rd cladding modes as the 1st cladding mode moves to the overlay. The peak depth following the transition will depend on the ambient index at which the transition occurs and the cladding mode to which the core mode is coupling. For example, if the core mode began to couple only to the 3rd cladding mode as the 1st cladding mode transitioned to the overlay, we would expect a deep peak because the value of the 3rd cladding mode's coupling constant is near the 196 m^{-1} value that maximizes peak depth. On the other hand, if the core mode coupled energy into the 2nd cladding mode following the transition, we would expect to see a shallow peak or no peak at all since the coupling constant is well below the value which yields maximum peak depth. In this second scenario, the peak would grow gradually with the coupling constant of the 2nd cladding mode as the ambient index approached 1.430. Above 1.430, the core mode would eventually begin to couple to the 3rd cladding mode as the coupling constant of the 2nd cladding mode fell off, and the peak depth would be close to what it had been in ambient air. In either case, the core mode will be coupling primarily to the 3rd cladding mode once

the ambient index exceeds approximately 1.435. The peak depth may decrease slightly as the ambient index approaches 1.440 since the coupling constant of the 3rd cladding mode increases past 196 m⁻¹.

In Figure 6.12, we have plotted the peak depths of our six batch processed LPFGs as a function of the ambient index. As in Figure 6.11, the top plot shows the 1.000 to 1.445 ambient index range while the bottom plot is an exploded view of the 1.400 to 1.445 ambient index range. Many of the predictions that we made based on the calculated coupling constants are confirmed by the measured data. All six LPFGs transitioned around the 1.430 ambient index, and as the ambient index was increased from there, the peak depths grew gradually. When the ambient index reached 1.440, the peaks depths were close to what they had been in ambient air, and they decreased slightly as the ambient index was increased beyond 1.440. We also note that the evolution of the peak following the transition is not smooth, and the peak depth does not increase linearly. The fluctuations that we see in the curves probably result from non-uniform index modulations along the length of the gratings and the non-uniform ITO overlays. These two non-uniformities will determine the ambient index at which the transition occurs and how strongly the core mode couples to the 2nd and 3rd cladding modes following the transition. Also, some of the fluctuations may have resulted from misinterpreting spectra that lacked clearly defined resonant peaks or had multiple resonant peaks.



(a)



(b)

Figure 6.12: The measure peak depths from the six batch processed LPFGs as a function of the ambient index. In the top plot (a), the ambient index range is 1.000-1.445. The bottom plot (b) is an exploded view of the 1.400-1.445 ambient index range.

6.3 - Optimizing the LPFG Performance

Given the known errors in our fabrication processes, the four-layer model fit our experimental data relatively well. The tuning capabilities of our LPFGs were well approximated by the calculated resonant wavelength curves, and we were able to prove that non-uniform UV exposure during the writing process affected the resonant wavelength. The peak depth trends that we predicted using the calculated coupling constants were supported by the measured data. Drawing from this analysis, we believe that the four-layer model can be used to determine the feasibility of an LPFG with specified tuning properties. In the case of our tunable filter, we require a tuning range of at least 40 nm (the bandwidth of the C-band) and a constant peak depth. Additionally, the tuning should occur over a range of ambient indices that can be achieved by an E-O polymer. Based on the model results in this chapter, we should be able to achieve these tuning specifications if we reduce the amount of error during fabrication. By varying the ambient index from 1.428 to 1.433, a range that can be achieved with an E-O polymer, the effective index of the 3rd cladding mode increases by 2.4×10^{-4} , which yields an approximate resonant wavelength shift of -96 nm for a grating period of 400 μm . More importantly, over the same ambient index range, the coupling constant of the 3rd cladding mode only varies by about 2 m^{-1} , which amounts to a -0.82 dB change in peak depth. By properly coordinating grating strength (i.e. UV exposure time) with the thickness and refractive index of the ITO overlay, the core mode will couple to the 3rd cladding mode once the 1st cladding mode has transitioned to the overlay, and a tunable LPFG with a better than 40 nm range and stable peak depth can be achieved.

Since we did not have the means to measure the actual photoinduced refractive index modulation in our fibers, we used the resonant peak wavelength as a measure of the grating strength. As a grating was written, the peak would grow in depth and would shift to longer wavelengths as the exposure time was increased. We could control the grating strength by stopping the writing process once the peak had reached the desired wavelength. All of the LPFGs were coated with the same ITO overlay (i.e. 50 nm, 1.88 refractive index at 632 nm) and tuned with index matching oils. Using this method, we were able to determine the initial peak wavelength (1356 nm) that would produce a tunable LPFG with a stable peak depth over an extended tuning range. The tuning

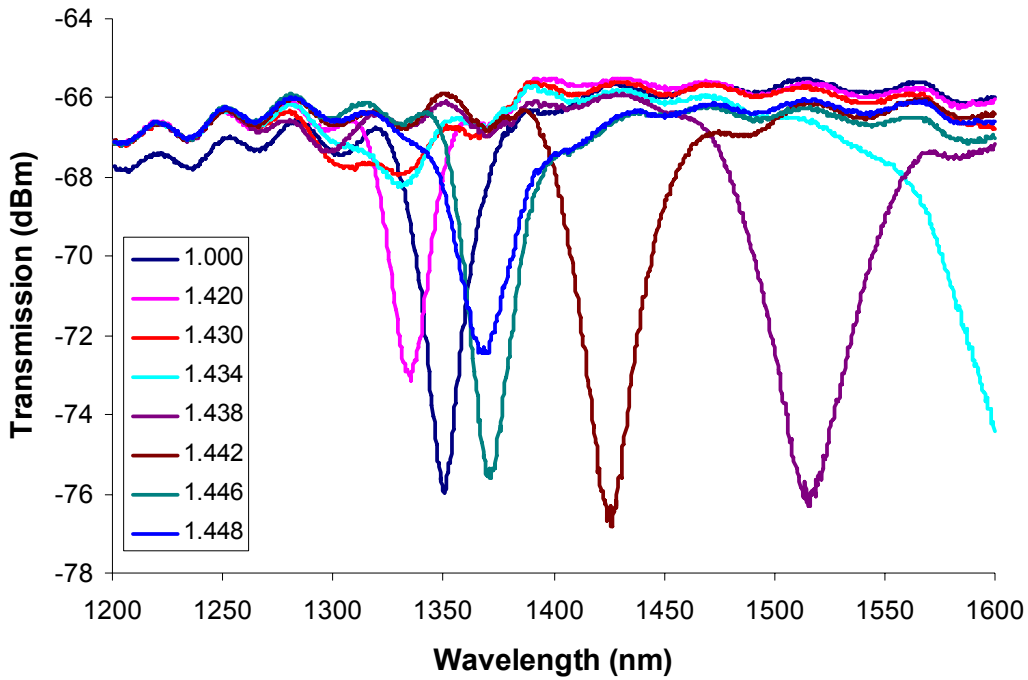


Figure 6.13: The tuning spectra of an LPFG that maintains a stable peak depth over nearly 150 nm of its tuning range. (Fiber diameter = 40 μm , Grating period (Λ) = 400 μm , Grating length = 8 mm, ITO thickness = 50 nm, ITO refractive index ~ 1.80)

spectra of one such LPFG is shown in Figure 6.13. The total tuning range of this LPFG is in excess of 200 nm, but more importantly, the peak depth stays within 1 dB of its maximum over nearly 150 nm of that range. Furthermore, the 150 nm tuning range over which the peak is stable can be achieved by varying the ambient refractive index from 1.438 to 1.446, a difference of only .008.

To confirm that the results in Figure 6.13 were not an anomaly, we fabricated more LPFGs with 1356 nm initial peak wavelengths and measured their tuning spectra. The results are shown in Figure 6.14. Every time we batch processed a set of six fibers 2-3 of the fibers were used to write LPFGs with 1356 nm peak wavelengths, and in Figure 6.14, the LPFGs that are next to one another came from the same batch (i.e. (a) and (b), (c) and (d), (e) and (f)). Each of the LPFGs depicted in Figure 6.14 tuned well in excess of 150 nm, and LPFGs that came from the same batch tuned similarly. None of the LPFGs in Figure 6.14, however, performed as well as the LPFG shown in Figure 6.13.

The spectra in Figures 6.13 and 6.14 perfectly illustrate the strengths of the four-layer model and weaknesses in our fabrication processes. The performance of the LPFG from which the spectra in Figure 6.13 were taken was very close to what we predicted from the model simulations. However, when we fabricated more LPFGs with the same parameters, we were unable to duplicate the original's performance. Nevertheless, there is a lot that can be learned from the spectra shown in Figure 6.14. Given the limitations of our equipment and the known errors that occur during fabrication, the LPFGs that were batch processed performed similarly as long as we wrote the initial resonant peak to the same wavelength. This is a major accomplishment because it means that the errors

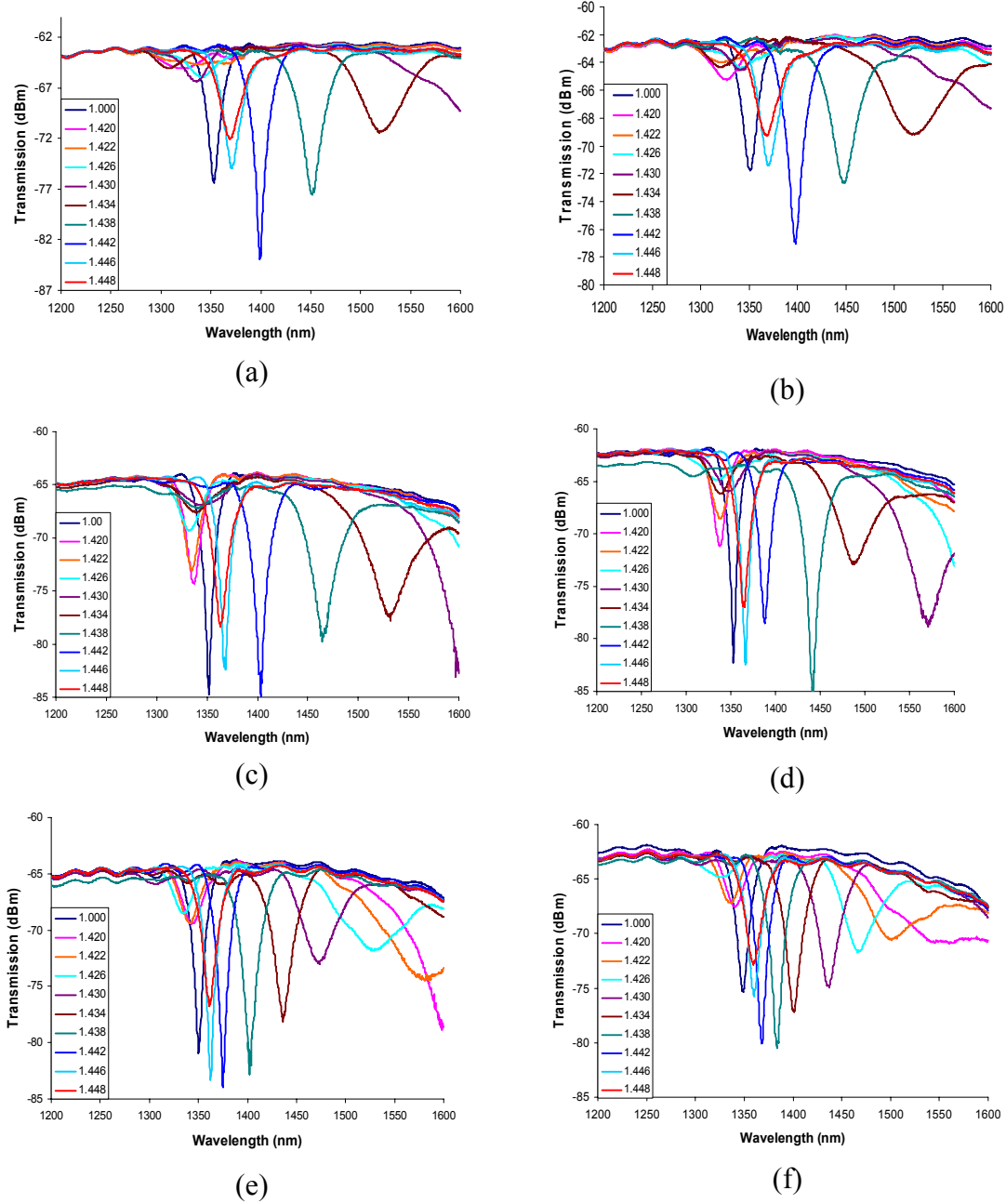


Figure 6.14: Tuning spectra of several LPFGs whose initial peak wavelengths were 1356 nm. (Fiber diameter = 40 μm , Grating period (Λ) = 400 μm , Grating length = 8 mm, ITO thickness = 50 nm, ITO refractive index ~ 1.80)

that are being incurred during fabrication are not statistically random. Most of the errors are repeatable, and our LPFGs are being limited by the equipment we are using, not our theoretical design. Based on this conclusion and the spectra in Figure 6.13, the four-layer model appears to be accurate, and we should be able to use it to generate a set of parameters for an LPFG with a given set of performance characteristics. On the other hand, producing LPFGs that match the predicted tuning performance metrics of the model, or even two LPFGs with identical performance characteristics, is extremely difficult without having access to equipment with enhanced capabilities and error tolerances. There are simply too many sources of error in our fabrication processes to consistently match the LPFG parameters needed for specific tuning characteristics. In our experiments, we used the same LPFG and ITO parameters throughout so that we could limit our analysis to a single ideal-case LPFG. We limited our scope because we realized that we needed to minimize the number of fabrication parameters that were varied from sample to sample in order to have any amount of consistency. Batch processing reduced the amount of error and increased the consistency among samples in the same batch, but the performance of samples with the same parameters taken from different batches still fluctuated significantly. The two areas where we would benefit greatly from more accurate equipment would be grating writing and sputtering. If we could improve in these two areas, we would be able to consistently produce samples that were much closer to ideal. Even though we did not have access to such resources during the course of this research, the four-layer model results provided us with a set of target LPFGs parameters, and by carefully controlling our fabrication processes, we were able to create some LPFGs that nearly matched the performance predicted by the model.

Chapter 7

Future Work

As discussed in the previous chapter, we have reached a point in our work on the tunable LPFG filter where the limitations of our equipment have begun to hinder progress. In order to effectively use the four-layer model to guide further development of our device, we would not only need more advanced equipment, but we would also need to redesign our fabrication processes around the new equipment's capabilities. In addition to the tunable LPFG filter, there are other applications to which we can extend LPG and tunable LPG technology. In this chapter, we will examine some of the projects that may be considered for future research.

7.1 - Tunable LPFG Filter

In this thesis, we have presented an analysis of the tunable LPFG design and showed that the four-layer model can be used to predict an LPFG's performance. With the new model and better equipment, work can continue on this project and here are some topics that need to be addressed.

- **Filter Prototype:** The primary goal of this research effort was to fabricate a working LPFG filter prototype with a 40 nm tuning range, a resonant peak bandwidth of less than 1 nm, and nanosecond switching speed. Although we did not meet this goal, the analysis and experimental work presented in this thesis has

shown that targeted tuning range for the device is more than feasible as long as the proper fabrication parameters are chosen and experimental error is minimized. Figure 4.5 shows the resonant peak of an LPFG with a nanocomposite cladding tuned electro-optically over 50 nm. These experimental results prove that an LPFG can be tuned via an E-O polymer cladding and that a tuning range large enough to cover the C-band can be achieved. In Figure 6.13, the resonant peak of an LPFG with an optimized ITO overlay is tuned over 200 nm by index matching oils, and the depth of the resonant peak is maintained over nearly 150 nm of that range. The performance metrics of the LPFG in Figure 6.13 nearly matched those predicted by the four-layer model. Future research on the tunable LPFG filter should focus on fabricating a prototype that matches the performance of the LPFG whose spectra are shown in Figure 6.13. In addition to more advanced equipment, the prototype fabrication effort needs to be coordinated with someone familiar with E-O polymers so that the LPFG and ITO parameters can be optimized to the refractive index range covered by the E-O polymer cladding. Alternatively, nanoparticles may be used to create a composite polymer with a variable index range that has been tuned to the most sensitive index range of the ITO coated LPFG. Some of the fabrication processes may also need to be redesigned according to the configurations and capabilities of the new equipment.

- **Bandwidth reduction:** While tunable LPFG technology has many potential applications, the electro-optically tunable LPFG presented in this thesis was designed primarily as a filter in fiber optic communications networks. However,

at the current 3 dB bandwidth ($\sim 20\text{-}25$ nm), our device cannot be used as a stand alone component in most wavelength division multiplexing (WDM) systems. The LPFG bandwidth needs to be reduced to be viable in such systems. We targeted a bandwidth of less than 1 nm so that the device could be used in dense wavelength division multiplexing (DWDM) communication systems where the channel spacing is approximately 0.8 nm. In the theory for weak gratings, the relative bandwidth is inversely proportional to the number of grating periods (Eq. 5.35). To increase the number of periods, the overall grating length must be increased or the grating period must be reduced. Figure 7.1 shows the spectra from two LPFGs fabricated in our lab. In Figure 7.1(a), the LPFG has a 400 μm period and is 8 mm in length. The LPFG in Figure 7.1(b) also has a 400 μm period but is 4 cm in length. By keeping the grating period constant and increasing the overall length of the grating (i.e. the number of periods) by a factor of five, the bandwidth

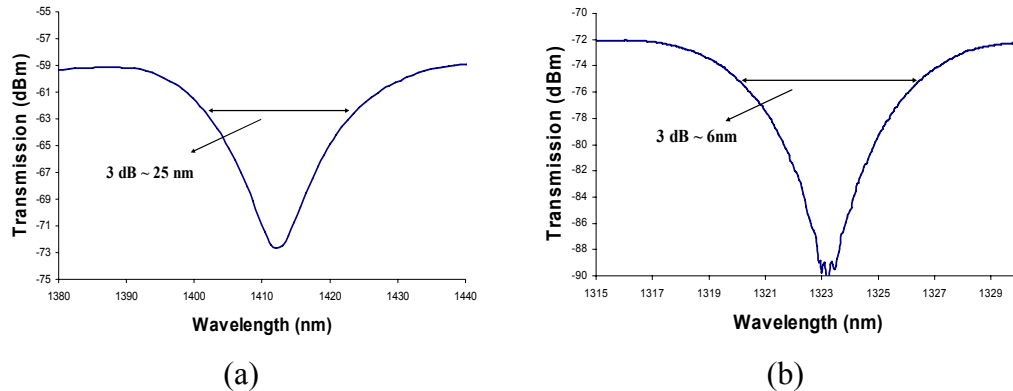


Figure 7.1: The resonant peak bandwidths of two LPFGs are compared: (a) an LPFG that has a 400 μm grating period and is 8 mm in length versus (b) an LPFG that has a 400 μm grating period and is 40 mm in length. When the number of periods is increased by a factor of five, the bandwidth is reduced by approximately the same factor.

reduced gof the resonant peak is reduced by approximately the same factor, which is consistent with the theory. When the light propagating through a fiber interacts with a larger number of periods, the magnitude of the photoinduced index change, or grating strength, must be reduced in order to achieve a single, strong, narrowband peak. This reduction is required to prevent overcoupling, a phenomenon in which the wavelengths that had been coupled into the cladding modes couple back into the core over the length of the grating. The grating period, the grating strength, and the total number of periods must be coordinated properly to maximize the attenuation of the resonant band and to prevent overcoupling.

As a result of the reduction in grating strength, there is less room for alignment error during fabrication, and more accurate equipment is needed to produce narrowband gratings that tune consistently. In Chapter 6, we showed that alignment and exposure errors in the grating writing process were major limiting factors in the consistency of our LPFGs. While we were able to suppress some of the effects of small misalignment errors by using short grating lengths (less than 1 cm) and high grating strengths in our experiments, the effects of these errors are exacerbated when the overall length of the grating is increased. The slightest misalignment will cause the photoinduced index change along the length of the LPFG to become increasingly non-uniform as the length is increased. The non-uniform exposure, in turn, compromises the coordinated balance between the grating period, the grating strength, and the total number of periods. This error is

not apparent in Figure 7.1, but as in Chapter 6, the major effects of the non-uniform exposure become apparent when an LPFG is tuned.

Apart from the more stringent alignment requirements, there are fundamental and practical limits to which the weak grating theory can be applied to bandwidth reduction. Fundamentally, Equation 5.35 certainly will not hold ad infinitum and will most likely have a lower limit (i.e. it may break down when the grating becomes extremely weak). Even if we assume that perfect alignment can be achieved with better equipment, there will be a point at which further reduction in the resonant peak bandwidth does not result from simply adding more periods. Practically, there are limits to the number of grating periods that can be added before overcoupling occurs and LPFG length. Assuming that weak grating theory does not break down, there will be a minimum grating strength that can be achieved with UV-laser illumination. Once this threshold is reached, adding more periods by either increasing the LPFG length or reducing the grating period will induce overcoupling and will not result in further bandwidth reduction. Furthermore, the accuracy of the fabrication processes and the application to which the tunable LPFG filter is being applied will dictate the maximum useful LPFG length. In Figure 7.1, we kept the grating period constant and increased the total grating length by a factor of five. As a result, the resonant peak bandwidth was reduced by approximately the same factor. The spectrum in Figure 7.1(b) shows the narrowest resonant peak bandwidth (~ 6 nm) that we achieved experimentally. Even if we were not limited by our fabrication processes and weak grating theory held for extremely weak gratings, an LPFG with a 400 μm

period would have to be 32 cm long in order to achieve a resonant peak bandwidth of roughly 0.75 nm. In addition to the problems that would arise from trying to fabricate a 32 cm, thin cladding LPFG (e.g. etching, writing, coating, handling, etc.), a device of that length would not be very practical as a component in a fiber optic communication network, especially when considering the fact that the length of the fiber containing the LPFG must not be bent or wound for the device to operate properly. In applications other than fiber communications, slightly longer LPFGs may be more practical, but most of these applications do not have the stringent bandwidth requirements that necessitate a large increase in length.

While there are many fundamental and practical challenges associated with bandwidth reduction via an increase in LPFG length, we have not addressed bandwidth reduction by means of shortening the grating period. A shorter period length provides for a larger number of periods in a fixed amount of length, and many of the practical problems associated with longer LPFGs are avoided. However, many of the fundamental problems still exist, namely that a large number of periods requires a very weak index modulation. Additionally, there are challenges associated with writing shorter period ($< 300 \mu\text{m}$) LPFGs in thin fibers. The resonant peaks of these LPFGs appear at wavelengths below 1200 nm (Figure 3.7). Even though cladding mode transitions will cause the resonant peak to “jump” to a longer wavelength, there is no guarantee that the post-transition peak will appear in the 1550 nm wavelength range.

Although we targeted a sub-1 nm bandwidth for the tunable LPFG filter, this goal may not be attainable using a single LPFG. However, Figure 7.1 is evidence that a substantial bandwidth reduction can be achieved by increasing the LPFG length to a few centimeters. The ~ 6 nm bandwidth shown in Figure 7.1(b) is not small enough to be used in DWDM systems, but it is sufficient for many other WDM systems. Even narrower bandwidths may be achieved by using the tunable LPFG filter in conjunction with FBGs or other wavelength filtering devices.

- **Creating a tunable narrowband filter:** We have shown that substantial bandwidth reduction can be achieved by increasing the total number of periods in an LPFG. However, turning the narrowband LPFG into a tunable filter will be considerably more challenging. Since the grating strength and grating length are both changed to reduce the bandwidth, the four-layer model is needed to determine the new LPFG and ITO parameters for the narrowband tunable filter. Additionally, the longer sections of thin fiber add to the complexity of the process. These fibers are more difficult to handle and more fragile than the fibers we used in our experiments. New fabrication processes will need to be designed to accommodate the added length.

- **Switching speed and stability:** Switching speed and stability are two important aspects of the tunable filter that must also be considered in future work. We had hoped to explore both of these issues during the course of this research effort, but

after finding that the three-layer model was incomplete, most of our time was spent developing a new four-layer model and focusing on the tuning characteristics of the device.

Our goal was to achieve nanosecond tuning speeds with our prototype filter. Unfortunately, we never had an opportunity to test the electro-optic tuning speed because of the problems that we had with the ITO and polymer layers. The switching speed will be limited by not only the polymer response time, but also by the conductivity of the ITO electrodes. The ITO electrodes must have a high conductivity to reduce the amount of time it takes to change the applied field and to prevent charge buildup at the ITO/polymer interfaces. In future work, the response time of the polymer should be measured when it is a stand-alone film as well as when it is coated onto the thin cladding fiber. ITO deposition methods must also be studied in order to control the thickness, refractive index, and conductivity of the electrode layers.

Stability is another key issue that must be addressed in order to make the tunable LPFG a viable fiber network device. There are two types of stability to consider for the LPFG filter – thermal and long term. When exposed to temperatures in excess of 125 °C for extended periods of time, LPFGs that are fabricated in photosensitive fibers by UV-illumination tend to degrade because the dopants responsible for the photoinduced index change tend to anneal out [10]. As a result, LPFGs fabricated in photosensitive fibers are not recommended for filters or sensors that are to be used in harsh environments. However, as a component in a fiber optic network, the LPFG filter will probably not be

subjected to temperatures in excess of 125 °C for significant amounts of time, and even if the temperature reaches or exceeds this threshold for a brief period of time, the device will survive. In terms of performance, the resonant wavelength of the tunable LPFG is temperature sensitive, and unwanted tuning will occur if there are significant temperature swings. However, temperature compensation techniques have been proposed and may be employed to reduce the thermal sensitivity of the device [8,21]. The degree to which temperature compensation must be used will depend on the application and the temperature stability of the environment. In addition to thermal stability, long-term stability must also be tested. This may consist of placing a working tunable LPFG filter in an environmental chamber for several days and monitoring its performance under varied conditions. Some studies have suggested that exposing photosensitive fibers to a small amount of UV light before an LPFG is written helps improve the long term stability of the device [10].

7.2 - Tunable LPGs in planar waveguides

LPGs are not limited to fiber optics, and in many ways, they are easier to implement in planar structures and waveguides [61]. In this thesis, we have detailed some of the problems that have resulted from non-uniform coatings on the cylindrical surfaces of our fiber samples. The primary reason for the non-uniform coatings was that most of our equipment was designed for planar substrates, and the coating processes did not conform well to the cylindrical geometry of a fiber. With this in mind, it is a logical

step to take the tunable LPFG design and attempt to apply it to planar and rectangular waveguide structures.

The structure and refractive index of fused silica and other types of bulk glasses can be changed by exposing them to infrared femtosecond laser pulses [62-67]. By translating a piece of fused silica (bulk or wafer) through a beam of focused pulses, optical waveguides can be directly written into the material [62,66]. LPGs can be made in the same fashion by focusing the pulses through an amplitude or phase mask before they interact with the silica. To create a resonant band in the output spectrum of a waveguide written into a piece of silica, an LPG can be written inside or adjacent to the waveguide core. Since the effective indices of both the core and cladding modes are a function of the material indices of the core and cladding (Eqs. 3.3 and 3.5), modulating either material index will give rise to a resonant band in the output spectrum. In addition to silica, sapphire may be another material in which waveguides and LPGs can be written by focused femtosecond pulses.

Planar LPGs can also be made tunable with an E-O polymer. Unlike the tunable LPFG case, however, where the E-O polymer had to be wrapped around the fiber, there are several different ways an E-O polymer can be used to tune the planar LPG spectrum. For example, if the LPG is written to the core of a planar waveguide and the waveguide is close enough to the silica surface, the tails of the guided mode field distribution will interact with the ambient, and changes in the ambient index will cause the resonant band to shift. By coating the surface of the silica with ITO and a layer of E-O polymer, the guided mode field distribution will interact with the polymer layer, and the resonant band will tune as the refractive index of the polymer is varied. This method of tuning a planar

LPG is similar to the tunable LPFG case. Some other ways to tune a planar LPG with an E-O polymer may include using the polymer as the waveguide core and writing the LPG adjacent to it, or writing the LPG directly into the polymer. The major advantage of implementing tunable LPGs in planar waveguides is that there is more flexibility in the design. Additionally, the speed and performance of a tunable planar LPG device should be about the same as that of the tunable LPFG since the same tuning mechanisms are being employed. Some added insertion loss may be incurred when coupling a fiber to the planar waveguide, but this loss can be minimized by properly designing the waveguide and precisely aligning the input and output fibers. However, the added flexibility in the planar LPG design may come at the cost of an increased number of fabrication steps, which may include photolithography, etching, and other semiconductor processing methods [68-69].

7.3 - Add/drop tunable filter

A more long term goal related to the tunable filter project is the creation of an add/drop filter for fiber optic networks. As a stand alone component, the tunable filter in this thesis only has the ability to drop a communications channel. The wavelengths that are coupled to the cladding modes attenuate quickly as they propagate and are difficult to collect for evaluation. A more dynamic device would have the ability to not only drop a channel, but also to add one in its place. This type of device would allow a channel to be dropped, monitored, and then reinserted into the original signal. It would also allow the content of a certain channel to be changed on the fly. An add/drop filter could be

implemented in a number of different ways, and some potential designs involving gratings have been explored [70-71]. One possible approach would be to use our knowledge of tunable grating technology to develop an intermediate period grating (IPG) ($\Lambda \sim 10^{-5}$ m). This type of grating would couple energy from an incident signal to forward propagating cladding modes like an LPG, but would feature a narrower bandwidth because we could increase the number of grating periods without increasing the overall grating length³. An optical add/drop filter design that utilizes an IPG is shown in Figure 7.2. The design shown is for a planar device, but a similar structure could

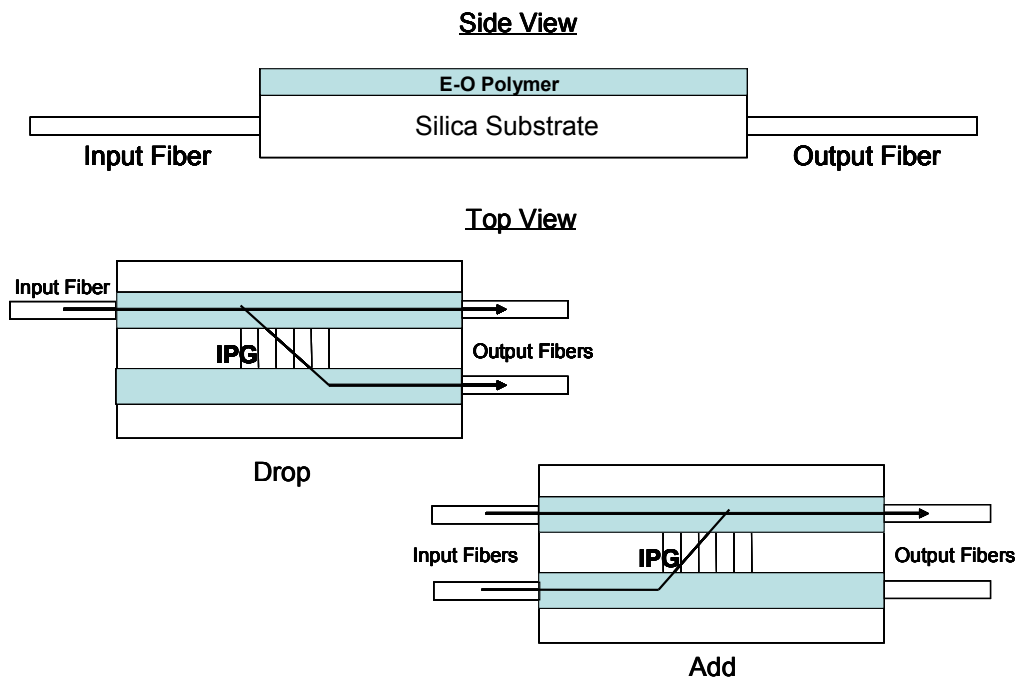


Figure 7.2: Optical add/drop filter design featuring a tunable IPG.

³ Although we have discussed the bandwidth reduction limitations previously, many of those limitations were a result of writing LPFGs in photosensitive fibers with UV-laser irradiation. If we were to change our fabrication methods, we may be able to overcome some of those limitations. For example, by using highly accurate semiconductor processing methods, we may be able to achieve a smaller minimum grating strength than what can be achieved in photosensitive fibers with a UV laser.

potentially be made in a dual core fiber. The functionality of the device is fairly straightforward. A multi-wavelength signal is injected into the top waveguide by a fiber optic cable. The IPG couples the resonant wavelength(s), which can be tuned by varying the index of the E-O polymer overlay, into the bottom waveguide. (Alternatively, one or both of the actual waveguides could be made of E-O polymer, and the resonant band of the IPG would be tuned by varying the index of one, or both of the waveguide cores.) The resonant wavelength(s) are then output to a detector where the signal can be monitored. To add or replace the wavelengths that were dropped, a narrowband signal would be sent through the bottom waveguide, and the IPG would couple it back into the original signal. While the design in Figure 7.2 is just one possible way an optical add/drop filter could be implemented, it clearly illustrates how the functioning device should operate.

7.3 - Sensing applications

In addition to devices for optical communications networks, tunable LPFG technology can also be used in sensing applications [9-14, 72-76]. LPFGs have an intrinsic sensitivity to changes in temperature due to the thermal coefficients of the silica fiber. As the surrounding temperature varies, the resonant band of the LPFG tunes. Since silica fibers can withstand temperatures in excess of 1000 °C, LPFGs are well suited for high temperature sensing as long as suitable grating writing techniques are used. LPFGs written by UV illumination in photosensitive fibers tend to degrade when exposed to sustained temperatures in excess of 125 °C. However, LPFGs written by

electric arc or femtosecond IR laser pulses can withstand temperatures in excess of 1000 °C [10,75-77]. If even higher temperature sensing is required, LPFGs can be fabricated in sapphire fibers, which can withstand temperature in excess of 1500 °C. Also, in sensing applications, there is no need to improve the bandwidth or collect filtered wavelengths, which reduces the design complexity of an LPFG temperature sensor. In addition to temperature, LPFGs may be used to sense stress, strain, and perhaps biological agents. An LPFG that senses biological agents may be realized by replacing the E-O polymer in our tunable filter design with a polymer that is sensitive to the concentration of a specific agent in the air. A rise in the concentration level of the specified agent will induce a change in the refractive index of the polymer, which will cause the resonant wavelength to shift.

Chapter 8

Summary and Conclusions

In this thesis, a design for an electro-optically tunable filter based on an LPFG was presented. Coupled mode theory and a three-layer model analysis were used to verify the working principles of the device and its operation. It was shown that a single resonant band in the near infrared spectrum could be achieved by using an LPFG with a thin cladding layer and that the resonant wavelength could be tuned by varying the refractive index of the surrounding medium. The single resonant band LPFG and its tunability were further verified experimentally.

While the immediate goal of this research was to fabricate a working prototype of the filter, several unexpected results were recorded when the filter design was tested - the most notable being the effects of the thin ITO electrode that was coated onto the thin cladding LPFG. Since the effects of this layer were originally thought to be negligible, the ITO layer was not included in the three layer model. Thus, the tuning effects that were observed when the ITO coated LPFG was tested had not been predicted. Further research was required to understand that the high index ITO was causing mode transitions in the cladding, and a new four-layer model was developed to quantitatively analyze the tuning characteristics of the ITO coated LPFG. The preliminary results of the model verified the existence of mode transitions in our device and helped us understand how changes in the cladding mode field distributions were affecting the depth of the resonant peak.

After using the four-layer model to look at the modal field distributions in the cladding and quantify the ITO coated LPFG's enhanced sensitivity to changes in the ambient index, we compared the model calculated data to measured data from a single LPFG before and after it had been coated with ITO. Since the uncoated LPFG was the simplest case to model and there were fewer sources of error in the measured data from our uncoated sample LPFG, we calibrated the model to the measured spectral data from the uncoated sample LPFG. By calibrating the model to this data set, we believed that the model would better fit the measured data from ITO coated LPFG, and we would be able to see how the performance of our ITO coated LPFG sample deviated from the ideal-case LPFG more easily.

When we first compared the two data sets, there was a large gap between the wavelengths predicted by the model and those we measured, but the shapes of the curves were similar. We were able to eliminate the gap between the model and measured data by using the full resonant wavelength equation, which takes the strength of the grating into account. Once the model fit the uncoated LPFG data, we moved to the ITO coated LPFG and found that our measured results only deviated slightly from the model data.

Even though the measured data from the ITO coated LPFG fit the model, we needed to see how well the model results compared to measured data from additional samples. We fabricated six new ITO coated LPFGs and compared their measured spectral data to the model. Since the samples were batch processed, we assumed that all of their parameters were the same except for the grating strengths, which varied due to our grating writing setup. Even though the samples were batch processed, we saw differences in their tuning performance, and none of the new measured data sets fit the

model as well as the data from the first sample LPFG. However, by adjusting the grating strength in the model, we achieved a better fit between the model and the measured data, which confirmed our theory that the fiber alignment during writing was one of the primary sources of error among a group batch processed samples.

The comparisons between the model data and the seven measured data sets convinced us that the model was accurately predicting the tuning capabilities of our LPFG, and we turned our attention to the how well the model predicted an LPFG's resonant peak depth. Using the calculated coupling constants, we predicted how the depth of the resonant peak should change as the LPFG was tuned and compared our predicted results to the measured resonant peak depths from our samples. The general trends predicted by the model were reflected in the measured data, but the peak depth curves that were compiled from the sample LPFGs spectra varied from sample to sample. We concluded that the peak depth differences were most likely a result of non-uniformities in the LPFG's index modulation and the ITO overlay.

After comparing the model results to the measured data from our sample LPFGs, we were convinced that the model could be used to guide the development of the tunable filter. However, the limitations of our equipment prevented us from consistently making LPFGs that performed as well as the model predicted. Using the model data, we showed that a tunable LPFG with a tuning range in excess of 40 nm and a stable resonant peak depth could be achieved if our fabrication errors were reduced. We also showed the tuning spectrum of an LPFG that nearly met the performance metrics predicted by the model. When we tried to duplicate the performance of our "nearly-ideal" sample, we found that we could consistently achieve a large tuning range, but could not always

maintain a consistent peak depth across the tuning range. We also showed that the tuning performances of samples that were batch processed were similar as long as the grating strengths were nearly equal. This was an important observation because it meant that the differences in performance between batch processed samples were resulting from repeatable errors, which supported our claim that our tunable LPFGs were being limited by fabrication processes, not our theoretical design.

Once the analysis of the four-layer model and the experimental data had been completed, we briefly discussed some research topics that could be explored in the future using the LPFG analysis from this thesis. With better equipment, work could continue on the tunable filter project. The goals of further research should include fabricating a working prototype, reducing the bandwidth, evaluating filter stability and eventually, creating a narrowband tunable filter. The theory and design of the tunable filter could also be extended to planar waveguides. Using focused infrared femtosecond pulses, LPGs can be directly written into silica and sapphire waveguides and tuned with an EO-polymer. The design flexibility gained by working in planar waveguides may spawn a variety of devices that incorporate LPGs. One device of particular interest would be an optical add/drop filter, and the potential design for such a device was presented. Finally, tunable LPG technology can be used in sensing applications. The intrinsic properties of LPFGs written in silica and sapphire fibers make them well suited for temperature sensing. LPGs could also be used in the detection of stress, strain, and biological agents.

When we began our LPFG research, our primary goal was to create a working tunable filter prototype. With the majority of the theory behind our design completed, we felt that most of our time would be spent on engineering the processes needed to

fabricate our filter and experimentation. However, as this thesis has shown, the original three-layer model from which the tunable filter was conceived was not complete. In addition to engineering the processes needed to fabricate tunable LPFGs, we researched the effects of high index overlays and created a new four-layer model that included the ITO layer of our filter. The development and evaluation of the four-layer model was one of the major accomplishments of this work. Even though other research groups have identified cladding mode transitions and presented ways to calculate the fields and coupling constants in an LPFG, the four-layer model is a comprehensive tool that can be used to optimize the performance of a tunable LPFG that has been coated with a high index overlay. In this thesis, we used the model to find the optimal thickness and refractive index for the ITO layer of our tunable LPFG filter. With the optimized ITO layer, the model predicted that we could achieve a large tuning range and a stable resonant peak depth. When we fabricated an LPFG with the optimized ITO layer, it tuned in excess of 200 nm when the ambient index was increased by 0.01 and maintained a constant peak depth over nearly 150 nm of that range. These performance statistics were consistent with those predicted by the model. To the best knowledge of the author, the optimized LPFG had the highest sensitivity to the ambient refractive index ever reported for an LPFG and was another major accomplishment of our work. The experimental data from the optimized sample validated both the model results and our fabrication processes. However, we were unable to duplicate the optimized LPFG sample because we could not consistently overcome the prevailing errors that were incurred during fabrication. We were able to consistently produce LPFGs with tuning ranges in excess of 200 nm but were unable to keep the resonant peak depth constant over a large

portion of the tuning range. Although we were unable to produce a working prototype of the electro-optically tunable LPFG filter, the four-layer model, the experimental data from the optimized LPFG, and the analysis presented in this thesis make tunable LPGs a more viable technology and can be used to guide future research once more advanced equipment becomes available.

References

1. T.E. Tsai, G.M. Williams, and E.J. Friebel, "Index structure of fiber Bragg gratings in Ge-SiO₂ fibers," Opt.
2. G.A. Rakuljic and V. Leyva, "Volume holographic narrow-band optical filter," Opt. Lett., 18 (6), 459-461, 1993.
3. S. Yin, B.D. Guenther, and F.T.S. Yu, "A Tunable Narrow-Band Filter Using Photorefractive Fiber," Opt. Mem. and Neur. Net., 5 (1), 35-41, 1996.
4. A. M. Vengsarkar, P. J. Lemaire, J. B. Judkins, et. al., "Long period fiber gratings as band-rejection filters," J. Lightwave Technology., 14 (1), 58-64, 1996.
5. A. Abramov, B. Eggleton, J. Rodgers, et. al., "Electrically Tunable Efficient Broad-Band Fiber Filter," Phot. Tech. Lett., 11 (4), 445-447, 1999.
6. X. Shu, L. Zhang, and I. Bennion, "Sensitivity characteristics of long-period fiber gratings," J. Lightwave Tech., 20 (2), 255-266, 2002.
7. Y. Zhu, P. Shum, J.H. Chong, et. al., "Deep-notch, ultracompact long-period grating in a large-mode-area photonic crystal fiber," Opt. Lett., 28 (24), 2467-2469, 2003.
8. J.N. Jang, S.Y. Kim, S.W. Kim, et. al., "Novel Temperature Insensitive Long-period Grating by using the Refractive Index of the Outer Cladding," presented at the *Optical Fiber Communications Conference 2000*, OFC 2000 (IEEE, 2000), 1, 29-31.
9. W. H. Steier, A.Chen, S.S. Lee, et. al. "Polymer electro-optic devices for integrated optics," Chem. Phys., 245(1-3), 487-506, 1999.
- 10 S.W. James and R.P. Tatum, "Optical fibre long-period grating sensors: characteristics and application," Meas. and Sci. Technology, 12, R49-R61, 2003.
- 11 A. Cusano, P. Pilla, L. Contessa, et al., "High-sensitivity optical chemosensor based on coated long-period gratings for sub-ppm chemical detection in water," Appl. Phys. Lett. 87, 234105, 2005.
- 12 K. Zhou, X. Chen, L. Zhang, et. al., "Optical chemsensors based on etched fibre Bragg gratins in D-shape and multimode fibres," SPIE Conf. Proceedings, Vol. 5855, 158-161, 2005.

- 13 M. Konstantaki, S. Pissadakis, S. Pispas, et al., "Optical fiber long-period grating humidity sensor with poly(ethylene oxide)/cobalt chloride coating," *Appl. Opt.* 45 (19), 4567-4571, 2006.
- 14 Z. Wang, S. Ramachandran, "Ultrasensitive long-period fiber gratings for broadband modulators and sensors," *Opt. Lett.*, 28 (24), 2458-2460, 2003.
- 15 V. Bhatia, "Properties and sensing applications of long-period gratings", Ph.D. dissertation, Virginia Polytechnical Institute and State University, 1996.
- 16 S. Yin, K. Reichard et al, "Single resonant band, tunable optical fiber wavelength filter based on long period fiber grating," U.S. Patent No. 6,563,985.
17. S. Yin, O. Leonov, K.W. Chung, et. al., "Wavelength tuning range enhanced single resonant band fiber filter using a long period grating (LPG) with ultra thin cladding layer," presented at the *Optical Fiber Communications Conference 2000*, OFC 2000 (IEEE, 2000), 1, 23-25.
- 18 S. Yin, K. Chung, and X. Zhu, "A highly sensitive long period grating based tunable filter using a unique double-cladding layer structure," *Opt. Comm.*, 188, 301-305, 2001.
- 19 S. Yin, K. Chung, and X. Zhu, "A novel all-optic tunable long-period grating using a unique double-cladding layer," *Optics Comm.*, 196, 181-186, 2001.
20. Q. Chen, J. Lee, M. Lin, et. al., "Investigation of Tuning Characteristics of Electrically Tunable Long-Period Gratings, With a Precise Four-Layer Model," *J. Lightwave. Tech.*, 24 (7), 2954-2962, 2006.
21. J. Lee, C. Hahn, B. Wang, et. al., " A quantitative analysis of an athermal design for a long period grating based tunable filter," *Opt. Comm.*, 258, 184-192, 2006.
- 22 H. J. Patrick, A.D. Kersey, and F. Bucholtz, "Analysis of the Response of Long Period Fiber Gratings to External Index of Refraction," *J. Light. Tech.*, 16 (9), 1606-1612, 1998.
- 23 B. Lee, Y. Liu, S. Lee, et. al., "Displacements of the resonant peaks of a long-period fiber grating induced by a change of ambient refractive index," *Opt. Lett.*, 22, 1769-1771 1997.
- 24 K. Chung and S. Yin, "Analysis of a widely tunable long-period grating by use of an ultra thin cladding layer and higher-order cladding mode coupling," *Optics Letters*, 29, 812-814, 2004.
- 25 A. Cusano, A. Iadicicco, P. Pilla, et. al., "Mode transition in high refractive index coated long period gratings," *Opt. Exp.*, 14, 19-34, 2006.

26. R. Huo, Z. Ghassemlooy, A. Hassan, et. al., "Modelling of long-period fibre grating response to refractive index high than that of cladding," *Meas. and Sci. Technology*, 12, 1-5, 2001.
27. I. Ishaq, A. Quintela, S. James, et al., "Modification of the refractive index response of long period gratings using thin film overlays," *Sensors and Actuators B-Chemical*, 107(2), 738-741, 2005.
28. S. W. James, N. D. Rees, R. P. Tatam, et. al. "Optical fiber long-period gratings with Langmuir-Blodgett thin-film overlays," *Opt. Lett*, 27, 686-687, 2002.
29. Z. Wang, J.R. Heflin, R.H. Stolen, et. al., "Analysis of optical response of long period fiber gratings to nm-thick thin-film coatings", *Opt. Exp.*, 13, 2808-2813, 2005.
30. I D. Villar, I. R. Matias, F. J. Arregui, et. al., "Optimization of sensitivity in Long Period Fiber Gratings with overlay deposition", *Opt. Exp.*, 13, 56-69, 2005.
31. A. Yariv, "Coupled-Mode Theory for Guided-Wave Optics," *IEEE Journal of Quantum Electronics*, Vol. QE-9(9), 919-933, 1973.
32. A. Ghatak and K. Thyagarajan, *Introduction to Fiber Optics*, Cambridge University Press, New York, New York, 1998, Chap. 21, 454-461, Appendix E, pp. 543-546, Appendix F, pp. 547-552.
33. E. Hecht, *Optics 3rd Ed.*, Addison-Wesley, 1998, Chap. 3, 66-73.
34. D.K. Mynbaev and L.L. Scheiner, *Fiber-Optic Communications Technology*, S. Helba, Ed., Prentice-Hall, Inc., Upper Saddle River, New Jersey, Chap. 5, 139-144, Chap. 13, pp. 616-627.
35. G. P. Agrawal, *Fiber-Optic Communication Systems 2nd Ed.*, K. Chang, Ed., John Wiley & Sons, Inc., New York, NY, 1997, Chap. 2, pp. 30-39, Chap. 7, 296-303, Chap. 9, pp. 441-444.
36. T. Erdogan, "Cladding-mode resonances in short- and long- period fiber grating filters," *J. Opt. Soc. Am. A*, 14, 1760-1773, 1997
37. A. Yariv, *Optical Electronics in Modern Communications 5th Ed.*, Oxford University Press, 1997.
38. D. Gloge, "Weakly guiding fibers," *App. Opt.* 10, 2252-2258, 1971.
39. E. Anemogiannis, E.N. Glytsis, and T.K. Gaylord, "Transmission characteristics of long-period fiber gratings having arbitrary azimuthal/radial refractive index variation", *J. Lightwave Technol.*, 21, 218-227, 2003.

40. K. Chung and S. Yin, "Analysis of random grating period and amplitude errors in ultra-thin long-period grating," *Microwave and Optical Technology Letters*, Vol. 12, 178-181, 2001.
41. W. Ren, S. Bauer, S. Yilmaz, et. al., "Optimized poling of nonlinear optical polymers based on dipole-orientation and dipole-relaxation studies," *J. Appl. Phys.*, 75 (11), 7211-7219, 1994.
42. F. Qiu, K. Misawa, X. Cheng, et. al., "Determination of complex tensor components of electro-optic constants of dye-doped polymer films with a Mach-Zehnder interferometer," *Appl. Phys. Lett.*, 65 (13), 1605-1607, 1994.
43. C.C. Teng and H.T. Man, "Simple reflection technique for measuring the electro-optic coefficient of poled polymers," *Appl. Phys. Lett.*, 56 (18), 1734-1736, 1990.
44. M.J. Bananch, M.D. Alexander, Jr., S. Caracci, et. al., "Enhancement of Electrooptic Coefficient of Doped Films through Optimization of Chromophore Environment," *Chem. Mater.*, 11 (9), 2554-2561, 1999.
45. M.A. Mortazavi, A. Knobles, S.T. Kowal, et. al., "Second-harmonic generation and absorption studies of polymer-dye films oriented by corona-onset poling at elevated temperatures," *J. Opt. Soc. Am. B.*, 6 (4), 733-741, 1989.
46. H.L. Hampsch, J.M. Torkelson, S.J. Bethke, et. al., "Second harmonic generation in corona poled, doped polymer films as a function of corona processing," *J. Appl. Phys.*, 67 (2), 1037-1041, 1990.
47. L. Sun, J. Kim, C. Jang, et. al., "Polymeric waveguide prism-based electro-optic beam deflector," *Opt. Eng.*, 40 (7), 1217-1222, 2001.
48. D.Y. Jeong, Y.K. Wang, M. Huang, et. al., "Electro-optical response of the ferroelectric relaxor poly(vinylidene fluoride – trifluoroethylene – chlorofluoroethylene) terpolymer", *J. Appl. Phys.*, 96 (1), 316-319, 2004.
49. R.A. Synowicki, "Spectroscopic ellipsometry characterization of indium tin oxide film microstructure and optical constants," *Thin Solid Films*, 313-314, 394-397, 1998.
50. Y.S. Jung, "Spectroscopic ellipsometry studies on the optical constants of indium tin oxide films deposited under various sputtering conditions", *Thin Solid Films*, 467, 36-42, 2004.
51. A. Uzupis, S. Tamulevicius, R. Butkute, et. al., "Effect of deposition conditions and annealing on residual stress of ITO films magnetron sputtered on silica," *Physica Status Solidi*, 1 (2), 307-311, 2003.

52. D.I. Kim, Y.Z. Yoo, and H. G. Chun, "Effect of Post Deposition Annealing Temperature on the Optoelectrical Property of ITO thin Films Prepared by Magnetron Sputter Type Negative Metal Ion Source," *Solid State Phenom.*, 118, 287-293, 2006.
53. M. Libra, L. Bérdos, and H. Baráňková, "Influence of post-deposition annealing on the electrical conductivity of indium-tin-oxide films," *Physica Status Solidi*, 116 (1), K65-K67, 2006.
54. N.G. Patel and B.H. Lashkari, "Conducting transparent indium-tin oxide films by post-deposition annealing in different humidity environments," *J. Mat. Sci.*, 27 (11), 3026-3031, 1992.
55. C. Yeh and G. Lindgren, "Computing the propagation characteristics of radially stratified fibers: an efficient method", *Appl. Opt.*, 16, 483-493, 1977.
56. T. Erdogan, "Fiber Grating Spectra," *J. Lightwave Tech* , 15 (8), 1277-1294, 1997.
57. J. Adams, *An Introduction to Optical Waveguides*, Wiley & Sons, 217, 1983.
58. C. Dengpeng, and Q. Jingren, "Calculation of coupling coefficient between core mode and cladding modes of fiber grating," *Communications*, 1999. APCC/OECC '99. Fifth Asia-Pacific Conference on ... and Fourth Optoelectronics and Communications Conference, 2, 1471-1473, 1999.
59. B. Stegall and T. Erdogan, "Leaky Cladding Mode Propagation in Long-Period Fiber Grating Devices," *Photonics Tech. Lett.*, 11 (3) 343-345, 1999.
60. E.K. Illy and H.J. Booth, "Comparison of Fibre Bragg Grating Writing at Multiple UV Wavelengths," ECOC, Copenhagen, Denmark, 2002.
61. Rastogi and K.S. Chiang, "Long-period gratings in planar optical waveguides," *Appl. Opt.*, 41 (30), 6351-6355, 2002.
62. M. Will, S. Nolte, B.N. Chichkov, et. al., "Optical properties of waveguides fabricated in fused silica by femtosecond laser pulses," *Appl. Opt.*, 41 (21), 4360-4364, 2002.
63. Y. Kondo, K. Nouchi, T. Mitsuyu, et. al., "Fabrication of long-period fiber gratings by focused irradiation of infrared femtosecond laser pulses," *Opt. Lett.*, 24 (10), 646-648, 1999.
64. J.W. Chan, T. Huser, S. Risbud, et. al., "Structural changes in fused silica after exposure to focused femtosecond laser pulses," *Opt. Lett.*, 26 (21), 1726-1728, 2001.

65. D. Homoelle, S. Wielandy, A.L. Gaeta, et. al., "Infrared photosensitivity in silica glasses exposed to femtosecond laser pulses," *Opt. Lett.*, 24 (18), 1311-1313, 1999.
66. A. Saliminia, N.T., Nguyen, M.C. Nadeau, et. al., "Writing optical waveguides in fused silica using 1 kHz femtosecond infrared pulses," *J. Apps. Phys.*, 93 (7), 3724-3728, 2003.
67. Y. Cheng, K. Sugioka, M. Masuda, et. al., "Optical gratings embedded in photosensitive glass by photochemical reaction using a femtosecond laser," *Opt. Exp.*, 11 (15), 1809-1816, 2003.
68. K.K. Tung, W.H. Wong, and E.Y.B. Pun, "Polymeric optical waveguides using direct ultraviolet photolithography process," *Appl. Phys. A* , A 80, 621-626, 2005.
69. R.G. DeCorby, N. Ponnampalam, M.M. Pai, et. al., "High Index Contrast Waveguides in Chalcogenide Glass and Polymer," *J. Selected Topics. in Quantum Electronics*, 11 (2), 539-545, 2005.
70. A. Ankiewicz, A.H. Wang, and G.D. Peng, "Analysis of narrow bandpass filter using coupler with Bragg grating in transmission," *Opt. Comm.*, 156, 27-31, 1998.
71. S. Tomljenovic-Hanic and J.D. Love, "Planar Waveguide Add/Drop Wavelength Filters Based on Segmented Gratings," *Microwave and Opt. Tech Lett*, 37 (3), 163-165, 2003.
72. V. Bhatia, " Applications of long-period grating to single and multi-parameter sensing," *Opt. Exp.* 4 (11), 457-466, 1999.
73. Y.G. Han, B.H. Lee, W.T. Han, et. al., "Resonance Peak Shift and Dual Peak Separation of Long-Period Fiber Gratings for Sensing Applications," *Phot. Tech. Lett.*, 13 (7), 699-701. 2001.
74. S. Chen, Z. Tong, O. Zhao, et. al., "A smart bending sensor with a novel temperature- and strain-insensitive long period grating," *Sensors and Actuators A*, 116, 103-106, 2004.
75. Y. Zhu, C. Zhan, J. Lee, S. Yin, and P Ruffin, "Multiple parameter vector bending and high-temperature sensors based on asymmetric multimode fiber Bragg gratings inscribed by an infrared laser," *Opt. Lett.*, 31 (13), 2006.
76. S.H. Nam, C. Zhan, J. Lee, C. Hahn, K. Reichard, P. Ruffin, K.L. Deng, and S. Yin, "Bend-insensitive ultra short long-period gratings by the electric arc method

- and their applications to harsh environment sensing and communication," Opt. Exp., 13, 731-737, 2005.
77. G. Rego, O. Okhotnikov, E. Dianov, et. al., "High-Temperature Stability of Long-Period Fiber Gratings Using an Electric Arc," J. Lightwave. Tech., 19 (10), 1574-1579, 2001.

Appendix

Publications

Journal papers related to this research effort

1. J. Lee, Q. Chen, Q. Zhang, K. Reichard, D. Ditto, J. Mazurowski, M. Hackert, and S. Yin “Enhancing the Tuning Range of a Single Resonant Band LPG While Maintaining the Resonant Peak Depth By Using an Optimized High Index ITO Overlay,” *App. Opt.*, 46 (28), 6984-6989, 2007.
2. J. Lee, C. Hahn, B. Wang, K. Reichard, D. Ditto, D. Glista, Q. Wang, S. Yin, “A quantitative analysis of an athermal design for a long period grating based tunable filter,” *Optics Comm.*, 258, 184-192, 2006.
3. Q. Chen, J. Lee, M. Lin, Y. Wang, S. Yin, Q. Zhang, and K. Reichard, “Investigation of Tuning Characteristics of Electrically Tunable Long-Period Gratings With a Precise Four-Layer Model,” *J. Lightwave Tech.*, 24 (7), 2954-2962, 2006.
4. Q. Chen, M. Lin, J. Lee, Q. Zhang, S. Yin, “Nanocomposites with very large electro-optic effect and widely tunable refractive index,” *Appl. Phys. Lett.*, 89, 2006.
5. Sung Hyun Nam, Chun Zhan, Jon Lee, Corey Hahn, Karl Reichard, Paul Ruffin, Kung-Li Deng, and Shizhuo Yin, “Bend-insensitive ultra short long-period gratings by the electric arc method and their applications to harsh environment sensing and communication,” *Opt. Exp.*, 13, 731-737, 2005.

Conference proceedings and presentations related to this research effort

1. Q. Chen, M. R. Lin, J. E. Lee, Q. M. Zhang, and S. Yin, “Nanocomposite with very large electro-optic effect and widely tunable refractive index”, to be presented at MRS 2006 Fall Meeting, Boston, MA, November 2006.
2. S. Yin, Q. Zhang, J. Lee, Q. Chen, K. Reichard, J. Mazurowski, D. Ditto, M. Hackert, “Ultra-Fast, All-Fiber Tunable Filter Based on Long Period Grating,” AVFOP Presentation, Annapolis, MD, September 2006.

3. J. Lee, S. Yin, Q. Zhang, Q. Chen, K. Reichard, J. Mazurowski, D. Ditto, M. Hackert, "A review on the recent advances of an all-fiber electronically tunable wavelength filter," SPIE Conference Proceedings, vol. 6314, August 2006.
4. S. Yin, Q. Zhang, J. Lee, Q. Chen, K. Reichard, "Quantitative analysis of the performance of an all-fiber electronically tunable wavelength filter with a four-layer model," Poster Presentation at SPIE Optic and Photonics, San Diego, CA, August 2006.
5. Q. Chen, M. R. Lin, Y. Wang, Q. M. Zhang, J. Lee, S. Yin, and K. Reichard, "Widely Electrically Tunable Long-Period Fiber Gratings with Ferroelectric Relaxor P(VDF-TrFE-CFE) Terpolymer", Poster Presentation at 15th International Symposium on the Applications of Ferroelectrics (ISAF2006), Sunset Beach, NC, August 2006
6. Q. Chen, M. R. Lin, Y. Wang, Q. M. Zhang, J. E. Lee, S. Yin, and K. Reichard, "Widely electrically tunable long-period fiber gratings with ferroelectric relaxor poly(vinylidene fluoride - trifluoroethylene - chlorofluoroethylene) terpolymer as second cladding", SPIE Conference Proceedings, vol. 6117, 2006.
7. J. Lee, Q. Chen, S. Yin, K. Reichard, Q. Zhang, D. Ditto, J. Mazurowski, and M. Hackert, "Unique all-fiber tunable filter using a single resonant-band LPG and nanoparticle dispersed electro-optic polymer," Poster Presentation at OFC/NFOEC, Anaheim, CA, March 2006.
8. K. Reichard, S. Yin, J. Lee, C. Hahn, D. Ditto, Q. Wang, S. Nam, Q. Zhang, Q. Chen, and J. Claude, "Recent advances on all-fiber tunable filter," SPIE Conference Proceedings, vol. 5911, 2005.
9. J. Lee, C. Hahn, S. Nam, B. Wang, K. Reichard, D. Ditto, D. Glista, Q. Wang, and S. Yin, "An Athermal Design on LPG Based Tunable Filter," SPIE Conference Proceedings, vol. 5560, 2004.

Additional journal papers

1. C. Zhan, J. Lee, Z. Yong, S. Yin, P. Ruffin, and J. Grant, "Multi-parameter harsh environment using photo-enhanced polarization mode separated fiber Bragg gratings," submitted to Optics Comm., in June 2006.
2. C. Zhan, J. Lee, S. Yin, P. Ruffin, and J. Grant, "Photoenhanced polarization mode separated fiber Bragg gratings inscribed by femtosecond laser," J. Appl. Phys., 101, 053110, 2007.

3. Y. Zhu, C. Zhun, J. Lee, S. Yin, and P Ruffin, "Multiple parameter vector bending and high-temperature sensors based on asymmetric multimode fiber Bragg gratings inscribed by an infrared laser," Opt. Lett., vol. 31, no. 13, 2006.
4. Yi Yang, Jon Lee, Karl Reichard, Paul Ruffin, Frank Liang, Dave Ditto, and Shizhuo Yin, "Fabrication and implementation of a multi-to-single mode converter based on a tapered multimode fiber," Optics Comm., pp. 129-137, 2005.

VITA

Jonathan E. Lee

Jonathan Lee received a BSE in electrical engineering, as well as a certificate in Engineering and Management Systems (EMS), from Princeton University in 2002. While in the engineering program at Princeton, Jonathan concentrated in optics, but also developed solid background in electrical engineering fundamentals, including circuit theory, integrated circuits, and signal processing. The EMS certificate program required him to take additional courses in economics, statistics, and optimization. In addition to his school work, Jonathan had summer internships with Morgan Stanley (Summer 2000) and Sensors Unlimited (Summer 2001), a small technology firm based in Princeton, New Jersey that specializes in infrared imaging equipment. Following his summer internship with Sensors Unlimited, Jonathan worked with the company on his senior project entitled, "Optimization of 40 Gigabit PIN Photodiodes."

Upon graduating from Princeton, Jonathan took a position with the ARRO Group, a small engineering consulting firm based in Lancaster, Pennsylvania. As one of the only electrical engineers on staff, Jonathan worked on a variety of engineering projects that included the design and implementation of supervisory control and data acquisition systems (SCADAs) for municipal water and wastewater treatment facilities, programming custom database software that was integrated with geographical information systems (GIS), and power distribution and lighting for various municipal buildings. While working for ARRO, Jonathan also took and passed the Fundamentals of Engineering (FE) exam in the spring of 2003.

In the fall of 2003, Jonathan matriculated to Penn State University to start his graduate work in electrical engineering. He took a research assistantship position with Dr. Stuart (Shizhuo) Yin, whose research interests included electro-optics, optical sensing, and photonic devices. The focus of Jonathan's research, and primary motivation behind his Ph.D. thesis, was an all-fiber optic, tunable filter, a device patented by Dr. Yin. While the primary goal of the project was to quantitatively model the filter and develop the processes required to manufacture prototype devices, a number of research opportunities presented themselves as the project progressed. Some of the research topics that spawned from the tunable filter project included fiber grating fabrication processes, thermal compensation for long period fiber gratings (LPFGs), nanoparticle dispersed electro-optic polymers, and cladding mode transitions in optical fibers as a result of high index overlays. Jonathan's work in these areas allowed him to obtain his Masters' degree in May of 2005 and his Ph.D in December 2007. In addition to his theses, Jonathan has authored and co-authored a number of journal papers and conference proceedings, and is a member of SPIE, OSA, and IEEE.